VU VRIJE UNIVERSITEIT AMSTERDAM | UNIVERSITEIT VAN AMSTERDAM

MSc of Physics & Astronomy

Advanced Matter and Energy Physics

An ultrastable optical cavity for a strontium optical atomic clock

by

Scott Wolzak

STUDENT ID	11906944
EXAMINER	prof. dr. Florian Schreck
SECOND EXAMINER	dr. Klaasjan van Druten
DAILY SUPERVISOR	dr. Sumit Sarkar
MASTER	Physics & Astronomy (joint degree UvA/VU)
TRACK	Advanced Matter and Energy Physics
UNIVERSITY	University of Amsterdam & VU University Amsterdam
INSTITUTE	Van der Waals-Zeeman Institute (WZI)
FACULTY	Faculteit der Natuurwetenschappen, Wiskunde en Informatica (FNWI)
PROJECT DURATION	October 2022 - August 2023
CREDITS	60 ECTS

UNIVERSITY OF AMSTERDAM
Institute of Physics

Abstract

The primary objective of this project is to conceptualize and construct an ultrastable optical cavity. The cavity is intended to serve as a frequency reference to a laser operating at 698 nm. The laser will be used to interrogate strontium atoms in a 1D optical lattice clock that is currently under development in the group. The objective for building this cavity is to provide the clock laser a short-term frequency instability of $\sigma_y < 3 \cdot 10^{-16}$ at 1 s, limited by the thermal noise floor of the cavity.

In this work, we focus on designing a 30 cm long ultrastable cavity. We highlight the current limitations of modern cavities that impede the reduction of the thermal noise floor. To ensure that the cavity reaches its projected thermal-noise-floor it needs to be made insensitive to external influences. The mechanical instability was investigated using finite element method (FEM) analysis in COMSOL. An optimal spacer diameter of 8 cm was identified and the optimal positions of the supporting points were determined at $dx = 61.35$ mm and $dz = 3.75$ mm. This resulted in the following gradients of the acceleration and tilt sensitivities $\frac{\delta k_z}{\delta dz} = 7.3 \cdot 10^{-11}$ g^{-1} mm^{-1}, $\frac{\delta \kappa_z}{\delta dx} = 7.0 \cdot 10^{-11}$, $\frac{\delta \kappa_y}{\delta dx} = 7.3 \cdot 10^{-11}$ and $\frac{\delta \kappa_x}{\delta dz} = -8.1 \cdot 10^{-11}$ g^{-1} mm^{-2}. Additionally, a design of a self-balancing structure is developed for mounting the cavity.

The thermal sensitivity of the cavity was investigated by creating a model that defines an effective coefficient of thermal expansion. The relative cavity length change $\frac{\Delta L}{L}$ was simulated at differing temperatures in COMSOL. The zero-crossing temperature shift caused by the fused silica mirror substrates was investigated by attaching ULE annuli to the back side of the mirrors.

Furthermore, the effectiveness of a three-layer aluminium heat shield design for housing the cavity was simulated. Initially, a theoretical framework is established that describes the radiative and conductive heat transfer. An expression for the time dependent temperature variation for both the three heat shields and the cavity was found. A geometrical model of the heat shields encasing the cavity was made in COMSOL and the time dependent radiative heat transfer response was computed. Finally, to conclude we present a preliminary design of the complete optical setup surrounding the cavity that includes the Pound-Drever-Hall (PDH) laser stabilization, fiber noise cancellation, active residual amplitude modulation (RAM) suppression and power stabilization.

Contents

1 Introduction **5**

2 Theoretical background **8**

2.1 Optical atomic clocks: basic framework of operation 8

2.2 Evaluation of frequency instability 9

2.3 Stability of optical clocks 11

2.4 Optical reference cavities 12

2.4.1 Fabry-Pérot resonator theory 12

2.4.2 Resonator stability 14

2.4.3 Longitudinal & transverse modes 14

2.5 Laser stabilization to an optical cavity 16

2.5.1 Pound-Drever-Hall locking 17

2.5.2 Residual amplitude modulation 20

2.5.3 Fiber noise cancellation 21

2.6 Stability transfer using a frequency comb 24

2.7 Three-cornered hat comparison 27

3 Design of an ultra-stable optical cavity **29**

3.1 Thermal noise limit 29

3.2 Reduction of thermal noise in optical cavities 32

3.2.1 Cavity materials 32

3.2.2 Mirror configurations & Spacer length 33

3.3 Mechanical instability 37

3.3.1 Finite-element analysis 37

3.3.2 Poisson effect & mirror tilt 40

3.3.3 Misalignment Analysis 42

3.3.4 Modelling cavity length change 43

3.4 Optimization of support positions 45

3.4.1 Transverse acceleration 49

3.4.2 Longitudinal acceleration 51

3.4.3 Spacer geometry optimization 51

3.4.4 Support area dependency 54

3.4.5 Transverse support offset 55

3.4.6 Finalized configuration 57

3.4.7 Limitation of the FEM simulations 57

3.5 Cavity Mounting 58
3.6 Thermal sensitivity 60
3.6.1 ULE annulus 62
3.6.2 Heat transfer modelling 62
3.6.3 Heat shields design 64

4 Optical layout for the stabilization of the clock laser **67**

5 Summary & Outlook **69**

A Power spectral density & Allan deviation **72**

B Technical drawings cavity & mounting structure **73**

References **78**

1 Introduction

For as long as humans have been interested in the keeping of time, it has been quantized by measuring in units of repeating periodic events. Historic civilizations kept time by diurnal changes, based on Earth's rotation and its periodic orbit around the sun. Due to technological advances in recent times, the keeping of time on a much shorter timescale has become more and more important. Mechanical timekeepers like the pendulum clock, based on the physical swinging of a pendulum, were replaced by quartz clocks that were able to oscillate in the Gigahertz range, during the beginning of electronic timekeeping. This advancement in timekeeping was sufficient to show that Earth's rotation is not constant, limiting the ability to keep time based on Earth's rotation to milliseconds [1].

Already in 1879 James Clark Maxwell realized the potential of atoms to serve as a natural standard of time, due to their "likeliness in every physical property" and availability in practically "infinite numbers" [2]. This embodies the desire of physicists at that time to standardize the unit of time. Unbeknownst to Maxwell, his suggestion would become prophetical. With the development of quantum mechanics and advances in the understanding of atomic physics at the start of the twentieth century, the General Conference on Weight and Measures (CGPM) defined the SI unit of time on the frequency corresponding with the hyperfine splitting of the cesium-133 atom in its groundstate in 1967.

Over the following decades, atomic clocks using the microwave transition of cesium continued to improve in their fractional frequency uncertainty with approximately one order of magnitude per decade. Especially the implementation of laser cooling proved essential for reducing systematic uncertainties due to lower atomic temperatures [3; 4; 5; 6]. In the last decade, atomic species with clock transitions that operate at optical frequencies have been chosen as better candidates for time and frequency references.

Optical atomic clocks differ from microwave clocks by operating on optical transitions with frequencies of hundreds of Terahertz. This offers several orders of magnitude gain in terms of fractional frequency instability. Hence, the SI second is likely to be redefined with more contributions of optical atomic clocks in Temps Atomique International (TAI) [7]. Enhancements in frequency standards have facilitated the advancement of technologies like global navigation satellite systems (GNSS) and geodesy [8]. Furthermore, these improvements have played a pivotal role in fundamental physics research, investigating phenomena such as relativity [9], variations in the fine-structure constant α [10], and the proton-to-electron mass ratio μ [11].

One of the crucial components to create an atomic clock is a stable local oscillator. In an optical atomic clock, a frequency-stabilized laser fulfils the role of a local oscillator. The frequency of the laser is stabilized to the resonance frequency of an ultra-stable optical cavity,

which consists of two highly reflective mirrors attached to the ends of a spacer. When the laser is locked to the cavity resonance, the optical path length stability of the cavity is translated into the fractional frequency instability of the laser. Unfortunately, the cavity is susceptible to several environmental perturbations that can alter the effective optical path length of the cavity e.g. temperature and pressure fluctuations, vibrations and variations of the refractive index. To create a stable cavity that is insensitive to temperature fluctuations, the spacer can be made out of ultra-low-expansion (ULE) glass and the cavity can be encased in actively temperature-stabilized heat shields. By placing the cavity on an active vibration isolation platform with careful design of the cavity mounting, the vibration sensitivity can be minimized.

When environmental perturbations are sufficiently suppressed, the cavity length fluctuation can attain a fundamental instability limit, referred to as the *thermal-noise floor*. Thermal fluctuations cause unavoidable variations of the dimensions of the constituents of the cavity. For modern state-of-the-art cavities operating at room temperature, the dominant contribution of thermal noise arise from the Brownian noise of the highly-reflective mirror coatings, which often have a thickness of only several micrometres [12]. Currently, the best-performing cavities that operate at room temperature, are long extended cavities. These cavities incorporate spacers made from ULE glass and extend close to 50 cm in length. Laser that have been locked to such cavities have shown to achieve fractional frequency instabilities down to $\sigma_y \approx 1$ to $2 \cdot 10^{-16}$ at 1 s [13; 14].

Exploring ways to further reduce the thermal-noise floor of cavities have gained significant attention. Alternative coating materials with lower mechanical loss factors are being developed such as crystalline mirrors made from $Al_{0.92}Ga_{0.08}As/GaAs$ multilayers [15]. Additionally, operating at lower temperatures presents another strategy for reducing thermal noise. Recent advancements in cavity technology have demonstrated that cavities constructed from mono-crystalline silicon and operated under cryogenic conditions can help achieving ultra-stable lasers with low fractional frequency instabilities, reaching approximately $\sigma_y \approx 4 \cdot 10^{-17}$ at 1 s [16; 17].

The objective of the research outlined in this thesis is to design and construct a cavity suitable for room temperature operation, aiming to achieve thermal-noise-limited performance for a clock laser for strontium with fractional frequency instability $\sigma_y < 3 \cdot 10^{-16}$ at 1 s.

Outline of the thesis

- **Chapter 2:** Presents the necessary theoretical background about the workings of a Fabry-Pérot cavity and shows how laser stabilization with the Pound-Drever-Hall (PDH) method works. Further, we show how to characterize frequency instability and how to evaluate it using a three-cornered hat (TCH) comparison. In addition, we present rele-

vant noise sources like residual amplitude modulation (RAM) and fiber noise and discuss schemes on how to combat them.

- **Chapter 3:** Chapter 3: Lists various crucial aspects influencing cavity design. Firstly, it offers a comprehensive assessment of thermal noise and its constituent factors. Subsequently, it delves into diverse strategies for mitigating the impact of thermal noise, encompassing the selection of appropriate cavity materials and optimal mirror configurations. Secondly, ensuring the cavity attains its thermal-noise-limited performance necessitates insensitivity to vibrations and temperature fluctuations. Utilizing FEM software, mechanical instability is simulated, leading to the identification of optimal cavity geometry and support placements. The chapter introduces a self-balancing three-point mount for the cavity. To enhance comprehension of the cavity's thermal susceptibility, pertinent heat transfer mechanisms are discussed, alongside the introduction of a three-layer heat shield design. Lastly, the influence of a ULE annulus on cavity length is showcased.

- **Chapter 4:** Presents the proposed experimental setup of the new 30 cm ULE cavity, including: the PDH laser stabilization, fiber noise cancellation, active RAM suppression and power stabilization.

- **Chapter 5:** Gives an overview of the obtained cavity design and presents an outlook of what is left to be done to have the cavity operational and optimized.

2 Theoretical background

2.1 Optical atomic clocks: basic framework of operation

The measurement of time has traditionally involved counting cycles of a recurring event. To establish a reliable standard for frequency, a periodic signal is required, characterized by a consistently stable frequency that remains universal across both space and time. An atomic frequency standard is based on the frequency difference between two energy states of an atomic sample. To effectively transmit time and frequency data, an auxiliary local oscillator comes into play, responsible for continuously engaging with the atomic sample to track its resonance. In optical atomic clocks, this role is fulfilled by a laser. Initially, the laser is locked to one of the resonance frequencies of an ultra-stable optical cavity, delivering frequency stability over shorter timespan. The cavity-stabilized laser then interrogates the atoms, providing a measurement of the transition probability. Feedback is provided to the laser frequency to keep it locked to the atomic transition frequency where the transition probability is maximal. Ultimately, to create a functional clock, the local oscillator's oscillations must be quantified. This process involves converting the optical frequency, often in the hundreds of Terahertz range ($\sim 10^{14}$ Hz), into an electronically countable microwave frequency using an optical frequency comb. Figure 1 presents an overview illustrating the operational principles of a passive optical atomic clock.

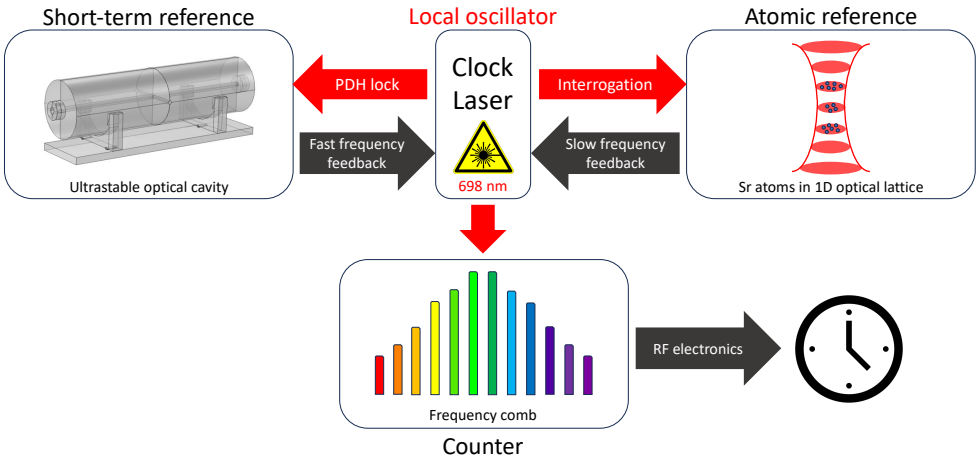


Figure 1: Overview of the general operation of a passive optical atomic (lattice) clock. The local oscillator is locked using the Pound-Drever-Hall scheme to an ultrastable optical cavity that provides fast-frequency feedback to the clock laser. The laser interrogates the atomic reference, here depicted as strontium atoms in a 1D optical lattice. The interrogation sequence provides a slow feedback to keep the local oscillator locked to the atomic transition. The number of oscillations is tracked using a optical frequency comb (OFC) that converts the optical frequency down to the microwave regime.

The performance of an atomic frequency standard is dependent on the quality of the local oscillator that probes the clock's atomic reference transition. To understand the stability of optical atomic clocks we need to be able to describe the frequency instability of an oscillator. Therefore, we start off by providing the necessary tools to characterize frequency instability.

2.2 Evaluation of frequency instability

For an ideal oscillator with amplitude E_0 and frequency ν_0, if the phase and amplitude are known at some point in time, its behaviour can be predicted for any time in the future. Unfortunately, for a real oscillator, the amplitude and phase fluctuations due to noise processes give rise to some uncertainty in these predictions. To be able to characterize the influence of these noise processes on the frequency stability of our laser, we need to quantize the frequency fluctuations. The instantaneous laser frequency is given by

$$\nu(t) = \nu_0 + \frac{1}{2\pi}\frac{d\phi(t)}{dt}, \tag{1}$$

where ν_0 is the mean frequency of the oscillator. So deviations of the instantaneous frequency from the mean frequency can be denoted as

$$\Delta\nu(t) = \nu(t) - \nu_0 = \frac{1}{2\pi}\frac{d\phi(t)}{dt}, \tag{2}$$

where the frequency deviation $\Delta\nu(t)$ is purely dependent on the time-derivative of the oscillator phase $\phi(t)$. To fairly compare the frequency noise among oscillators with different absolute frequencies, we normalize the frequency fluctuations, which gives

$$y(t) \equiv \frac{\Delta\nu(t)}{\nu_0}, \tag{3}$$

where $y(t)$ denotes the fractional frequency fluctuations. The fast frequency fluctuations are typically described in the frequency domain using the power spectral density (PSD) $S_\nu(f)$. The PSD of frequency fluctuations gives a noise spectrum and measures the distribution of energy in (Fourier) frequency space with units of [Hz^2/Hz]. The PSD of phase fluctuations $S_\phi(f)$ can be related to that of frequency fluctuations $S_\nu(f)$. Both $S_\phi(f)$ and $S_\nu(f)$ can be converted to the PSD of normalized frequency fluctuations $S_y(f)$ as

$$S_y(f) = \frac{S_\nu(f)}{\nu_0^2} = \frac{f^2}{\nu_0^2}S_\phi(f), \tag{4}$$

where f is the Fourier frequency. The normalized frequency noise spectrum can be classified into different types of noise using the following power law approximation

$$S_y(f) = \sum_{\alpha=-2}^{2} h_\alpha f^\alpha, \tag{5}$$

where different regions of the noise spectrum can correspond to different scaling with the exponent α, indicating a characteristic f^{α} noise dependency. The different types of noise are classified by the values of the exponent α and are shown in table 1 [18].

Noise Type	**PSD** $S_y(f)$	**AVAR** $\sigma_y^2(\tau)$
Random Walk FN	$h_{-2}f^{-2}$	$\frac{2}{3}\pi^2 h_{-2}\tau$
Flicker FN	$h_{-1}f^{-1}$	$2\ln(2)h_{-1}$
White FN	h_0	$\frac{1}{2}h_0\tau^{-1}$
Flicker PN	h_1f^{1}	$\frac{1.038+3\ln(2\pi f_H\tau)}{4\pi^2}h_1\tau^{-2}$
White PN	h_2f^{2}	$\frac{3f_H}{4\pi^2}h_2\tau^{-2}$

Table 1: Behavior of the Allan variance (AVAR) of the fractional frequency fluctuations for different power spectral densities (PSD) of typical sources of frequency and phase noise, denoted as FN and PN respectively [18].

A more common approach to characterize the stability of an oscillator over time is the Allan deviation $\sigma_y(\tau)$. Consider the frequency evolution of our laser in time $\nu(t)$, which can be measured with a frequency counter that gives a frequency average $\overline{\nu}_i$ over an averaging time window of τ. Therefore,

$$\overline{\nu}_i = \frac{1}{\tau}\int_{t_i}^{t_i+\tau} \nu(t)\, dt. \tag{6}$$

Usually, the standard deviation for N samples is a measure of how dispersed the data is compared to the mean. Hence, the information of the frequency fluctuations of the laser between different averaging times remains hidden. Such frequency fluctuations and their origin is crucial information we aim to obtain. Now, instead of comparing the frequency data to the mean laser frequency, the differences between adjacent frequency data points can be considered. The difference between successive averaged frequency data points will contain an averaging time-dependent measure of the frequency fluctuations. The AVAR is in this case, given by

$$\sigma_\nu(\tau)^2 = \frac{1}{2(N-1)}\sum_{i=1}^{N-1}(\overline{\nu}_{i+1}-\overline{\nu}_i)^2, \tag{7}$$

where the Allan deviation (ADEV) becomes

$$\sigma_\nu(\tau) \equiv \sqrt{\sigma_\nu^2(\tau)}. \tag{8}$$

Finally, we express the ADEV of fractional frequency fluctuations $y(t)$ as

$$\sigma_y(\tau) = \frac{\sigma_\nu(\tau)}{\nu_0}. \tag{9}$$

By measuring with small averaging time τ, one is able to identify high-frequency noise that acts on a short timescale, while for long τ, low frequency drifts like temperature fluctuations play a bigger role. It is also possible to calculate the Allan deviation from the measured noise PSD. The PSD can be determined by taking the Fourier transform of the autocorrelation function of frequency fluctuations $\Delta\nu(t)$, this is highlighted in more detail in appendix A.

The one-sided PSD $S_y(f)$ in the frequency domain, can be converted to AVAR $\sigma_y^2(\tau)$ in the time domain, using

$$\sigma_y^2(\tau) = 2\int_0^\infty S_y(f)\frac{\sin^4(\pi f\tau)}{(\pi f\tau)^2}df, \tag{10}$$

however, it is in general not possible to calculate the PSD from the ADEV [18]. Additionally, the ADEV doesn't allow the flicker phase noise and white phase noise to be distinguished from one another, since both give the same scaling $\sigma_y(\tau) \propto \tau^{-2}$, as is shown in table 1. To get around this, multiple alternatives to the Allan variance exist. The definitions of a few that are commonly used (e.g. modified ADEV) are denoted in appendix A.

Now we have gained insight into how to express frequency instability of oscillators, we will present the limitations of the fractional frequency instability of optical clocks and provide motivation for the use of ultrastable optical cavities for building an optical atomic clock.

2.3 Stability of optical clocks

The fundamental stability limit of an optical atomic clock is given by the quantum-projection noise (QPN) floor. QPN is a consequence of the repetitive projective measurement of the atom's quantum state [19].

For an optical atomic clock operating on an atomic transition with absolute frequency ν_0 and linewidth $\Delta\nu$, interrogating N atoms, the QPN-limited fractional frequency instability is given by

$$\sigma_y(\tau) = \kappa\frac{\Delta\nu}{\nu_0}\frac{1}{\sqrt{N}}\sqrt{\frac{T_c}{\tau}}, \tag{11}$$

where T_c is the total cycle time of the clock including dead time, τ is the averaging time and κ is a factor that depends on the exact interrogation scheme used. Clearly, the QPN-limit averages down with the square-root of the number of atoms that are being interrogated ($\propto 1/\sqrt{N}$). For this reason optical *lattice* clocks offer an advantage over single-ion clocks[1]. Furthermore, the QPN limit scales down with an increasing averaging time ($\propto 1/\sqrt{\tau}$). Unfortunately, a major limiting factor in achieving such desired stability of the clock is the coherence of the local oscillator. Frequency noise of the interrogation laser can prevent the atomic clock from reaching a

[1]Single-ion clocks do have the benefit that the ion often remains trapped after an interrogation cycle while a neutral ensemble is usually lost, requiring the preparation of a new ensemble.

QPN-limited instability. The low frequency fluctuations and drifts of the laser are corrected by interrogating the atoms and feeding the proper frequency correction to the laser. However, the laser has to be immune to the high frequency noise as much as possible in order to be able to interrogate the atoms. Therefore, to stabilize the frequency of the clock laser and reduce short-term frequency drifts it is locked to the resonance frequency of an ultrastable optical reference cavity. In the following section the concept of an optical reference cavity will be discussed.

2.4 Optical reference cavities

In practice, optical reference cavities are ultra stable Fabry-Pérot resonators. To grasp the fundamental theory of the Fabry-Pérot resonator, we will begin by examining the expressions for the electric fields of light within and outside a planar cavity. Furthermore, we will evaluate the stability of a resonator and subsequently, we will introduce a more realistic picture where a Gaussian beam is coupled into a cavity, leading to *transverse spatial modes*.

2.4.1 Fabry-Pérot resonator theory

To get familiar with the properties and behaviour of an ultrastable cavity, let's first consider the basic Fabry-Pérot resonator depicted in figure 2, which is given by two mirrors separated over a distance L. An incident monochromatic electromagnetic beam with frequency ω is denoted in the complex phasor notation as

$$E_I(t) = E_0 e^{-i(\omega t - \vec{k}\cdot\vec{r})} \tag{12}$$

where $\vec{r}$ is the position vector and $\vec{k}$ is the wavevector for which $|\vec{k}| = k = 2\pi/\lambda = \omega/c$ with λ the laser wavelength [20]. In each round trip, the light inside the cavity accumulates a phase factor $e^{-i\Delta\phi}$, with phase shift $\Delta\phi$ given by

$$\Delta\phi = k \cdot 2nL = \frac{2\pi}{\lambda} 2nL, \tag{13}$$

where n is the refractive index of the medium inside the cavity. The field inside the cavity E_C is given by

$$E_C = t \cdot E_0 \sum_{n=0}^{\infty} \left(r^2 e^{-i\omega \frac{2nL}{c}} \right)^n = \frac{t \cdot E_0}{1 - r^2 \cdot e^{-i\omega \frac{2nL}{c}}}, \tag{14}$$

where r and t are the amplitude reflection and transmission coefficients. This equation can be understood intuitively as a single transmission coefficient to get inside the cavity and the constructive interference of light waves that keep reflecting within the cavity. The transmitted field E_T can be described using the field that circulates inside the cavity and is given by

$$E_T = E_C \cdot e^{-i\omega \frac{nL}{c}} \cdot t = E_0 \frac{t^2 \cdot e^{-i\omega \frac{nL}{c}}}{1 - r^2 \cdot e^{-i\omega \frac{2nL}{c}}}. \tag{15}$$

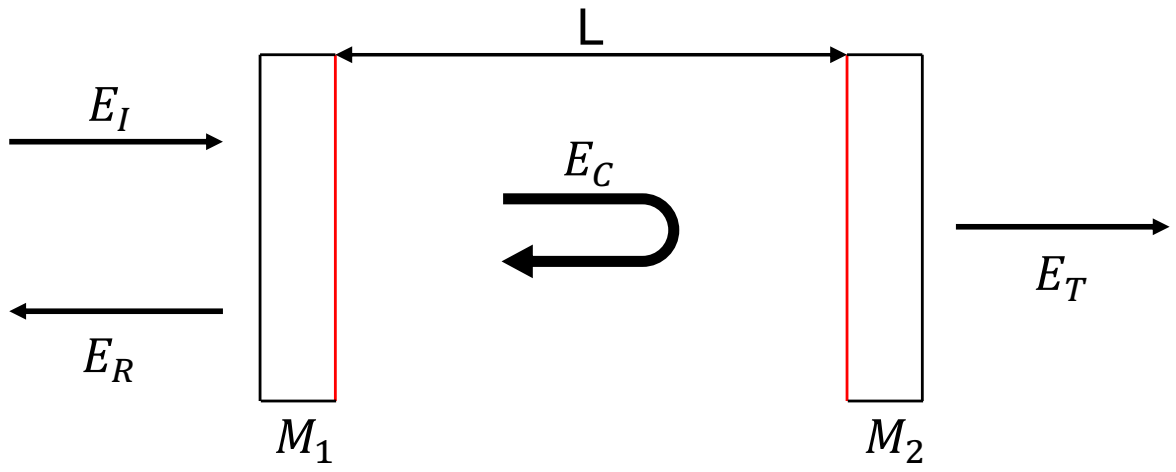


Figure 2: Schematic overview of the simplified planar Fabry-Pérot resonator of length L, considering plane waves. The incident and reflected fields are denoted by E_I and E_R respectively. The circulating field inside the cavity is given by E_C and the transmitted field by E_T.

The following transmitted field intensity I_T is given by

$$I_T = |E_T|^2 = \frac{t^2 E_0^2}{1 + r^4 - 2r^2 \cos(\Delta\phi)}, \tag{16}$$

which has the profile of an Airy function with maxima for $\Delta\phi = q \cdot 2\pi$ with integer q. Rewriting this in terms of frequency ν gives

$$\nu = q \cdot \frac{c}{2nL} = q \cdot \Delta\nu_{FSR}, \tag{17}$$

where $\Delta\nu_{FSR}$ is the free spectral range (FSR), which corresponds to the frequency seperation between consecutive transmission peaks of the cavity. It is also equal to the inverse of the round-trip travel time of the light inside the cavity. The linewidth Γ of the cavity is defined by the full-width at half maximum (FWHM) of the Airy peaks and is given by

$$\Gamma = \Delta\nu_{FWHM} = \frac{c}{2nL} \frac{1 - r^2}{\pi r}. \tag{18}$$

Furthermore, the ratio of the FSR over the cavity linewidth is an important characteristic cavity parameter called the *finesse* F and is given by

$$F = \frac{\nu_{FSR}}{\Gamma} = \frac{\pi r}{1 - r^2}, \tag{19}$$

which is approximately $\pi/(1 - r^2)$ for mirrors with high reflectivity ($r \approx 1$). For a high finesse cavity, the transmission peaks are narrow compared to the FSR, such that the FP etalon essentially creates a narrow optical filter. The field that is reflected from the cavity E_R is the sum

of the direct reflection and the leakage beam from the intra-cavity field. The reflected field is given by

$$E_R = -rE_0 + E_0 \frac{t^2 r \cdot e^{-i\omega \frac{2nL}{c}}}{1 - r^2 \cdot e^{-i\omega \frac{2nL}{c}}}. \tag{20}$$

When the cavity is on resonance the amplitudes of the two contributions are of equal amplitude but of opposite phase, such that they destructively interfere, resulting in no reflected light from the cavity. When the cavity is near resonance, the phase of the reflected light field will depend greatly on the laser detuning $\Delta\nu$ from resonance, which will show to be very useful for stabilizing the laser frequency to the cavity resonance as is discussed further in section 2.5. Although the idealized scenario of plane waves traveling along the optical axis within a planar cavity is useful for understanding, it doesn't precisely represent a realistic cavity due to the infinite extension of plane waves in the transverse direction. In addition, a planar cavity will be very sensitive to misalignment, since a slight angle of the input beam will keep reflecting away from the optical axis until it is lost from the cavity completely. For this reason, a more realistic cavity, that is geometrically stable, needs to be considered.

2.4.2 Resonator stability

The geometrical stability of a Fabry-Pérot cavity can be parameterised using the cavity's g *factor*, which is given by

$$g \equiv g_1 g_2 = \left(1 - \frac{L}{R_1}\right)\left(1 - \frac{L}{R_2}\right), \tag{21}$$

where $g_{1,2}$ is the g factor of the individual cavity mirrors, which is dependent on the mirror's radius of curvature (ROC) $R_{1,2}$ [21]. For a stable cavity, the g factor should obey the *stability criterion*: $0 \leq g \leq 1$. This g factor can be interpreted as the magnification that an optical beam experiences after a round trip in the cavity. This criterion then implies that the optical beam should stay finite in size, even after several round trips. Figure 3 shows the resonator stability as a function of g_1 and g_2. A more in depth analysis of the cavity's geometrical stability and sensitivity to misalignment as a function of its g-factor is done in section 3.3.3. Now we have introduced the concept of a *stable* cavity and its g-factor, we can step away from the simplified plane wave picture, and introduce a more realistic one described with Gaussian beams.

2.4.3 Longitudinal & transverse modes

For a Gaussian beam that is confined in the cavity, the curvature of the wavefront should match the ROC of the mirrors. The beam radius at the cavity mirror surfaces, also referred to as *beam spots* $w_{1,2}$, is dependent on the chosen mirror configuration and radii of curvature. The beam

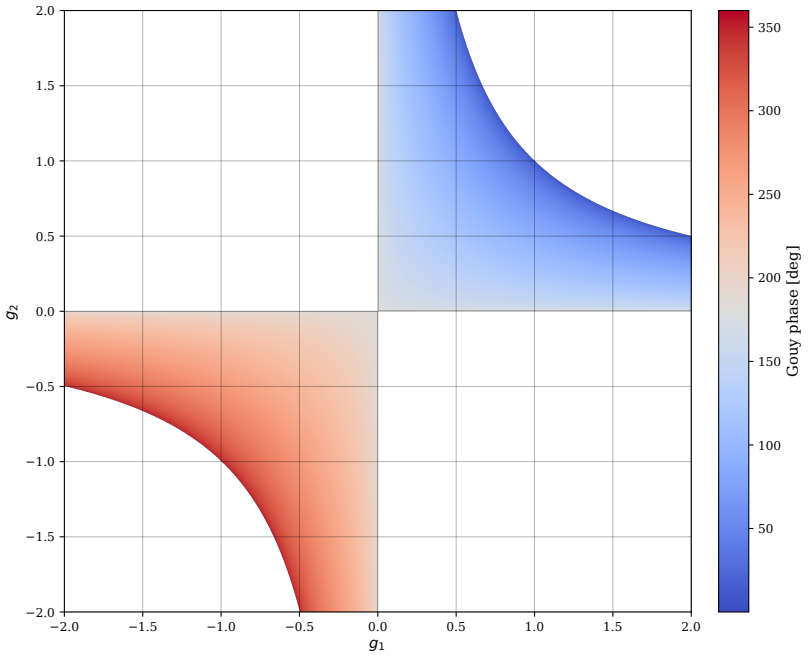


Figure 3: Resonator stability diagram. The shaded colored area satisfies the stability criterion $0 \leq g \leq 1$.

spot sizes can be calculated using propagation laws for Gaussian beams and are given by

$$w_1^2 = \frac{\lambda L}{\pi}\sqrt{\frac{g_2}{g_1(1-g_1g_2)}} \qquad \text{and} \qquad w_2^2 = \frac{\lambda L}{\pi}\sqrt{\frac{g_1}{g_2(1-g_1g_2)}}, \tag{22}$$

where the beam radius $w_{1/2}$ denotes the radius for which the laser intensity has fallen off to $1/e^2$ of the intensity at the beam center [21].

Besides the fundamental Gaussian mode, other optical modes can also form a stable cavity. Namely, the higher-order transverse electromagnetic modes TEM_{mn}, where m and n are integer mode numbers $(m,n = 0,1,2,...)$. These higher-order modes have a spatial-field distribution given by Hermite-Gauss functions, the product of a Hermite polynomial and a complex Gaussian function. Because of the transverse spatial confinement of the beam, the transverse momenta will be spread out, which creates a phase shift ζ compared to the fundamental mode [22]. This lag in phase is called the *Gouy* phase shift ζ and for a Fabry-Pèrot cavity it is given by

$$\zeta = 2\arccos(\pm\sqrt{g_1g_2}). \tag{23}$$

The additional phase shift that a higher-order m,n mode accumulates is then given by $\Delta\phi_{mn} = (m+n)\zeta$. The frequency offset of the higher-order mode from the fundamental mode is given by

$$\Delta\nu_{mn} = \frac{\Delta\phi_{mn}}{2\pi}\cdot\Delta\nu_{FSR} = (m+n)\cdot\frac{1}{\pi}\arccos(\pm\sqrt{g_1g_2})\cdot\Delta\nu_{FSR}, \tag{24}$$

from which we can see the transverse mode separation frequency $\Delta\nu_{TEM} = \Delta\nu_{mn}/(m+n)$. Now for a given longitudinal mode q, with frequency spacing $\Delta\nu_{FSR}$ and transverse mode m,n, the resonance frequencies are shifted compared to the simplified planar Fabry-Pérot cavity with

$$\nu_{mnq} = \Delta\nu_{FSR}\left(q + \frac{(m+n+1)}{\pi}\arccos(\pm\sqrt{g_1 g_2})\right). \tag{25}$$

If a higher-order mode is close to resonance at the same frequency as a fundamental mode, it is called higher-order mode degeneracy. This can create unwanted distortions in the beam and pull optical power from the fundamental mode. Furthermore, it can make it harder to stabilize the laser frequency to the cavity resonance, degrading the laser stabilization performance.

With a more in-depth theoretical understanding of optical cavities out of the way, lets look at how to actually *lock* the frequency of a laser to a cavity and consider which noise sources should be actively suppressed.

2.5 Laser stabilization to an optical cavity

In order to transfer the cavity's length stability $\frac{\Delta L}{L}$ to the laser's frequency stability $\frac{\Delta\nu}{\nu}$, the laser frequency needs to be locked to one of the cavity resonances. There exist several different techniques to stabilize the frequency of a laser to the resonance of an optical cavity. These techniques rely on comparing the laser's frequency with the resonance of the cavity and generating an error signal to provide feedback to the laser to suppress fluctuations in frequency [23]. The error signal can be generated from either the transmitted or reflected light from the cavity. Using the transmitted light one can directly lock to the side of a transmission fringe where the slope of the transmission peak converts frequency fluctuations into amplitude fluctuations in a so-called side-of-fringe lock. Whilst this method is elegant due to its simplicity, it has some notable drawbacks [24]; First of all, the bandwidth of the lock is limited to the linewidth of the cavity. Second, the technique is modulation-free, which means the error signal is detected at DC where there is more amplitude noise. Third, if the lock is perturbed and jumps to the other side of the resonance, the servo loop will push the laser away from the resonance, making it less robust. Fourth, the lock operates on the side of the resonance, so there will be less optical power in the cavity compared to the center of resonance, thus decreasing the signal-to-noise ratio of the transmitted light. Fortunately, there exist other approaches which use light that is reflected from the cavity to stabilize the laser frequency, such as the Hänsch-Couillaud (HC) [25] and the Pound-Drever-Hall (PDH) [23] technique.

The HC technique makes use of a polarization-dependent cavity resonance and derives its error signal from the polarization of the back reflected light, which again is detected at DC, making it sensitive to technical noise from the laser and photodetector. The PDH method circumvents all the aforementioned disadvantages and prevails over the HC technique by making

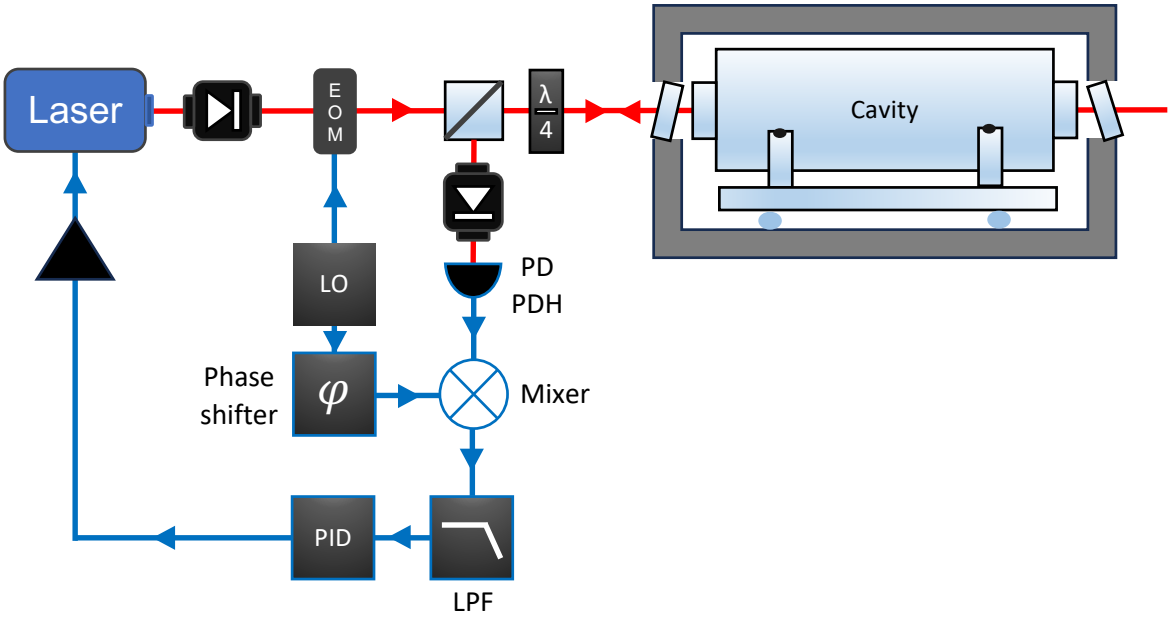


Figure 4: Schematic overview of the Pound-Drever-Hall locking technique. The local oscillator (LO) provides a modulation signal to the electro-optic modulator (EOM) for phase modulation, creating sidebands in frequency. The beat signal between the reflected sidebands and carrier is detected on a photodiode (PD). A portion of the LO signal is phase shifted and mixed with the beat signal to demodulate the signal. A low-pass filter (LPF) ensures that only the phase noise error is passed to the PID, from which the feedback signal is fed to the laser. Note that for a cavity with a polarization-dependent resonance, a Faraday rotator can be implemented instead of the quarter-waveplate ($\lambda/4$) in front of the cavity.

use of large modulation frequencies, avoiding detection at DC, making it insensitive to technical noise and thus it is the best option to create an ultrastable laser.

2.5.1 Pound-Drever-Hall locking

The PDH technique makes use of the phase of the light that is reflected from the cavity to generate an error signal. The phase of the reflected light shows a jump in phase depending on the sign of the detuning from the cavity's resonance as is depicted in figure 5b. The phase of the reflected light is antisymmetric across the cavity's resonance, making it possible to decide which side of the cavity resonance the laser's frequency is on. Unfortunately, a photo detector only measures the intensity of the light which does not contain the phase information explicitly. So an indirect determination of the phase needs to be employed. This is realised in the PDH method by phase-modulating the input light with an electro-optic modulator (EOM). The EOM is driven by a radio frequency signal to achieve a modulation frequency of Ω_m and modulation

depth β. A schematic overview of the PDH locking setup is depicted in figure 4. The light incident on the optical cavity is given by

$$E_I(t) = E_0 e^{i(\omega t + \beta \sin \Omega_m t)}, \tag{26}$$

where $\omega = 2\pi\nu$. When the modulation depth is small $\beta < 1$, most of the optical power is concentrated in the carrier and the first sidebands. The incident field can be rewritten using Bessel functions $J_n(\beta)$ as

$$E_I(t) \approx E_0[J_0(\beta)e^{i\omega t} + J_1(\beta)e^{i(\omega+\Omega_m)t} - J_1(\beta)e^{i(\omega-\Omega_m)t}]. \tag{27}$$

Now it is clear that the incident field consists of a carrier at the laser frequency ν and two sidebands at a frequency of $\nu \pm \Omega_m/2\pi$. If the modulation frequency is chosen to be much larger than the cavity linewidth $\Omega_m \gg \Gamma$, at resonance the carrier light is coupled into the cavity while the sidebands will be off-resonance and are directly reflected from the first cavity mirror. The light of the reflected sidebands now provides a phase reference for the carrier light that reflects from the cavity if the carrier is slightly off from the resonance center frequency by $\Delta\nu = \nu - \nu_0$. The difference in phase between the reflected sidebands and reflected carrier creates a modulation in the light intensity detected with a photodiode. The power of carrier and sidebands can be calculated with the reflection function $R(\omega)$, which for a symmetric and lossless cavity is given by

$$R(\omega) = \frac{E_R}{E_I} = \frac{r\left(e^{i\omega/\Delta\nu_{FSR}} - 1\right)}{1 - r^2 e^{i\omega/\Delta\nu_{FSR}}}, \tag{28}$$

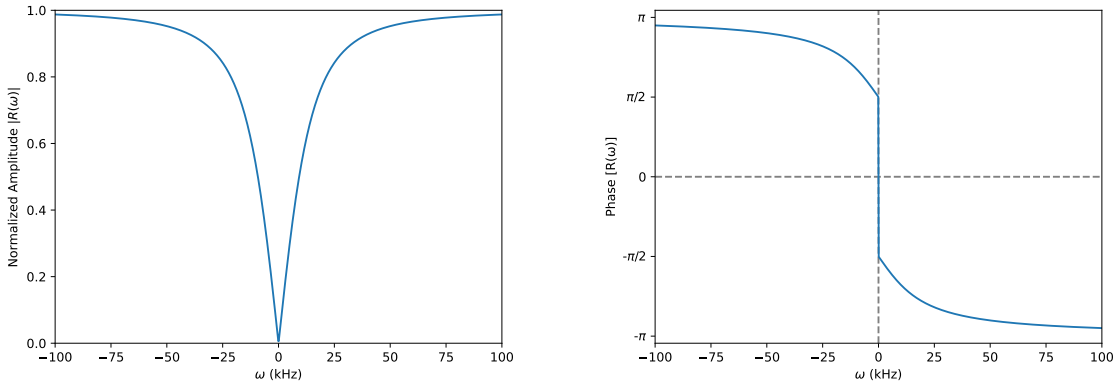
which has a Lorentzian shape if the detuning is small compared to the free spectral range $\Delta\nu \ll \Delta\nu_{FSR}$. The normalized amplitude of the reflection function and its phase are depicted in figure 5.

To create the error signal, the phase of the carrier needs to be related to the phase of the first-order sidebands in the beat signal of the reflected field. By applying $R(\omega)$ to our incident light the reflected power can be derived[2] and it is given by

$$P_R \approx 4P_c\left(\frac{\Delta\nu}{\Gamma}\right)^2 + 2P_s - 8\sqrt{P_c P_s}\left(\frac{\Delta\nu}{\Gamma}\right)\sin(\Omega_m t) - 2P_s\cos(2\Omega_m t), \tag{29}$$

where $P_c = J_0(\beta)^2 P_0$ and $P_s = J_1(\beta)^2 P_0$ are the power in the carrier and first-order sidebands respectively [26]. Now it is important to note that the reflected power P_R has a term that oscillates at the modulation frequency Ω_m that corresponds to the beating of the sidebands with the reflected carrier and its sign changes depending on which side of the cavity resonance the laser frequency is. The term that oscillates at $2\Omega_m$ corresponds to the beating of the two sidebands with each other and is not of interest to us. The beat signal can be fed to a mixer

[2]For a more detailed derivation see the introductory paper on PDH locking by Black [26].



(a) (b)

Figure 5: (a) shows the normalized cavity reflection coefficient $|R(\omega)|$ and (b) the phase of $R(\omega)$. For a cavity with a length of $L = 30$ cm and a finesse of $F = 100,000$.

where it is demodulated with a phase-matched signal from the same local oscillator that drives the EOM at the modulation frequency Ω_m, as is shown in figure 4. Next, the signal is low-pass filtered to get rid of the $\cos(2\Omega_m t)$ term. This will produce an error signal ϵ close to the cavity resonance ($\Delta\nu \ll \Gamma$). The error signal is proportional to the frequency detuning from resonance Δ, with an approximately linear slope D given by

$$\epsilon(\Delta\nu) \approx D \cdot \Delta\nu = -\frac{8\sqrt{P_c P_s}\Delta\nu}{\Gamma}. \tag{30}$$

A steeper slope corresponds to a better error signal since it is more sensitive to frequency fluctuations which are converted into an electronic signal. An example of a PDH error signal is depicted in figure 6.

In general, it is not possible to distinguish noise sources in the error signal, either coming from the laser frequency fluctuations or from optical path length fluctuations of the cavity. Therefore considering the cavity noise, the error signal near resonance is given by

$$\epsilon(\Delta\nu) \approx -\frac{8\sqrt{P_c P_s}\nu_0}{\Gamma}\left[\frac{\Delta\nu}{\nu_0} + \frac{\Delta L}{L}\right]. \tag{31}$$

In practise, the servo loop ensures that the fractional frequency deviations from cavity resonance $\frac{\Delta\nu}{\nu_0}$ is much smaller compared to the fractional optical path length fluctuations of the cavity $\frac{\Delta L}{L}$. Therefore, the fractional frequency instability of the laser will be given by the length stability of the cavity as

$$\frac{\Delta\nu}{\nu_0} = -\frac{\Delta L}{L}. \tag{32}$$

Unfortunately, there are noise sources that degrade the quality of the error signal and

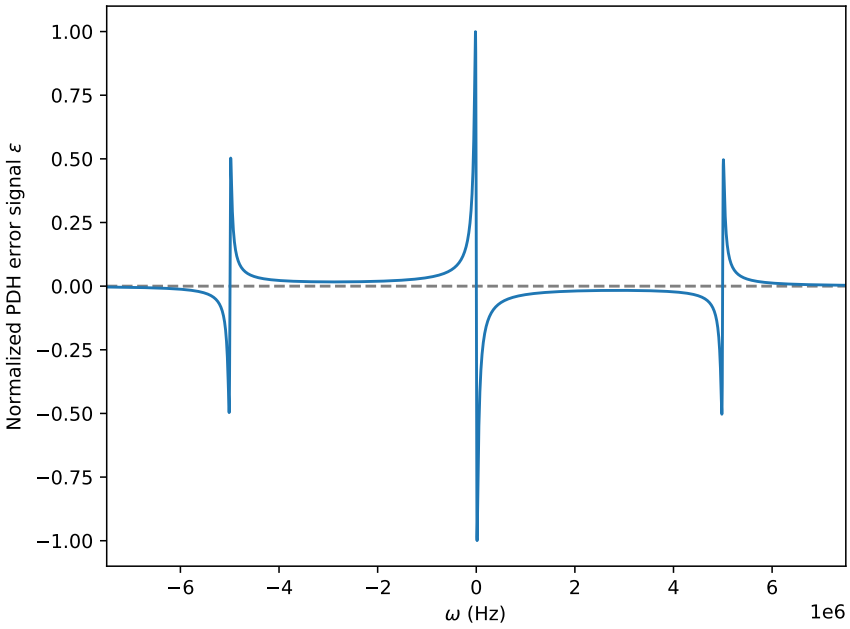


Figure 6: The normalized Pound-Drever-Hall error signal $\epsilon(\omega)$. For a modulation frequency $\Omega = 1\% \cdot \Delta\nu_{FSR} \approx 5$ MHz, $\beta = 1.08$, $L = 30$ cm and a cavity finesse of $F = 100,000$.

require active suppression, namely the *residual amplitude modulation* that is induced by the phase modulator.

2.5.2 Residual amplitude modulation

The error signal in the PDH technique should be equal to zero when the cavity is on resonance. When the symmetry around the carrier is broken, due to unequal magnitude in the sidebands, phase asymmetry or a combination of both, this leads to a DC offset of the locking point of the error signal [27]. The PDH servo loop will try to correct this DC offset by pulling the laser frequency away from the cavity resonance. If there is a perturbation that breaks this symmetry that is changing in time, this DC offset will also fluctuate in time, degrading the laser stabilization performance. The main time-dependent distortion of the symmetry of the sidebands comes from residual amplitude modulation (RAM).

There are multiple sources that can cause RAM. Such as the natural birefringence of the EOM crystal, if the polarization of the input light is not exactly aligned with the modulation axis of the EOM, a phase shift between the two optical field components will be induced that occurs at the modulation frequency of the EOM [28]. The polarizing beam splitter after the EOM will convert this into amplitude modulation of the light. Furthermore, the birefringence of the electro-optic crystal is in general dependent on temperature, so to minimize RAM fluc-

tuations the EOM should be temperature stabilized. Another source of RAM are parasitic etalons between the EOM and other optics in the optical path [29]. Etalons have a frequency-dependent amplitude and phase response that affects the sidebands differently. This effect can be suppressed by using anti-reflection (AR) coatings and slightly tilting optics in the beam path. Backscattering can also occur within the EOM crystal itself, for this reason, the EOM end facets can be cut at the Brewster's angle such that there occurs (almost) no internal reflection [30].

The fractional frequency instability σ_y induced by RAM can be denoted as

$$\sigma_y(t) = \sigma_{RAM}(t) \cdot \frac{\Gamma}{\nu}, \tag{33}$$

where σ_{RAM} is the Allan deviation of RAM fluctuations [31]. For a cavity with a linewidth of $\Gamma = 1.5$ kHz and operating at the clock transition frequency for strontium of $\nu \approx 429$ THz, the RAM fluctuations need to be below $\sigma_{RAM} < 3 \cdot 10^{-5}$ to be able to achieve a fractional frequency instability of $\sigma_y = 1 \cdot 10^{-16}$.

The effect of RAM can be suppressed to below $\sigma_{RAM} < 10^{-6}$ by implementing an active RAM stabilization scheme [31; 32]. A schematic overview of an active RAM stabilization setup is given in figure 7. The amplitude modulation that is induced by polarization modulation can be controlled precisely by applying a bias DC voltage in addition to the modulation frequency from the local oscillator via a bias tee. Since the amplitude modulation will be in phase with the phase modulation signal, the servo loop can suppress the RAM by compensating it with amplitude modulation with opposite amplitude[3].

Now, we have dealt with the RAM induced noise that disrupts the PDH error signal, we need to suppress any noise that has accumulated while sending the light from the laser to the cavity and finally to the atomic sample of the clock.

2.5.3 Fiber noise cancellation

To be able to operate an optical clock, the laser light needs to be transferred to the ultrastable cavity and further towards the atoms in the optical lattice. Additionally, if the stabilized light is to be compared to other stable sources from other laboratories, it would need to be distributed over a fiber link [33; 34]. In order to send the light from the laser to any destination, it has to travel through optical fibers or free space. However, the optical path length is sensitive to environmental perturbations, such as fluctuations in temperature and pressure as well as seismic and acoustic vibrations. These perturbations can cause a change in the geometric path length directly or cause a change in the refractive index in the medium the light is travelling through.

[3] A comprehensive explanation of how polarization modulation causes AM and a more thorough derivation of the RAM servo loop is given in the work of Hageman in appendix A [17].

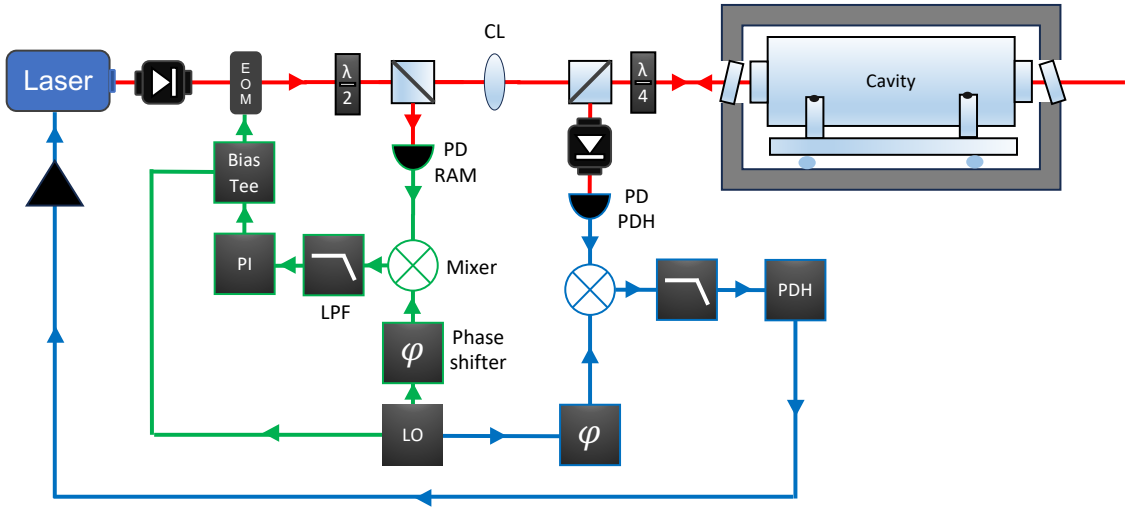


Figure 7: Schematic overview of an active RAM stabilization setup (in green). The elements in blue belong to the PDH locking scheme. The amplitude modulation of light intensity is detected on a photodiode (PD RAM) and demodulated with a phase-matched copy of the local oscillator (LO) signal in the mixer. The signal is low-pass filtered and a PI generates an appropriate DC signal which compensates RAM. The modulation from the LO and DC feedback are combined in the bias tee and fed to the EOM.

The combination of all these effects adds phase noise to the transmitted light degrading its stability [35].

For a fiber of length L, refractive index of the core n_f, the phase noise is dependent on the temperature T and pressure P. A changing laser phase in the fiber induces an instantaneous frequency change $\Delta\nu_f$ given by

$$\Delta\nu_f = \frac{d\phi_f}{dt} = \frac{2\pi}{\lambda}\left(\frac{d}{dt}\left[n_f(T,P)\cdot L(T,P)\right]\right), \tag{34}$$

where the fiber length L itself also depends on temperature and pressure due to thermal and mechanical expansion of the glass core [36]. The variations in refractive index are the dominant contribution, such that the thermal and mechanical expansion term $dL(T,P)/dt$ can be neglected. The resulting Doppler shift of the light inside the fiber is approximately given by

$$\Delta\nu_f \approx \frac{2\pi L}{\lambda}\left[\frac{dn_f}{dT}\frac{dT}{dt} + \frac{dn_f}{dP}\frac{dP}{dt}\right]. \tag{35}$$

So to maintain frequency stability during the transfer of light it is crucial to compensate for the phase noise that the light acquires between its source and destination depending on the environmental conditions and distance the light has to travel. This can be achieved by implementing a fiber noise cancellation (FNC) scheme. A schematic overview of the FNC scheme

is given in figure 8 [35; 37]. In this scheme the frequency of the light is compared before and after a round trip through the fiber link and the resulting shift in frequency caused by fiber noise is corrected for. To create a round trip for the light, a partial mirror is placed after the fiber to form an interferometer. In this Michelson interferometer that is created, the stability of the short stable arm is transferred to the long arm by stabilizing the phase of the long arm to the short reference arm with a phase-locked loop (PLL). An acousto-optic modulator (AOM) is placed in the long arm to compensate for frequency shifts induced by fiber noise f_N. The AOM itself also shifts the frequency by f_{AOM}. Since the back reflected light passes through the fiber and AOM twice it will accumulate a frequency shift of $2\cdot(f_{AOM}+f_N)$ [4]. A photodiode (PD) measures the beat signal between the light from before and after the round trip. The resulting beat note will oscillate at $2\cdot(f_{AOM}+f_N)$. To isolate the fiber noise contribution in the beat note it is demodulated by mixing with a reference signal that has a frequency of $2f_{AOM}$. Next, a PID continuously compensates this fiber noise f_N by changing the driving frequency of the AOM with a voltage-controlled oscillator (VCO) to $f'_{AOM} = f_{AOM} - f_N$, cancelling the fiber noise.

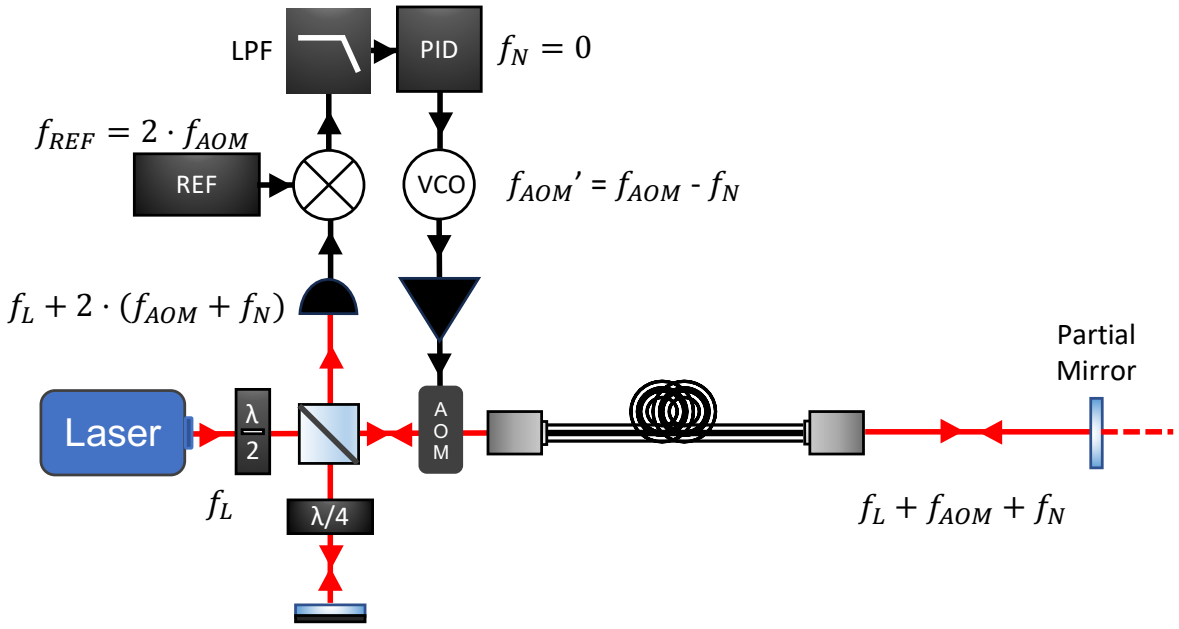


Figure 8: Schematic overview of a fiber noise cancellation scheme. The partial mirror back-reflects a portion of the light, creating an interferometer. A photodiode (PD) detects the beat signal of the light before and after a round trip. It is demodulated by mixing with a reference signal at $2f_{AOM}$. A PID adjusts the voltage of the VCO, changing the AOM frequency to correct for phase fluctuations due to fiber noise.

In addition to the AOM that compensates the fiber noise, a second *marker* AOM can be

[4] It is assumed that the round trip fiber noise is equal to twice the one-way trip noise.

placed at the end of the long arm after the fiber. This marker AOM shifts the frequency of the light coming back from the reflecting mirror, such that the reflected light can be more easily distinguished from any other light coming back due to unwanted reflections from other optical surfaces.

With the ability of phase-stabilizing fiber-links, we can distribute and compare time and frequency standards. The light is transferred over optical fiber links that typically operate in the telecom C-band, a wavelength range of 1530 - 1565 nm. In general, the frequency of the clock lasers (e.g. strontium has a clock transition at 698 nm) do not fall inside the C band. Hence, the stability of the clock laser needs to be transferred to another laser that operates in the telecom C-band. Such a transfer of stability is done using an optical frequency comb (OFC) in a scheme known as the transfer oscillator scheme.

2.6 Stability transfer using a frequency comb

The scheme to transfer the frequency stability uses a femtosecond frequency comb. A schematic overview of the frequency comb with the relevant frequencies is given in figure 9. The teeth of the frequency comb are given by $\nu_N = Nf_{rep} + f_0$, where f_{rep} is the repetition rate of the comb and f_0 is the carrier-envelope-offset (CEO) frequency. The scheme is based on the transfer-oscillator technique, in which the frequency stability of a master laser with frequency ν_M, is transferred to a slave laser with frequency ν_S [38; 39]. Both ν_M and ν_S must fall in the spectral range of the OFC, such that the comb can provide a phase-coherent link between the two frequencies. The transfer of frequency stability is based on the detection of beat notes between comb modes and the continuous wave (CW) field of the master and slave lasers. These beat notes contain information about the relative frequency fluctuations between the master and slave laser. This makes it possible to phase-lock the slave laser to the master laser through the OFC, transferring the stability of the master to the target slave laser. A schematic overview of the transfer oscillator technique is given in figure 10 which is explained in more detail in the following.

The beat notes between the frequency comb and master laser (f_M) and between comb and slave laser (f_S), are given by

$$f_M = \nu_M - N_M f_{rep} - f_0, \tag{36}$$

$$f_S = \nu_S - N_S f_{rep} - f_0, \tag{37}$$

where f_{rep} and f_0 are technical parameters of the frequency comb and are in principle not ultrastable. Thus, to be able to determine the beat frequency precisely, the repetition rate f_{rep} and carrier-envelope-offset f_0 need to be stabilized to eliminate them from equations for the beat note frequencies f_M and f_S. The carrier-envelope-offset frequency f_0 can be detected

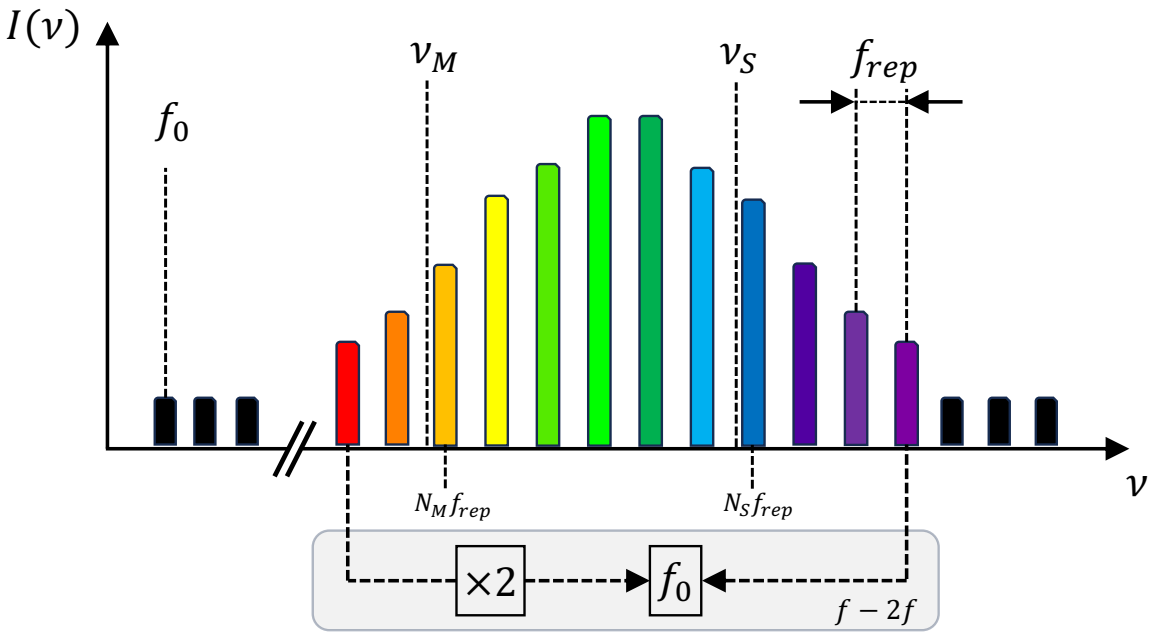


Figure 9: Schematic overview of the frequency comb and all the relevant frequencies. The carrier-envelope-offset frequency is given by f_0 and can be determined using the $f-2f$ interferometer technique depicted in the gray box. The repetition rate is given by f_{rep} and the master and slave laser frequencies are given by ν_M and ν_S respectively.

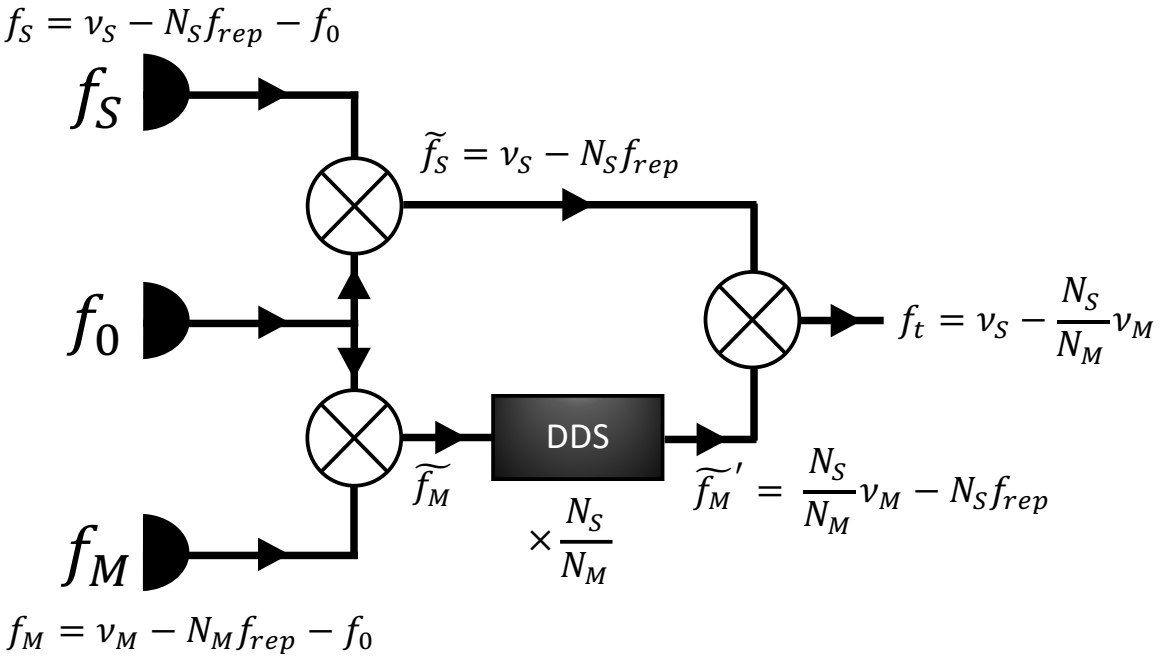


Figure 10: Schematic overview of the transfer oscillator scheme. First, the carrier-envelope-offset frequency f_0 is mixed out of the optical beat notes f_M and f_S. Second, $\tilde{f}_M$ is multiplied by a factor of N_S/N_M using a phase locked DDS. Third, the repetition rate f_{rep} is mixed out to be left with a virtual beat note f_t relating the master and slave frequencies f_M and f_S independent of any comb parameters.

using the $f-2f$ interferometer technique [40]. This technique produces a heterodyne beat at f_0 by self-referencing between two ends of the frequency spectrum that the comb spans. Comb light at the low-frequency end is frequency doubled and interfered with the fundamental light at twice its frequency, giving the relation

$$2 \cdot \nu_N - \nu_{2N} = 2 \cdot (N f_{rep} + f_0) - (2N \cdot f_{rep} + f_0) \tag{38}$$

$$= f_0. \tag{39}$$

Now it is possible to mix out the CEO frequency f_0 out of the optical beat notes f_M and f_S, the resulting frequencies are then given by

$$\tilde{f}_M = \nu_M - N_M f_{rep} \tag{40}$$

$$\tilde{f}_S = \nu_S - N_S f_{rep}. \tag{41}$$

To eliminate f_{rep}, one of the beat notes, either $\tilde{f}_M$ or $\tilde{f}_S$ is multiplied by a factor of N_S/N_M or N_M/N_S respectively, using a direct digital synthesizer (DDS). If we choose to phase lock the

DDS to $\tilde{f}_M$ and multiply the frequency by N_S/N_M we get

$$\tilde{f}'_M = \frac{N_S}{N_M}\nu_M - N_S f_{rep} \tag{42}$$

The resulting beat notes are mixed to get a repetition rate free expression f_t given by

$$f_t = \nu_S - \frac{N_S}{N_M}\nu_M. \tag{43}$$

This expression is independent of any comb parameters f_0 and f_{rep} and thus free of noise that is introduced in the stabilization of these parameters. By measuring the ADEV of the virtual beat note f_t the relative frequency instability between the the master and slave laser can be determined. Finally, to actually transfer the frequency stability, the frequency of the slave laser ν_S is locked to the virtual beat note f_t, such that the slave laser is forced to follow the residual frequency fluctuations of the master laser.

To summarize, the frequency comb allows for the transfer of frequency stability from one oscillator to another, and to measure the relative frequency instability between two oscillators separated far in frequency. In practice, the stability performance of such oscillators are benchmarked by comparing three similar oscillators. This is known as a *three-cornered-hat* (TCH) comparison.

2.7 Three-cornered hat comparison

In general the frequency instability of an oscillator σ_A can be determined by comparing the instability relative to that of a second oscillator σ_B. The relative instability between the two oscillators σ_{AB} can be obtained by measuring the beat signal with frequency counters giving

$$\sigma^2_{AB} = \sigma^2_A + \sigma^2_B - \frac{1}{(N-1)}\sum_{i=1}^{N-1}\left(\overline{y}_{i+1} - \overline{y}_i\right)_A\left(\overline{y}_{i+1} - \overline{y}_i\right)_B, \tag{44}$$

where the last term gives the correlation between the two oscillators [41]. Crucially, it is impossible to know which of the two oscillators is the limiting factor in the comparison. To get a valid determination of the frequency stability of oscillator A, the frequency stability of the reference oscillator B needs to exceed that of A such that $\sigma_B \ll \sigma_A$.

For this reason, whenever a new oscillator is developed with the premise to have superior frequency stability than the former oscillators, two identical copies need to be constructed to get a measure of the frequency instability. Since identical oscillators will both contribute to half of the measured variance σ_{AB}. Luckily, there exists an alternative technique whenever there are no two identical copies of an oscillator available, the so-called *three-cornered hat* method.

The TCH method consists of three oscillators; one under test (A) and two reference oscillators (B & C). For completely independent oscillators the correlation term for the relative

frequency instability of equation 44 will vanish leaving us with the set of equations for the variances

$$\sigma_{AB}^2 = \sigma_A^2 + \sigma_B^2, \tag{45}$$

$$\sigma_{AC}^2 = \sigma_A^2 + \sigma_C^2, \tag{46}$$

$$\sigma_{BC}^2 = \sigma_B^2 + \sigma_C^2. \tag{47}$$

From this set of equations we can derive the instabilities of the individual oscillators given by

$$\sigma_A^2 = \frac{1}{2}\left(\sigma_{AB}^2 + \sigma_{AB}^2 - \sigma_{BC}^2\right), \tag{48}$$

$$\sigma_B^2 = \frac{1}{2}\left(\sigma_{AB}^2 + \sigma_{BC}^2 - \sigma_{AC}^2\right), \tag{49}$$

$$\sigma_C^2 = \frac{1}{2}\left(\sigma_{AC}^2 + \sigma_{BC}^2 - \sigma_{AB}^2\right). \tag{50}$$

Unfortunately, the TCH method is also sensitive to cross-correlations between the oscillators; two oscillators that are placed on the same optical table can experience the same seismic noise, which could be interpreted as a frequency deviation of the third oscillator in the comparison. When correlations between oscillators are present it is possible to utilize more oscillators to increase the confidence in the measured instability [42].

3 Design of an ultra-stable optical cavity

In atomic clocks, the local oscillator is typically provided by a laser with frequency ν, which is locked to one of the resonant modes of an ultrastable Fabry-Pérot cavity with optical path length L. When the laser is locked to a cavity resonance, the frequency stability of the laser is approximately equal to the optical path length stability of the cavity. A small fluctuation in optical path length ΔL will result in a fluctuation in laser frequency $\Delta\nu$, following

$$\frac{\Delta\nu}{\nu} = -\frac{\Delta L}{L}, \tag{51}$$

where the ratios $\frac{\Delta\nu}{\nu}$ and $\frac{\Delta L}{L}$ represent the relative frequency stability of the laser and relative length stability of the cavity respectively.

The creation of an ultra-stable frequency reference is thus dependent on our ability to stabilize the optical path length between the cavity mirrors. Several external noise sources such as temperature and pressure fluctuations along with vibrations can degrade the length stability of the cavity. These effects can be reduced by careful engineering of the thermal enclosure, vacuum chamber and vibration isolation platform. Finally, the ultimate length stability that is achievable is limited by the inherent thermal noise of the cavity.

3.1 Thermal noise limit

Thermal noise can broadly be divided into two parts; Brownian noise and thermo-optic noise. Brownian motion originates from elastic energy dissipation causing thermal motion. Elastic energy is the energy that is stored in an object when it is temporarily deformed. The dissipation rate of this stored energy is dependent on the inverse of the mechanical quality factor Q of the material. In case of an optical cavity, the consequent thermal motion shows as local random displacements in the cavity spacer, mirror substrates and mirror coatings. Thermo-optic (TO) noise additionally has two contributors; thermo-elastic (TE) and thermo-refractive (TR). TE noise is defined as noise resulting from differences in thermal expansion due to local temperature fluctuations. TR noise arises from local differences in the index of refraction due to temperature fluctuations. Noise from Brownian motion is the dominant contributor to thermal noise and thus sets a fundamental limit to the length stability that one can achieve.

A powerful way to estimate the effect of thermal noise is the "direct-approach" that was proposed by Levin [43][5]. This method is fundamentally based on the fluctuation-dissipation theorem, introduced by Callen and Welton [45]. The fluctuation-dissipation theorem relates the random Brownian motion of atoms to thermodynamical loss in the system. Local dissipative losses on the mirror surfaces lead to local displacements, which in turn lead to phase distortions

[5] With consideration of corrections from Liu and Thorne [44]

of a reflected wavefront. The direct-approach method will be examined more closely in the following.

For Fabry-Pérot resonators, the average distance between the cavity mirrors experienced by the electric field of the laser is represented by $x = x_1 - x_2$, the coordinate describing the length fluctuations. From the fluctuation-dissipation theorem, Levin retrieves an expression for the power spectral density $S_x(f)$ of thermal fluctuations of x, given by

$$S_x(f) = \frac{2k_BT}{\pi^2 f^2}\frac{W_{diss}}{F_0^2} \tag{52}$$

where k_B is the Boltzmann constant, T denotes the absolute temperature and W_{diss} describes the time-averaged dissipated power when the system is subject to an oscillating force of amplitude F_0 and frequency f.

The direct-approach method considers a situation where the dissipation in the system is homogeneously distributed such that W_{diss} can be expressed as

$$W_{diss} = 2\pi f U_{max}\phi(r,f), \tag{53}$$

where U_{max} is the maximum elastic strain energy and $\phi(r,f)$ is the loss angle[6] of the total system, that describes the damping of the system due to elastic energy dissipation. The loss angle is the reciprocal of the mechanical quality factor $Q(f)$ such that a smaller loss angle corresponds to a lower damping rate and thus a lower energy loss rate.

The total thermal noise of the cavity is the sum of the contributions from all the cavity components; the spacer $S_x^{(sp)}$, mirror substrates $2\cdot S_x^{(sb)}$ and mirror coatings $2\cdot S_x^{(ct)}$. So the total thermal noise is given as

$$S_x = S_x^{(sp)} + 2\cdot S_x^{(sb)} + 2\cdot S_x^{(ct)} \tag{54}$$

$$= \frac{4k_BT}{\pi f F_0^2}\left(U_{max}^{(sp)}\phi_{sp} + 2\cdot U_{max}^{(sb)}\phi_{sb} + 2\cdot U_{max}^{(ct)}\phi_{ct}\right). \tag{55}$$

The maximum elastic strain energy U_{max} of each component is dependent on its geometry and material properties. A lot of theoretical work has gone into deriving accurate analytical expressions for U_{max} of each component. Following Levin's direct approach and assuming negligible effects from the mirrors, Numata *et al.* [12] derived an expression of$U_{max}^{(sp)}$ for a cylindrical spacer. Furthermore, the expression given by Numata *et al.* was improved by Kessler *et al.* by implementing two corrections[7] [46]. The corrected expression for $S_x^{(sp)}(f)$ is given by

$$S_x^{(sp)}(f) = \frac{4k_BT}{2\pi f}\frac{L}{A_{sp}Y_{sp}}\phi_{sp}, \tag{56}$$

[6]Conventionally the loss angle $\phi(f)$ is written as the imaginary component of the Young's modulus $Y = Y_0\left(1 + i\phi(r,f)\right)$

[7]Kessler's calculation differs in two ways. First, it takes into account that the area of the front face of the spacer is reduced by the central bore. Second, it considers correlated length fluctuations from both ends of the spacer.

where Y_{sp} is the spacer material's Young's modulus and $A_{sp} = \pi(R_{sp}^2 - R_{bore}^2)$ is the face area of a cylindrical spacer with a borehole of radius R_{bore}. By treating both cavity mirrors as an infinite half-space[8], defined as a mirror with infinite radius and depth, the mirror substrates contribution to the length fluctuation PSD is given as

$$S_x^{(sb)}(f) = \frac{4k_BT}{2\pi f}\frac{1-\sigma_{sb}^2}{\sqrt{\pi}Y_{sb}w}\phi_{sb}, \tag{57}$$

where σ_{sb} is the Poisson ratio and Y_{sb} denotes the Young's modulus of the substrate material [43; 47]. The mirror coating contribution was estimated by Nakagawa *et al.* by treating the mirror coating as a thin layer on the substrate, with similar elastic properties of coating and substrate [48]. In this case, the contribution of the coating becomes

$$S_x^{(ct)}(f) = \frac{4k_BT}{2\pi f}\frac{2(1+\sigma_{sb})(1-2\sigma_{sb})d_{ct}}{\pi Y_{sb}w^2}\phi_{ct}, \tag{58}$$

where d_{ct} is the thickness of the mirror coating. In reality, the coating and substrate will have differing elastic properties, which was taken into account by Harry *et al.* [49]. This gave rise to the following extended expression for the coating contribution to the PSD $S_x^{(ct)}(f)$

$$S_x^{(ct)}(f) = \frac{2k_BT}{\pi f}\frac{Y_{ct}^2\cdot(1+\sigma_{sb})^2\cdot(1-2\sigma_{sb})^2 + Y_{sb}^2\cdot(1+\sigma_{ct})^2\cdot(1-2\sigma_{ct})}{\pi Y_{sb}^2 Y_{ct}\cdot(1-\sigma_{ct}^2)}\frac{d_{ct}}{w^2}\phi_{ct}. \tag{59}$$

Note that equation 59 reduces to equation 58 under the assumption of equal elastic properties of coating and substrate: $Y_{ct} = Y_{sb}$ and $\sigma_{ct} = \sigma_{sb}$.

The fractional frequency stability of the laser is directly proportional to the fractional length stability of the cavity, as shown in equation 51. The PSD of length fluctuations $S_x(f)$ can be converted to the PSD of fractional frequency fluctuations $S_y(f)$ by

$$S_y(f) \equiv \frac{S_\nu(f)}{\nu^2} = \frac{S_x(f)}{L^2}. \tag{60}$$

The frequency instability in the time domain is typically characterized by the Allan deviation σ_y of fractional frequency fluctuations y [50]. The Allan deviation σ_y can be expressed using the PSD $S_y(f)$ with

$$\sigma_y = \sqrt{2\ln(2)S_y(f)f}. \tag{61}$$

Since $S_y(f)$ has a $1/f$ dependency (flicker frequency noise), as can be seen in equation 55, the resulting Allan deviation will be constant and is therefore called the *thermal noise floor* of the cavity.

[8] Bondu *et al.* was able to refine the expression for a finite-size mirror. However, typically the beam waist is much smaller compared to the mirror size, such that the mirror can be approximated as an infinite half-space with good accuracy [47].

3.2 Reduction of thermal noise in optical cavities

By looking at the equations for the thermal noise contributions of the spacer (Eq. 56), mirror substrates (Eq. 57) and mirror coatings (Eq.58) one can think of ways to reduce the total thermal noise of an optical cavity. The parameters from these equations that affect the thermal noise floor σ_y are temperature T, beam radius w, coating thickness d_{ct}, loss angles $\phi_{sp/sb/ct}$, cavity material's Young's moduli $Y_{sp/sb/ct}$ and Poisson ratio's $\sigma_{sb/ct}$. Additionally, equation 60 shows the inverse proportionality of the thermal noise floor with cavity length L.

Unfortunately, these parameters cannot be chosen freely, the choices are restricted due to practical limitations. Ideally, the temperature T can be reduced to cryogenic regimes. In that case one needs to carefully choose the spacer material (e.g. mono-crystalline silicon cavities [17; 51]). Otherwise, the optical cavities operating around the room temperature commonly employ spacer made of ultra low expansion (ULE[9]) glass. To summarize, the thermal noise floor of the cavity is heavily dependent on the material properties from which it is built.

3.2.1 Cavity materials

Modern optical cavities are typically made up of two high-reflectivity mirror coatings attached to fused silica (FS) mirror substrates, which are optically contacted to a spacer made from a material with a small coefficient of thermal expansion (CTE). The material's CTE describes the length change of an object with temperature. For cavities operating around room temperature the spacer is often made from ULE, which has a CTE of 0 ± 30 ppb/K [52]. All relevant material properties of ULE and FS are depicted in table 2.

An old practice was to construct both the spacer and the substrate out of ULE material. However, Numata *et al.* proposed to reduce the dominant mirror substrate noise contribution by replacing the ULE substrates with fused silica, since the loss angle of fused silica ($\phi_{FS} < 1 \cdot 10^{-6}$) is considerably lower compared to ULE ($\phi_{FS} = 1.6 \cdot 10^{-5}$) [12]. Furthermore, the CTE mismatch between the ULE spacer ($0 \pm 0.03 \cdot 10^{-6}$/K) and FS mirror substrate ($0.52 \cdot 10^{-6}$/K) resulting in mirror deformation, can be compensated by attaching ULE rings to the back of the FS substrate [53].

With the use of fused silica as the material of choice for the mirror substrates, the reduced mechanical loss has pushed the mirror substrate contribution to the thermal noise PSD S_y to a minor level. In current state-of-the-art cavities using conventional dielectric mirrors, which are typically alternating $\lambda/4$-layers of Ta_2O_5 and SiO_2, the mirror coatings have become the dominant contributor to the thermal noise floor of the system, as is depicted in figure 11. For this reason, it has become a topic of great interest to find new coating materials with lower loss

[9] ULE ® is a registered brand of ultra-low-expansion glass made with TiO_2 doped silica from Corning Inc.

Table 2: Geometrical and mechanical properties of cavity materials required to calculate the thermal noise floor of the cavity. Values for cavity length and spacer radius are preliminary and will be discussed further in section 3.3.

Parameter	**Definition**	**Value**
L	Cavity length	30 cm
A_{sp}	Spacer face area	$\pi\left(R_{sp}^2 - R_{bore}^2\right)$
R_{sp}	Spacer radius	4 cm
R_{bore}	Bore radius	4 mm
d_{ct}	Coating thickness	10 μm
ϕ_{ULE}	ULE loss angle	$1.7 \cdot 10^{-5}$
ϕ_{FS}	Fused silica loss angle	$1 \cdot 10^{-6}$
$\phi_{crystal}$	$Al_{0.92}Ga_{0.08}As$/GaAs loss angle	$2.5 \cdot 10^{-5}$
$\phi_{dielectric}$	Ta_2O_5/SiO_2 loss angle	$4 \cdot 10^{-4}$
σ_{ULE}	ULE Poisson's ratio	0.17
σ_{FS}	Fused silica Poisson ratio	0.17
Y_{ULE}	ULE Young's modulus	67.7 GPa
Y_{FS}	Fused silica Young's modulus	73.1 GPa

angles ϕ. A promising recent coating candidate, crystalline $Al_{0.92}Ga_{0.08}As$/GaAs, is proven to provide an order of magnitude lower mechanical loss angle ($\phi_{crystal} = 2.5 \cdot 10^{-5}$) compared to conventional mirrors [15]. With crystalline mirrors, the thermal noise contribution is no longer the dominant one, as can be seen in figure 12. A comparison between dielectric and crystalline mirrors and the resulting thermal noise floor is depicted in figure 13 and the relevant coating properties are shown in table 2.

3.2.2 Mirror configurations & Spacer length

Another influential parameter on the thermal noise floor is the beam radius w at the mirror surfaces. In the equations for the thermal noise PSD the substrate and coating contributions (Eq. 57 and 58) scale with $1/w$ and $1/w^2$ respectively. Meaning, that an increased beam radius at the mirror surfaces results in a lower thermal noise floor.

The beam radius at the cavity mirror surfaces, also referred to as *beam spots* $w_{1/2}$, are dependent on the chosen mirror configuration and radii of curvature as discussed in section 2.4.3. Using equation 22 we can calculate the beam spot size for different mirror configurations and ROCs. The resulting beam spot sizes and thermal noise floors for dielectric and crystalline

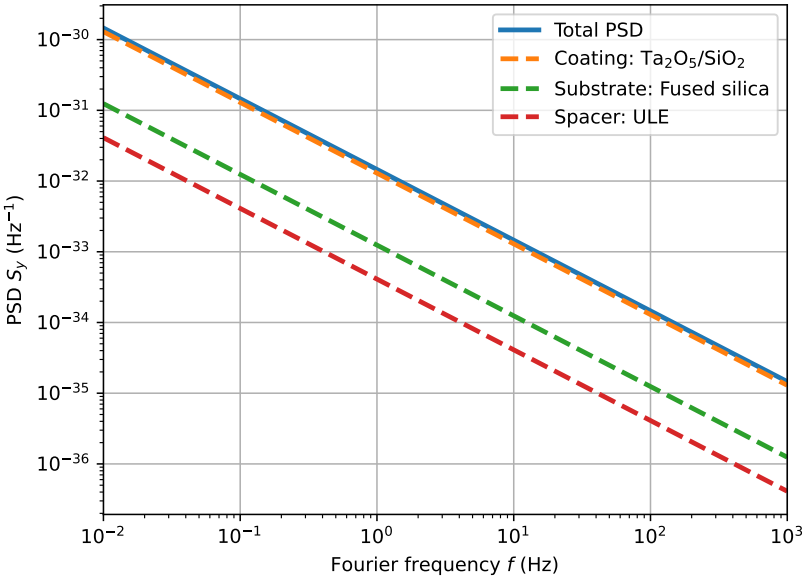


Figure 11: Thermal noise PSD S_y contributions from ULE spacer, FS substrates and dielectric Ta_2O_5/SiO_2 mirror coatings in planar-concave ($\mathscr{R}_1/\mathscr{R}_2$ = 1 m/∞ m) configuration using light with a wavelength of $\lambda = 698$ nm. The resulting thermal noise floor is $\sigma_y = 1.4 \cdot 10^{-16}$.

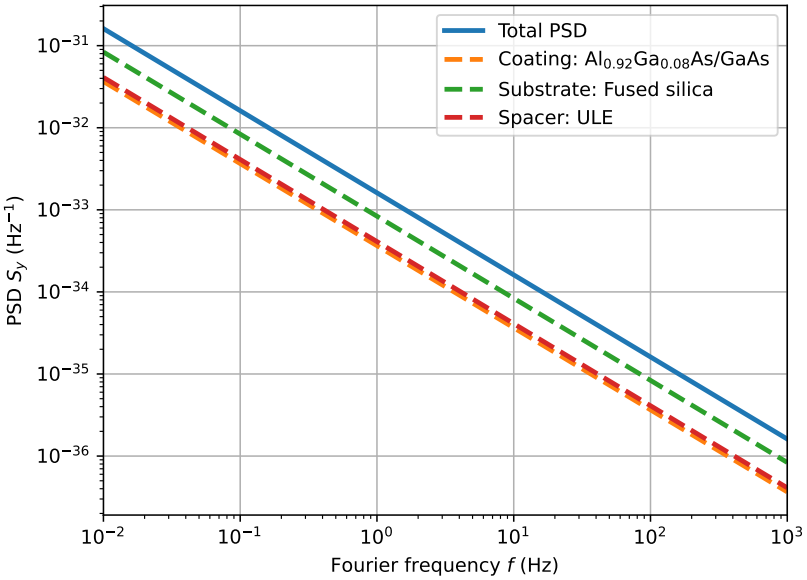


Figure 12: Thermal noise PSD S_y contributions from ULE spacer, FS substrates and crystalline $Al_{0.92}Ga_{0.08}As/GaAs$ mirror coatings in planar-concave ($\mathscr{R}_1/\mathscr{R}_2$ = 1 m/∞ m) configuration using light with a wavelength of $\lambda = 1542$ nm. The resulting thermal noise floor is $\sigma_y = 4.7 \cdot 10^{-17}$.

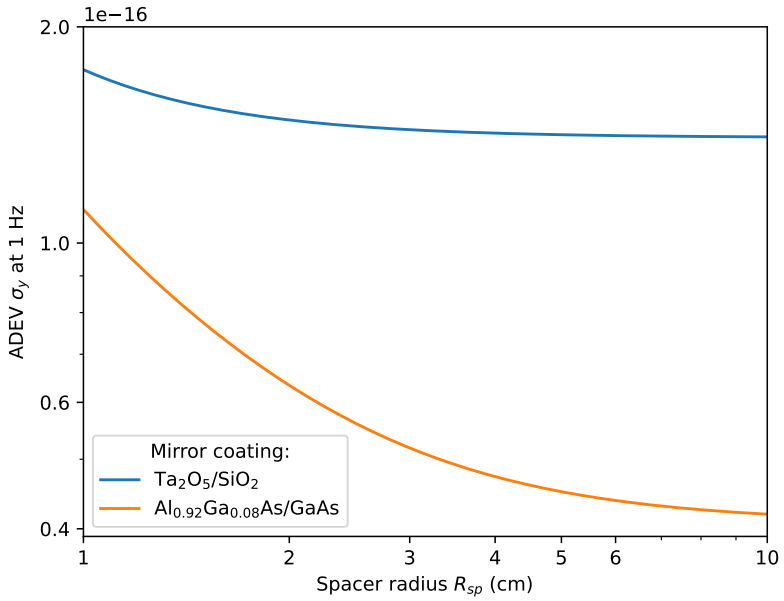


Figure 13: Thermal noise floor σ_y versus spacer radius for dielectric Ta_2O_5/SiO_2 and crystalline $Al_{0.92}Ga_{0.08}As/GaAs$ mirror coatings. The bore radius is set to $R_{bore} = 4$ mm.

mirrors are depicted in table 3 and 4 respectively. The reduction of the thermal noise floor for increasing spot size can be intuitively understood by the fact that for a larger mode size the thermal fluctuations are averaged over a larger surface area.

In section 3.1 the inverse proportionality of the thermal noise floor with cavity length was shown. Similar to the operating temperature of the cavity, we cannot choose the cavity length freely. In general, a longer cavity has a larger vibration sensitivity, which makes it more difficult to sufficiently suppress length changes caused by vibrations. The thermal noise floor for different mirror configurations as a function of spacer length is depicted in figure 14

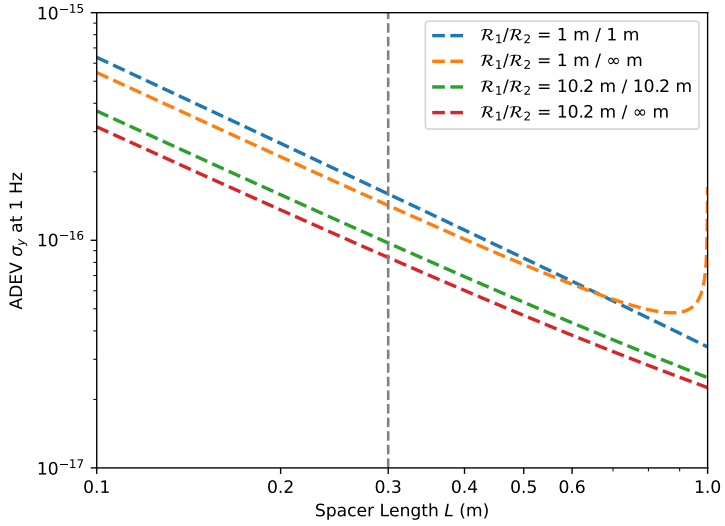


Figure 14: Thermal noise floor σ_y at 1 Hz versus cavity length for dielectric Ta_2O_5/SiO_2 mirror coatings with different ROC configurations ($\mathcal{R}_1/\mathcal{R}_2$). The thermal noise floor values are shown in table 3.

Table 3: Thermal noise floor σ_y for different cavity mirror configurations with a $L = 30$ cm ULE spacer, fused silica substrates and dielectric Ta_2O_5/SiO_2 mirror coatings at a temperature of $T = 295$ K using light with a wavelength of $\lambda = 698$ nm. The relevant material parameters used in the thermal noise floor calculation can be found in table 2.

Mirror ROC $\mathcal{R}_1/\mathcal{R}_2$	**Beam spot size** w_1/w_2	**Thermal noise floor** σ_y
1 m / 1 m	306 / 306 μm	$1.6 \cdot 10^{-16}$
1 m / +∞ m	381 / 319 μm	$1.4 \cdot 10^{-16}$
10.2 m / 10.2 m	526 / 526 μm	$9.7 \cdot 10^{-17}$
10.2 m / +∞ m	628 / 619 μm	$8.4 \cdot 10^{-17}$

Table 4: Thermal noise floor σ_y for different cavity mirror configurations with a $L = 30$ cm ULE spacer, fused silica substrates and crystalline $Al_{0.92}Ga_{0.08}As/GaAs$ mirror coatings at a temperature of $T = 295$ K using light with a wavelength of $\lambda = 1542$ nm.

Mirror ROC $\mathcal{R}_1/\mathcal{R}_2$	**Beam spot size** w_1/w_2	**Thermal noise floor** σ_y
1 m / 1 m	454 / 454 μm	$5.0 \cdot 10^{-17}$
1 m / +∞ m	567 / 474 μm	$4.7 \cdot 10^{-17}$
10.2 m / 10.2 m	782 / 782 μm	$3.9 \cdot 10^{-17}$
10.2 m / +∞ m	934 / 920 μm	$3.7 \cdot 10^{-17}$

3.3 Mechanical instability

To make sure that an optical cavity is able to achieve thermal-noise-limited performance, the mechanical stability of the resonator needs to be sufficient to suppress environmental perturbations that can alter the optical path length of the cavity. The cavity design needs to ensure that changes in optical path length are minimized while uniform forces are applied to the cavity. This is particularly important for long optical cavities that aim for a low thermal noise floor of 10^{-16} since they are intrinsically more sensitive to external perturbations. Ultrastable cavity designs typically make use of symmetry to create a system insensitive to accelerations. Several different cavity designs have previously been implemented with differing cavity spacer shapes; such as the *mushroom* type [54], a spherical design [55] or with a rectangular spacer [56; 57]. More recent designs that aim for higher performance opt for cylindrical spacers [13; 14]. A cylindrical spacer offers an enhanced acceleration insensitivity due to its non-axial symmetry [58].

To support the cylindrical spacer 4 rectangular cutouts are made in the side of the cylinder. The cutouts provide room to support the structure using 4 spheres made from Viton[10]. These cutouts are kept small to preserve the cylindrical symmetry while keeping enough room to position the Viton spheres at the optimal support points. By optimizing the positioning of the support points, it is possible to significantly reduce the sensitivity of the cavity to accelerations for all 3 dimensions. To find the optimal support positions which minimize vibration sensitivity, an analysis using a finite-element method (FEM) is employed.

3.3.1 Finite-element analysis

To investigate the structural response of the cavity to accelerations for differing geometries and support positioning, a structural model of the cavity is required. A finite-element model is made in COMSOL Multiphysics[11].

Since the cavity is exposed to vibrations from all directions with different sources such as atmospheric pressure fluctuations, oceanic waves and human activity like street traffic [59]. The range of frequencies of acceleration that contribute to frequency noise is typically below 10 Hz, while the first structural resonances of the cavity will be in the ~kHz range [13]. For a small acceleration $\vec{a}$, causing a small force $F = m \cdot a$, the cavity deforms linearly with ΔD, through Hooke's law given by

$$\Delta D = k \cdot a, \tag{62}$$

where k is a proportionality factor. For this reason, the model makes use of the static-strain

[10] Viton ® is a registered brand of vacuum-compatible fluoroelastomer.

[11] COMSOL Multiphysics Reference Manual, version 6.1, COMSOL Inc., www.comsol.com

response of the cavity to external vibrations. The static response of the cavity is studied under an applied acceleration for all dimensions. For acceleration in one dimension, the cavity will displace. The field that describes the displacement $d(x,y,z)$ as a function of positional coordinates (x,y,z) is given by

$$d(x,y,z) \equiv \begin{pmatrix} u \\ v \\ w \end{pmatrix}, \tag{63}$$

where u,v,w are the longitudinal, transverse and vertical displacement respectively. The total length change of the cavity ΔL is then given by the difference in opposite longitudinal displacement u of the two cavity mirrors $M_{1/2}$ given by

$$\Delta L \equiv u_{M_1} - u_{M_2}, \tag{64}$$

where $\Delta L > 0$ corresponds to the cavity length expanding and $\Delta L < 0$ the cavity length contracting. Note that an opposite sign of u at the mirrors is expected for symmetric expansion or contraction of the cavity length, in this case, the length change will be given by $\Delta L = 2u_{M_1}$. An example simulation, indicating the longitudinal displacement of the cavity under vertical acceleration is shown in figure 15.

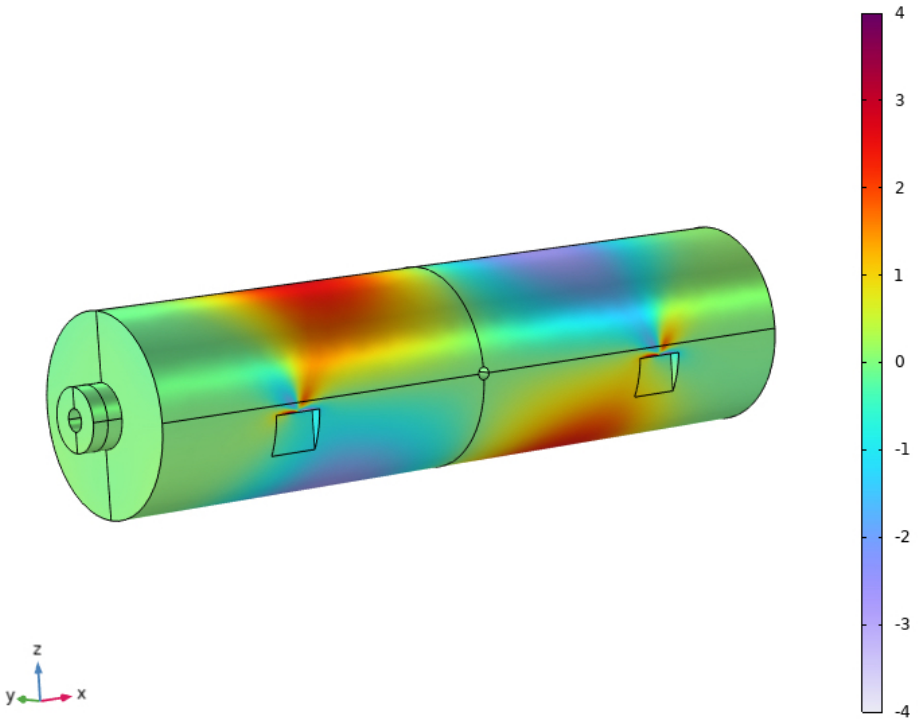
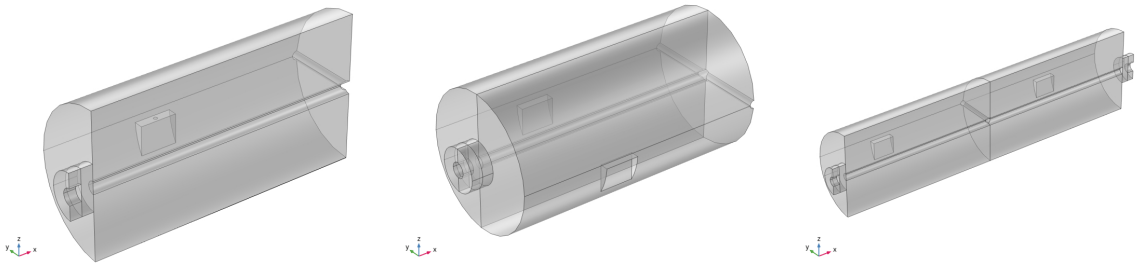


Figure 15: Longitudinal displacement under 1 g of vertical acceleration in nm for $dx = 61.35$ mm and $dz = 3.75$ mm. The color bar shows longitudinal displacement in nm.

To determine a cavity geometry that is insensitive to vibrations, a constant acceleration is applied in all of the three dimensions (x: longitudinal, y: transverse, z: vertical). The symmetry in the cavity geometry can be exploited to reduce the required computation time by only simulating the displacement field for a portion of the cavity. Consider the evaluation of estimating the effects of vertical acceleration, in this case only a quarter of the cavity needs to be simulated with *symmetry*[12] conditions applied to the middle yz and xz plane. The symmetry conditions constrain the geometry against movement normal to the surfaces defined by the symmetry planes, resulting in symmetric displacement solutions. For both transverse and longitudinal accelerations the model only needs to consider half the cavity geometry, with yz and xz as middle symmetry planes respectively. Besides the symmetry conditions, *fixed constraints*[12] are also introduced. For example, the circular supporting positions of the cavity are given a *prescribed displacement*[12] of zero in the vertical direction. In figure 16 a 3D view of the cavity geometries for accelerations applied in the three different dimensions is depicted.



(a) Vertical acceleration. (b) Transverse acceleration. (c) Longitudinal acceleration.

Figure 16: Partial cavity geometries to reduce computational cost by using symmetry conditions, imposing no movement normal to surfaces defined by symmetry planes. The symmetry planes are given for vertical acceleration (a) by the middle xz- and yz-planes, for transverse acceleration (b) by the middle yz-plane and for longitudinal acceleration (c) by the middle xz-plane.

The displacement and tilt of the mirror surfaces under acceleration are determined by defining two *cut lines*[12] along the mirror surfaces, which give the displacement along the optical axis as a function of the mirror coordinates. The defined cut lines are shown in figure 17, which depicts a wireframe rendering of a quarter cavity geometry with relevant geometrical parameters.

[12]These expressions refer to conditions that can be applied in the Solid Mechanics package of COMSOL Multiphysics.

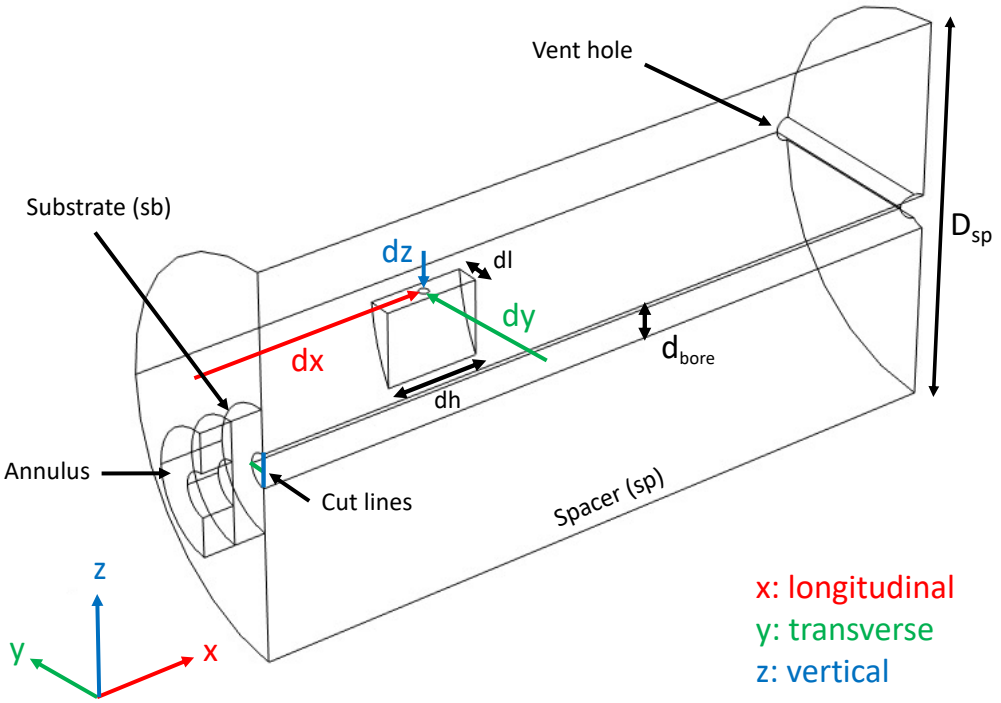


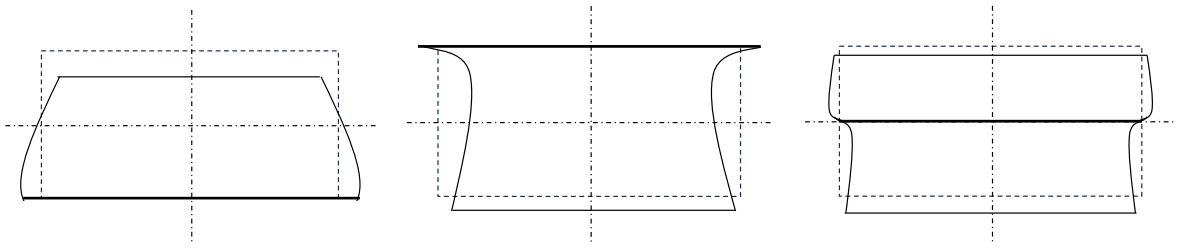
Figure 17: Wireframe representation of a quarter cavity geometry used for simulation under vertical acceleration. The relevant parameters are highlighted, where the dx, dy and dz denote the center of the support position with respect to the spacer face, xz-plane and xy-plane respectively[13].

Now, with the ability to simulate the mirror displacement under acceleration, we still lack insight into how the cavity length changes. The structural behaviour of the cavity length under acceleration can be explained with a combination of the *Poisson effect* and *mirror tilt*.

3.3.2 Poisson effect & mirror tilt

While the cavity structure is experiencing an external force or equivalently acceleration, the optical path length can change due to the Poisson effect and mirror tilt. The Poisson effect is the phenomenon that a material expands or contracts in the dimensions orthogonal to the direction of an applied force. The material parameter that describes the ratio of transverse expansion to expansion in the dimension of the applied force, is called the material's Poisson ratio σ. Both ultra-low-expansion (ULE) glass and fused silica (FS) have a Poisson ratio of $\sigma = 0.17$. In figure 18 the cavity length change due to the Poisson effect is depicted.

It is important to note that the effective length change along the optical axis depends on the

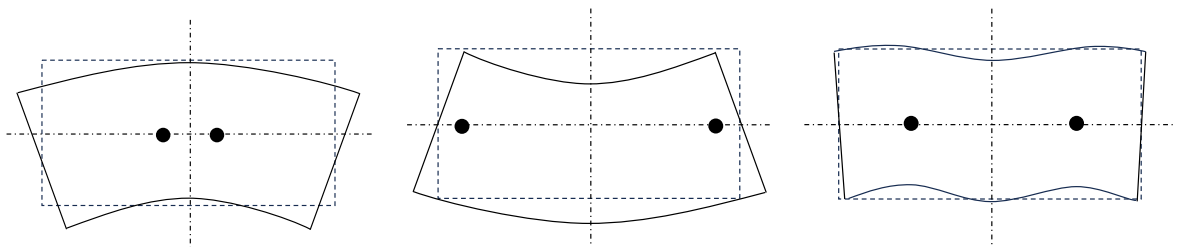


(a) (b) (c)

Figure 18: Schematic overview of the cavity length change due to the Poisson effect under applied vertical acceleration. (a) supported from the bottom. (b) supported from the top. (c) supported in the middle plane.

vertical support plane position; under vertical acceleration, while supported from the bottom the cavity expands, while if it's supported from the top, the cavity contracts. When the cavity is supported somewhere in between these two extremes, it will expand above the supporting plane and contract below it. This means that there will be a vertical support position z for which the contraction and expansion cancel along the optical (x) axis. For simulating the cavity length change the vertical support plane at which the four cutouts will be made, is defined with the dz parameter which gives the position from the middle xy-plane of the cavity as depicted in figure 17.

In addition to the direct expansion or contraction of the cavity due to the Poisson effect, there is also a second-order effect, namely, mirror tilt. When the cavity is subject to an external force, it will bend around the supporting points. Since the mirrors are attached to the ends of the spacer, this bend will result in a tilt of the mirrors and thus a change in the optical path length, as is depicted in figure 19.



(a) (b) (c)

Figure 19: Schematic overview of the cavity length change due to mirror tilt under applied vertical acceleration. (a) supported close to the center. (b) supported close to the spacer ends. (c) supported at the Airy points.

[13]The parameterization convention is adopted from [13].

Clearly, the bending of the cavity spacer is dependent on the longitudinal support positioning. Comparing the two extremes; if the cavity is supported at the outer edges the mirrors will bend inwards and if it is supported at the center, they tilt outwards. This will change the optical path length depending on the beam alignment to the center of the mirror. Again, somewhere in between these two extremes, there exists a longitudinal support position where the optical path length change caused by mirror tilt, cancels out. The support positions at which there is no length change, are called the *Airy points*. This tilt-induced length change is incorporated into the model by the longitudinal support parameter dx, which gives the distance from the center of the support position to the end face of the spacer.

3.3.3 Misalignment Analysis

The induced length change from mirror tilt can be derived from a geometrical analysis for a linear cavity. The optical axis is defined by the line that passes through both centers of curvature C_1 and C_2 of mirrors M_1 and M_2 respectively. Let θ_1 and θ_2 be the small angular rotations of either mirror, which in turn causes the beam centers to shift by Δz_1 and Δz_2 with respect to the mirror centers as is shown in figure 20. This causes an angular displacement $\Delta\theta$ of the optical axis given by

$$\Delta\theta \equiv \frac{\Delta z_2 - \Delta z_1}{L} = \frac{(1-g_2)\cdot\theta_1 - (1-g_1)\cdot\theta_2}{1-g_1g_2}, \tag{65}$$

where we see that the system gets more sensitive to angular misalignment for longer cavities, since $\Delta\theta$ scales with $\propto 1/L$ [60]. The displacements Δz_1 and Δz_2 are given by

$$\Delta z_1 = \frac{g_2}{1-g_1g_2}\cdot L\theta_1 + \frac{1}{1-g_1g_2}\cdot L\theta_2, \tag{66}$$

$$\Delta z_1 = \frac{1}{1-g_1g_2}\cdot L\theta_1 + \frac{g_1}{1-g_1g_2}\cdot L\theta_2, \tag{67}$$

where we can note that the sensitivity to angular misalignment goes to infinity as $g_1g_2 \to 1$. In other words, as the resonator approaches the stability criterion limit, the system gets more and more sensitive to angular misalignment [61].

The optical axis shift leads to a new cavity length given by

$$L_{tilt} \equiv L + \Delta L_{tilt} = \frac{\Delta z_2 - \Delta z_1}{\sin(\Delta\theta)}, \tag{68}$$

where we can do series expansion for ΔL_{tilt} around $\theta_1 = \theta_2 = \theta \to 0$. Expansion to second order for θ around $\theta \to 0$ gives[14]

$$\Delta L_{tilt} \approx \frac{L}{6}\frac{(g_2-g_1)^2}{(1-g)^2}\theta^2, \tag{69}$$

[14]Note that the expression for ΔL_{tilt} by Álvarez differs by a factor 3 [13].

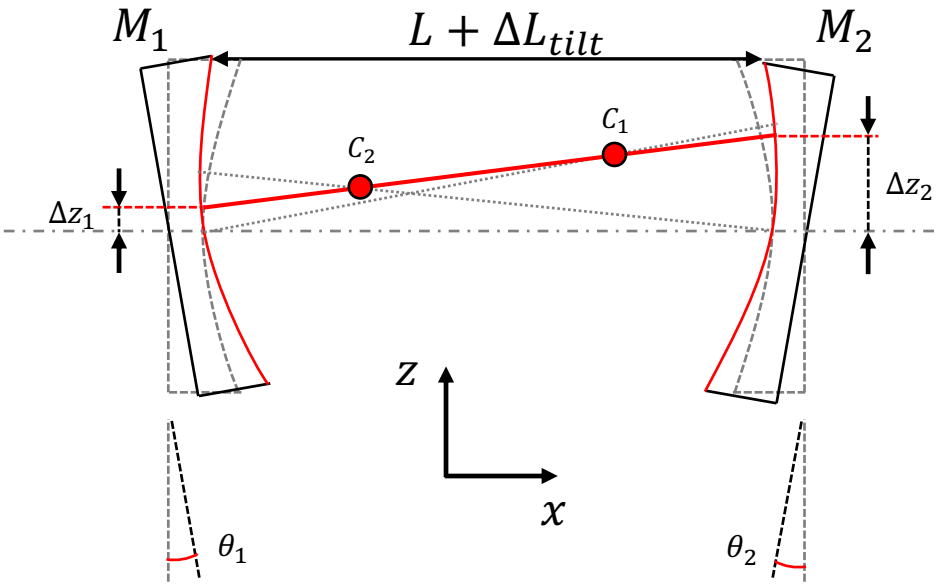


Figure 20: Schematic overview of mirror misalignment and optical axis displacement for a stable two-mirror cavity. The mirror tilts θ_1 and θ_2 induce a shift of the optical axis, which leads to a change in cavity length ΔL_{tilt}.

where the tilt induced length change scales with $\Delta L_{tilt} \propto \theta^2$. Because the mirror tilt has a second-order effect on the cavity length change, for typical small mirror tilts this can be neglected [13; 56]. But when a mirror is misaligned with the center from the spacer end face by Δr, this will cause a first order length change of $\Delta L_{tilt} \sim \theta \cdot \Delta r$. This is an effect that cannot be neglected and needs to be taken into account. The first-order length change under applied accelerations can be modelled while taking into account possible misalignment of the optical mode on the mirrors that is caused by an offset of the mirrors from the center of the spacer end faces.

3.3.4 Modelling cavity length change

Now with the understanding of the sources in our system that change the optical path length under acceleration, we can try to model their contribution. Namely, we can construct a model that quantizes the sensitivity of our system to acceleration-induced length changes. The first-order length change is given by

$$\frac{\Delta L}{L} = \frac{\Delta L_{Poisson}}{L} + \frac{\Delta L_{tilt}}{L} \equiv \mathscr{P} + \mathscr{T}, \tag{70}$$

where $\mathscr{P}$ and $\mathscr{T}$ refer to the length change contributions under small acceleration $\vec{a}$ due to the Poisson effect and mirror tilt respectively. One should note that in reality these two effects are not completely decoupled; the Poisson effect can also give a small tilt to the mirrors. This is not

a real concern since the FEM simulations cannot distinguish tilt induced by the Poisson effect and bending-induced tilt. The Poisson contribution $\mathscr{P}$ is modelled as

$$\mathscr{P} = a_x k_x + a_y k_y + a_z k_z, \tag{71}$$

where $a_{x,y,z}$ corresponds to the dimensional components of the applied acceleration vector $\vec{a}$ and $k_{x,y,z}$ refers to the acceleration sensitivity parameter for each dimension with units of (g^{-1}). The tilt contributions $\mathscr{T}$ is given by

$$\mathscr{T} = a_x \kappa_x \Delta r_z + a_y \kappa_y \Delta r_y + a_z \kappa_z \Delta r_z, \tag{72}$$

where $\kappa_{x,y,z}$ are the tilt sensitivity parameters for each dimension with units of (g^{-1} m^{-1}) and $\Delta r_{y,z}$ are the transverse and vertical offsets of the mirror from the center of the spacer end face. For perfectly centered mirrors $\Delta r_{y,z} = 0$, the first order length change due to mirror tilt will completely disappear.

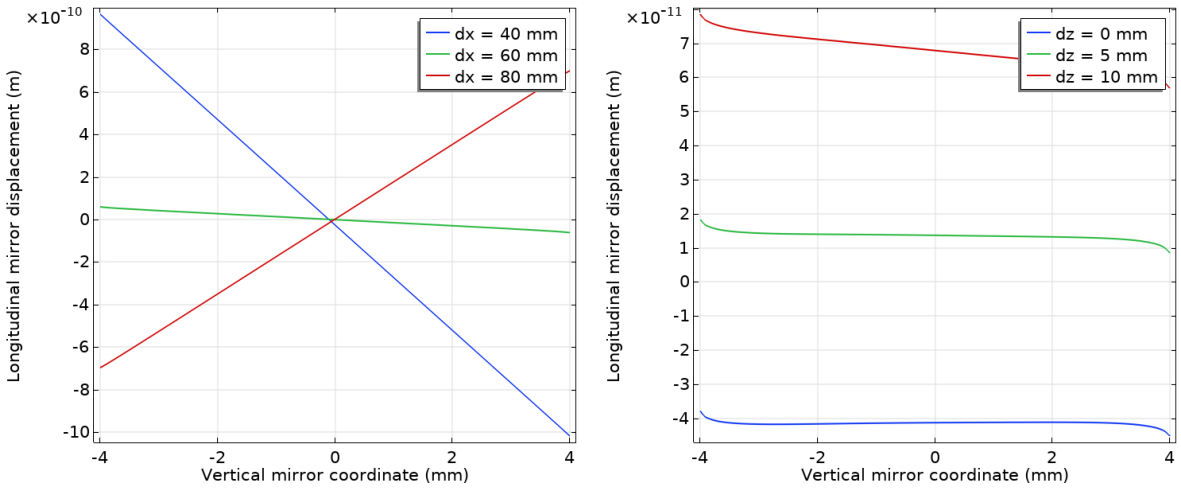
In section 3.3.2 we have seen that change in the vertical position of the supporting plane causes the cavity length to change via the Poisson effect and a change of the longitudinal support positions changes the cavity length because of mirror tilt. We parameterize the positions of the support points with dx and dz, the longitudinal and vertical support positions respectively as shown in figure 17. By changing the support position parameters dx and dz we can simulate the effective length change ΔL, separately for accelerations from each dimension and find a combination (dx, dz) where the length change due to Poisson effect and mirror tilt is compensated. If we choose our support positioning parameters (dx, dz) such that we are indeed in the region where $\Delta L \approx 0$, we are still interested in what happens if in practice we are slightly off in our support positions due to limited machining tolerances, machining errors or human error. This sensitivity to deviations from the ideal support positions (dx, dz) can be investigated by looking at the gradients of the acceleration and tilt sensitivity parameters k and κ with respect to the support position parameter. To give an example, the vertical acceleration sensitivity k_z is dependent on the vertical support position parameter dz due to the Poisson effect, thus the slope of k_z as a function of dz, or equivalently, the gradient $\frac{\partial k_z}{\partial dz}$, gives the sensitivity to dz deviations. The units of the acceleration sensitivity gradient are ($g^{-1}m^{-1}$) and for the tilt sensitivity gradient, the units are ($g^{-1}m^{-2}$). For the optimized support positions the resulting cavity length change needs to be close to zero, while the acceleration and tilt sensitivity gradients are kept to a minimum at the same time.

For a cavity that aims to achieve a thermal noise floor of $\sigma_y \sim 10^{-16}$ with typical environmental vibrations in the lab below 10^{-6} g, the resulting acceleration sensitivity should be no more than 10^{-10} g^{-1}.

3.4 Optimization of support positions

To find the optimal support positions for placing the four cutouts in the spacer, the support positional parameters dx and dz are systematically varied and the following cavity length deformation is studied. The geometric model of the cavity consists of a combination of parameters that are fixed, like the cavity length, and parameters that will be iteratively optimized during the simulations, such as the dimensions and position of the cutouts, etc.

First, let's verify the support point-dependent mirror displacement by varying the dx and dz parameters independently and plotting the mirror displacement, the resulting behaviour is shown in figure 21. The mirror displacement follows the expected behaviour in which the longitudinal support position dx is able to compensate for mirror tilt, while the vertical support position dz can compensate the Poisson effect-induced displacement as mentioned in section 3.3.2.



(a) dx compensates mirror tilt

(b) dz compensates Poisson effect

Figure 21: Longitudinal mirror displacement along vertical cutline under vertical acceleration of 1 g. Figure (a) shows the influence of the longitudinal support position parameter dx on mirror tilt with $dz = 3.75$ mm. Figure (b) shows the influence of the vertical support position parameter dz on mirror displacement induced by the Poisson effect with $dx = 61.35$ mm.

To get a more comprehensive understanding of the support positional dependence of the cavity length, a parameter sweep of the (dx, dz) space has been done and is shown in figure 22. The parameter sweep shows that there exists a region for which the deformation of the cavity results in a length change equal to zero $\Delta L = 0$ for centered mirrors. Furthermore, the cavity length change can be compensated fully by an appropriate choice of dz; for any choice of dx it is possible to achieve $\Delta L = 0$ by adjusting dz. However, it is important to note that the reverse

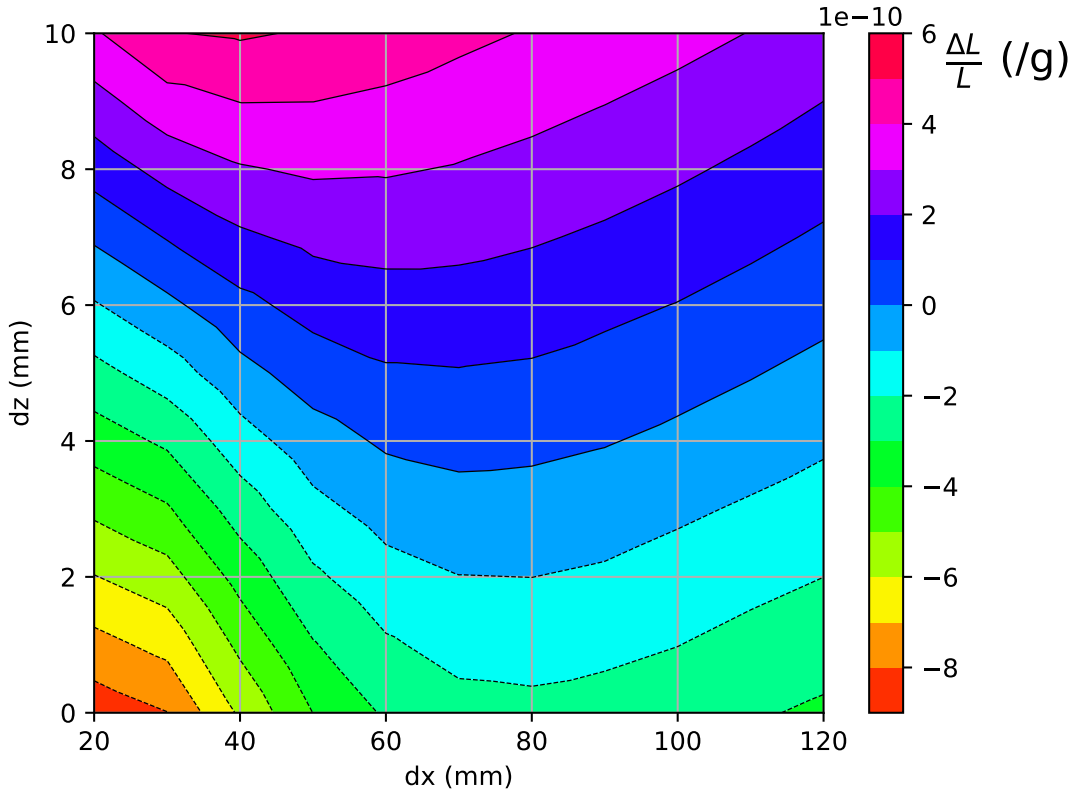


Figure 22: 2D parameter sweep of (dx, dz)-space. Colours indicate relative cavity length change $\frac{\Delta L}{L}$ for centered mirrors.

is not necessarily true; if dz is chosen poorly, it will be impossible to get to the acceleration insensitive regime of $\Delta L = 0$ by adjusting dx.

Since there is a zero-crossing for ΔL, it should be possible to get arbitrarily close to $\Delta L = 0$ for a precise choice of the support parameters dx and dz. Unfortunately, in practice, we cannot control dx and dz to desired precision, therefore, we need to account for slight deviations from the ideal support positions. Moreover, if the cavity mirrors are not perfectly aligned to the center of the spacer face we get additional length change induced by mirror tilt, as discussed in section 3.3.3. For a given dz it can be the case that we cannot compensate fully by adjusting dx. This is a cause for concern especially because in the cavity design dz is a fixed parameter after the cutout has been machined from the ULE spacer, while the dx parameter can be adjusted slightly by repositioning the Viton ball in the cutout. This can be solved preemptively by choosing dz such that it falls in a range that guarantees that there exists a $\Delta L = 0$ zero-crossing for the allowed adjustable range of dx.

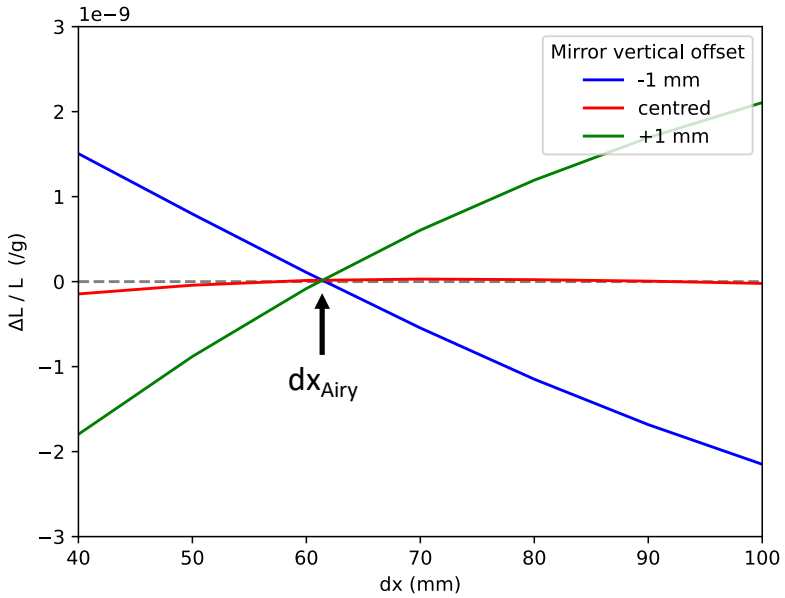


Figure 23: Relative length change $\frac{\Delta L}{L}$ under vertical acceleration of 1 g as a function of longitudinal support position dx (fixed $dz = 4$ mm) for different vertical mirror offset Δr_z from the center of the spacer face. At $dx = dx_{Airy}$ the tilt-induced length change is compensated.

To visualize the effect of mirror offset from the center of the spacer face we can compare the relative length change with centered and misaligned mirrors. In figure 23 the additional length change due to vertical mirror offset Δr_z is shown under vertical acceleration of 1 g. It can be seen that for a certain dx value the relative length change ΔL goes to zero, even for misaligned mirrors. The longitudinal support point where the cavity becomes insensitive to mirror tilt is denoted with dx_{Airy}.

To find the optimal longitudinal support position dx_{Airy} we need to find the value of dx which minimizes the mirror tilt angle. This is done iteratively by plotting the longitudinal mirror displacement with fixed dz for a range of dx and then choosing the dx value for which the mirror tilt is minimal. Repeating the simulation for a smaller dx range around the previous optimal dx point helps to find the most suitable value. Once the mirror tilt is minimized for a fixed dz we need to adjust dz to minimize the absolute length change ΔL. After adjusting dz we need to re-optimize our dx parameter because the two parameters dx and dz are not perfectly decoupled; adjusting dz can induce a tiny amount of mirror tilt. This process is repeated until no further improvement can be obtained within the meshing precision of the simulation, this will be discussed in more detail in section 3.4.7.

The resulting vertical acceleration sensitivity gradient $\frac{\partial k_z}{\partial dz}$, introduced in section 3.3.4, is

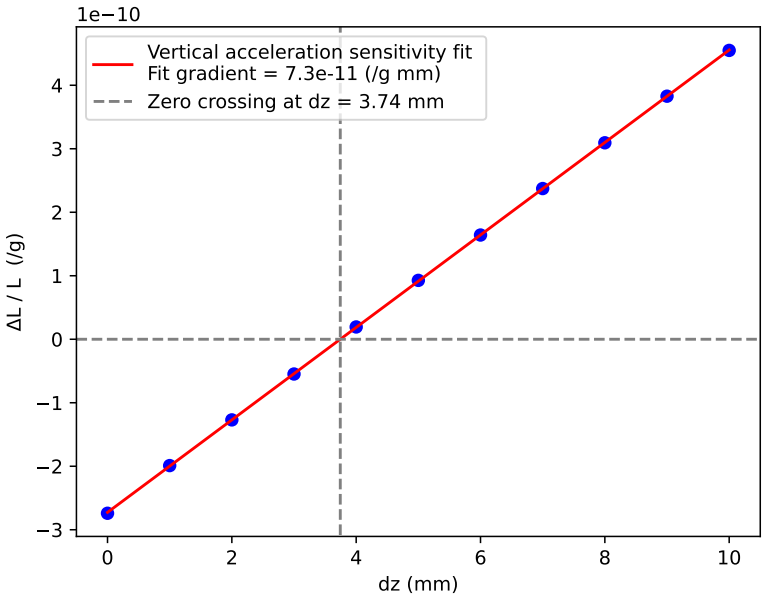


Figure 24: Relative longitudinal length change under vertical acceleration of 1 g versus vertical support position dz. The vertical acceleration sensitivity gradient is determined by a linear fit at $\frac{\partial k_z}{\partial dz} = 7.3 \cdot 10^{-11} \mathrm{g}^{-1} \mathrm{mm}^{-1}$.

calculated by simulating the relative length change $\frac{\Delta L}{L}$ as a function of the vertical support position dz and doing a linear fit to obtain the gradient of the fit curve which corresponds to $\frac{\partial k_z}{\partial dz}$. The linear fit is shown in figure 24 and gives a vertical acceleration sensitivity of $\frac{\partial k_z}{\partial dz} = 7.3 \cdot 10^{-11}\ \mathrm{g}^{-1}\ \mathrm{mm}^{-1}$.

To calculate the vertical tilt sensitivity gradient $\frac{\partial \kappa_z}{\partial dx}$ under vertical acceleration, we first need to calculate the resulting mirror tilt slope for each individual dx value by doing a linear fit to the mirror displacement versus the vertical mirror coordinate. Another consecutive linear fit obtains the gradient of mirror tilt as a function of dx. The linear fit curve to obtain the vertical tilt sensitivity gradient is shown in figure 25. The resulting gradient is given by $\frac{\partial \kappa_z}{\partial dx} = 7.0 \cdot 10^{-11} \mathrm{g}^{-1} \mathrm{mm}^{-2}$.

Sadly, the Airy point is not exactly the same for accelerations applied from different directions. So if we fix dx to dx_{Airy}, calculated for vertical accelerations, we cannot compensate the remaining length change induced by acceleration from the longitudinal and transverse direction.

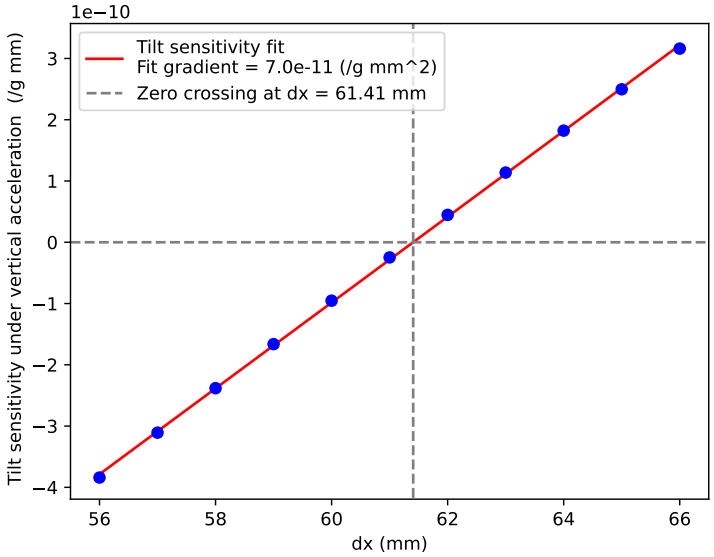


Figure 25: Vertical mirror tilt sensitivity under vertical acceleration of 1 g versus longitudinal support position dx. The vertical tilt sensitivity gradient is determined by a linear fit at $\frac{\partial \kappa_z}{\partial dx} = 7.0 \cdot 10^{-11} g^{-1} \mathrm{mm}^{-2}$.

3.4.1 Transverse acceleration

To study the cavity deformation under transverse acceleration, the modelled cavity geometry now consists of half the cavity geometry, due to symmetry conditions as shown in figure 16b. For transverse acceleration an additional *prescribed displacement* condition needs to be added, namely the support points are now also prohibited to move transversely in addition to the vertical direction. Under transverse acceleration the relative length change is zero for centered mirrors, as depicted in figure 26. These results confirm that the transverse acceleration sensitivity is negligible $k_y \approx 0$ and the remaining length change is induced by mirror tilt $\kappa_y \Delta r_y$. Note that the Airy point $dx_{Airy,y}$ for transverse acceleration differs from the Airy point for vertical acceleration $dx_{Airy,z}$. The difference $|dx_{Airy,z} - dx_{Airy,y}|$ will unavoidably result in a residual tilt sensitivity κ_y if dx is chosen at the Airy point for vertical acceleration.

Calculation of the position of the Airy point under transverse acceleration, is done in the same way as for vertical acceleration. The tilt sensitivity gradient $\frac{\partial \kappa_y}{\partial dx}$ is determined by doing a linear fit of the mirror tilt slopes for each simulated dx value. The resulting transverse tilt sensitivity fit is shown in figure 27 and has a gradient of $\frac{\partial \kappa_y}{\partial dx} = 7.4 \cdot 10^{-11} g^{-1} \mathrm{mm}^{-2}$. The zero-crossing that corresponds to the Airy point occurs at $dx = 64.21$ mm, which is shifted by 2.86 mm compared to the Airy point for vertical acceleration. This discrepancy results in a residual tilt sensitivity of $\kappa_y = 2.1 \cdot 10^{-10}$ $\mathrm{g}^{-1} \mathrm{mm}^{-1}$.

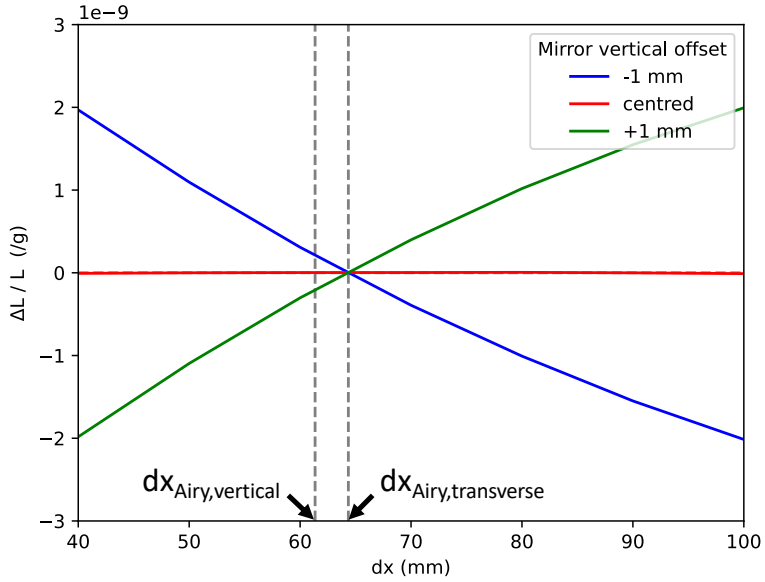


Figure 26: Relative length change $\frac{\Delta L}{L}$ under transverse acceleration of 1 g as a function of longitudinal support position dx (fixed $dz = 4$ mm) for different transverse mirror offset Δr_y from the center of the spacer face. The Airy point dx_{Airy} is different for vertical accelerations and transverse accelerations, denoted by the vertical lines.

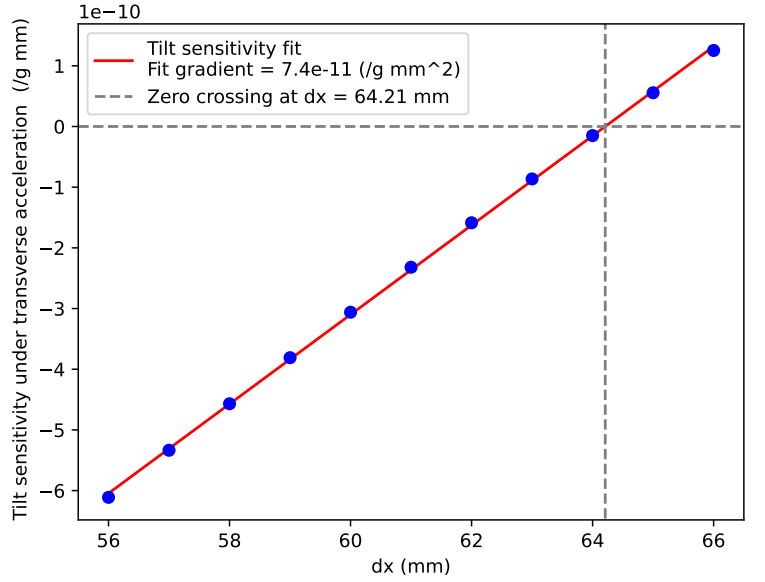


Figure 27: Transverse mirror tilt sensitivity under transverse acceleration of 1 g versus longitudinal support position dx. The transverse tilt sensitivity gradient is determined by a linear fit at $\frac{\partial \kappa_y}{\partial dx} = 7.4 \cdot 10^{-11} g^{-1} \text{mm}^{-2}$.

3.4.2 Longitudinal acceleration

In a similar way we study the relative length change caused by longitudinal acceleration along the optical axis. The simulations consider half of the entire cavity geometry, split by the xz-plane as shown in figure 16c.

The longitudinal tilt sensitivity parameter changes as a function of the vertical support position $\kappa_x(dz)$. The slope of the linear fit of the tilt sensitivity parameter as a function of dz gives the tilt sensitivity gradient $\frac{\partial \kappa_x}{\partial dz} = -8.1 \cdot 10^{-11} g^{-1} \mathrm{mm}^{-2}$, as shown in figure 28. The zero-crossing occurs at $dz = 0.44$ mm, which is offset by 3.31 mm compared with the optimal dz for vertical acceleration. This discrepancy results in a residual tilt sensitivity of $\kappa_x = -2.4 \cdot 10^{-10}$ $\mathrm{g}^{-1}\mathrm{mm}^{-1}$.

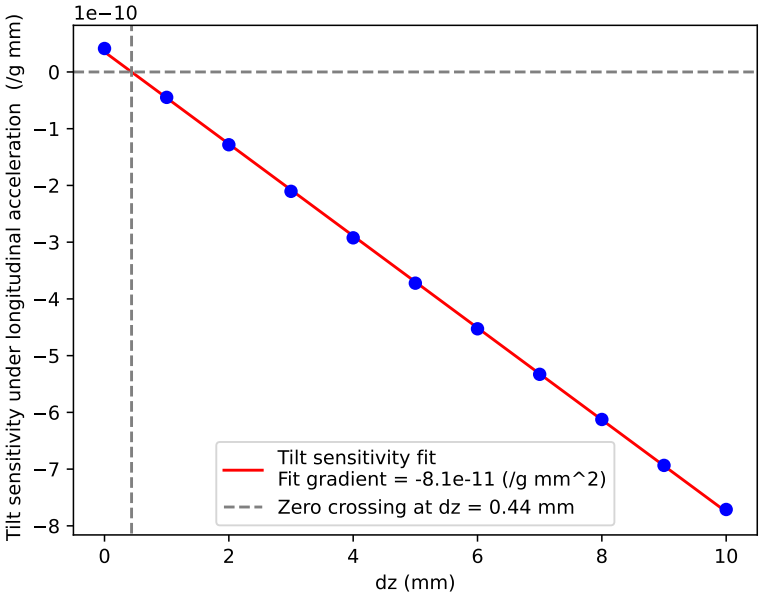


Figure 28: Vertical mirror tilt sensitivity under longitudinal acceleration of 1 g versus vertical support position dz. The vertical tilt sensitivity gradient is determined by a linear fit at $\frac{\partial \kappa_x}{\partial dz} = -8.1 \cdot 10^{-11} g^{-1} \mathrm{mm}^{-2}$.

3.4.3 Spacer geometry optimization

We have found a way to find an acceleration insensitive configuration by optimizing the support positions for a given spacer. So naturally we are interested to find the optimal spacer geometry. To achieve this we want to find how the acceleration and tilt sensitivities change depending on the diameter of the spacer and the depth of the four cutouts.

First, we investigate the influence of spacer diameter on the vertical acceleration and tilt sensitivity gradients. For each value of the spacer diameter the gradient of the vertical acceleration sensitivity $\frac{\partial k_z}{\partial dz}$ is calculated by taking a linear fit of the relative length change $\frac{\Delta L}{L}$ against the vertical support position parameter dz. The vertical tilt sensitivity gradient $\frac{\partial \kappa_z}{\partial dx}$ was determined for each spacer diameter by calculating the slope of mirror tilt. Next, a second linear fit of the mirror tilt slope versus the longitudinal support parameter dx yields the vertical tilt sensitivity gradient.

The resulting vertical acceleration and tilt sensitivity gradients as a function of spacer diameter are shown in figure 29. To be able to compare the sensitivity gradients we need to multiply the tilt sensitivity κ by a value for the mirror offset Δr. Here we choose a slightly pessimistic scenario with a large mirror offset of $\Delta r_z = 1$ mm. Interestingly, the vertical acceleration sensitivity gradient increases with increasing spacer diameter, while the vertical tilt sensitivity decreases. So a smaller diameter spacer is more sensitive to tilt induced length change, but a larger spacer will be more susceptible to length change induced by the Poisson effect. To minimize the total sensitivity gradient we choose a spacer diameter of 8 cm, for which the two contributions are in balance, keeping in mind that the actual tilt contribution can change depending on the mirror offset.

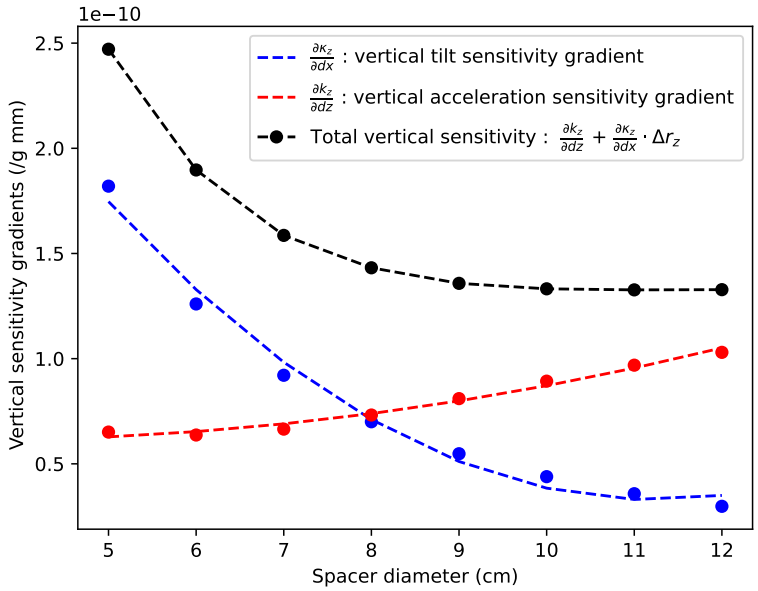


Figure 29: Vertical acceleration and tilt sensitivity gradients for differing spacer diameter. To be able to compare both the acceleration and tilt sensitivity gradients, we have multiplied the later $\frac{\partial \kappa_z}{\partial dx}$ with the vertical mirror offset $\Delta r_z = 1$ mm.

Second, we explore the influence of the depth of the cutouts on the vertical acceleration and tilt sensitivity gradients. In each simulation we alter the value for the cutout depth dl and read out the relative length change for centered mirrors. In addition, we vary dz around its optimal value for every chosen dl and do a linear fit to find the vertical acceleration sensitivity gradient $\frac{\partial k_z}{\partial dz}$. This provides us with the vertical acceleration sensitivity gradient as a function of the cutout depth dl and the result is depicted in figure 30.

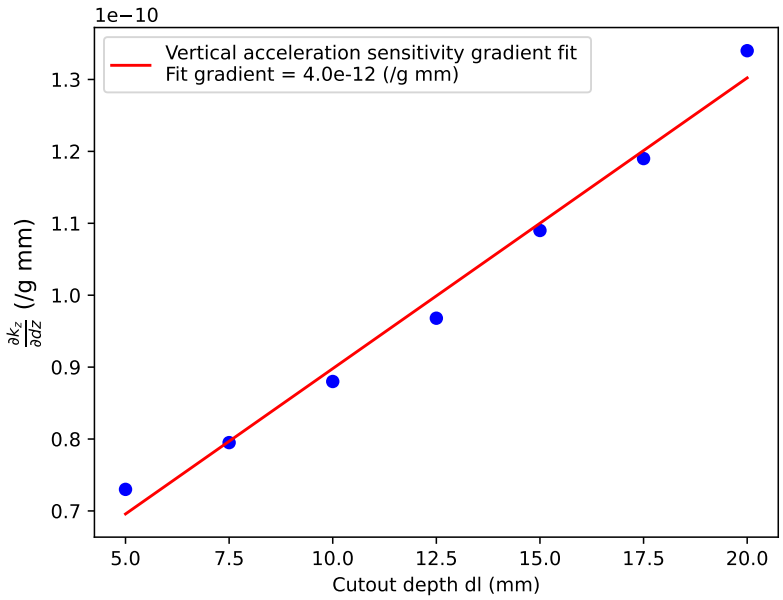


Figure 30: Vertical acceleration sensitivity gradient $\frac{\partial k_z}{\partial dz}$ as a function of cutout depth dl. A cavity with a larger cutout is more susceptible to deviations in dz.

The simulations show that by increasing the depth of the four cutouts, the vertical acceleration sensitivity gradient increases. This corresponds to a larger cavity length change resulting from deviations in dz. For this reason we choose a cutout depth of $dl = 5$ mm, which provides the lowest susceptibility to dz deviations while also being considered the minimal amount of room that is needed to position the cavity in a safe manner on the four Viton balls supports, which have a diameter of ~ 4 mm. The cutout width dh is set to 20 mm, offering room for adjustment of the Viton ball in the longitudinal dimension of the cutout. In the simulations we have assumed a support radius of 1 mm, since the Viton balls are under compression. Because the actual support radius could differ slightly, the support radius dependence of the cavity's mechanical stability is probed.

3.4.4 Support area dependency

The cavity will be supported by Viton balls placed at the calculated support positions. Due to compression by the cavity, the Viton balls (diameter ≈ 4 mm) will have a contacting surface of radius $R_{sup} \approx 1$ mm. Since this is not an exact estimation, we can simulate what would be the effect on the relative length change if the exact supporting radius would differ slightly from 1 mm. Figure 31 shows the relative length change under vertical acceleration as a function of the supporting radius. The gradient around $R_{sup} = 1$ mm is determined by a linear fit at $\frac{\partial k_z}{\partial R_{sup}} \approx 2 \cdot 10^{-12} \mathrm{g}^{-1}\mathrm{mm}^{-1}$. This is sufficiently small to neglect, for a deviation in supporting radius of ± 0.1 mm the resulting acceleration sensitivity would change by $\delta k_z < 10^{-12}$ g^{-1}, far below the maximum tolerable sensitivity range of 10^{-10} g^{-1}.

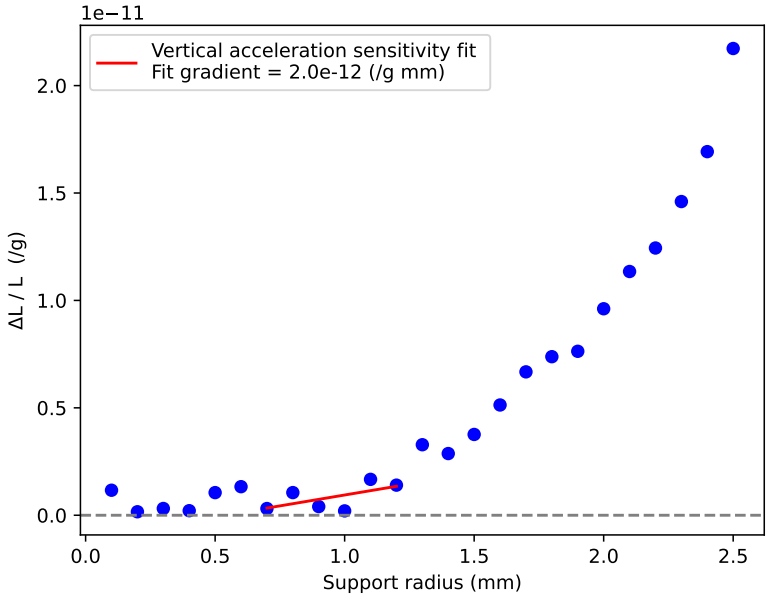


Figure 31: longitudinal length change dependence on support radius, under vertical acceleration of 1 g. The vertical acceleration sensitivity gradient is determined by a linear fit at $\frac{\partial k_z}{\partial R_{sup}} \approx 2 \cdot 10^{-12} \mathrm{g}^{-1}\mathrm{mm}^{-1}$.

The same analysis can be done for the tilt sensitivity. The vertical tilt sensitivity parameter as a function of the supporting radius is shown in figure 32. The resulting fit gradient is $\frac{\partial \kappa_z}{\partial R_{sup}} \approx -6 \cdot 10^{-13} g^{-1}\mathrm{mm}^{-2}$, which is also small enough to neglect.

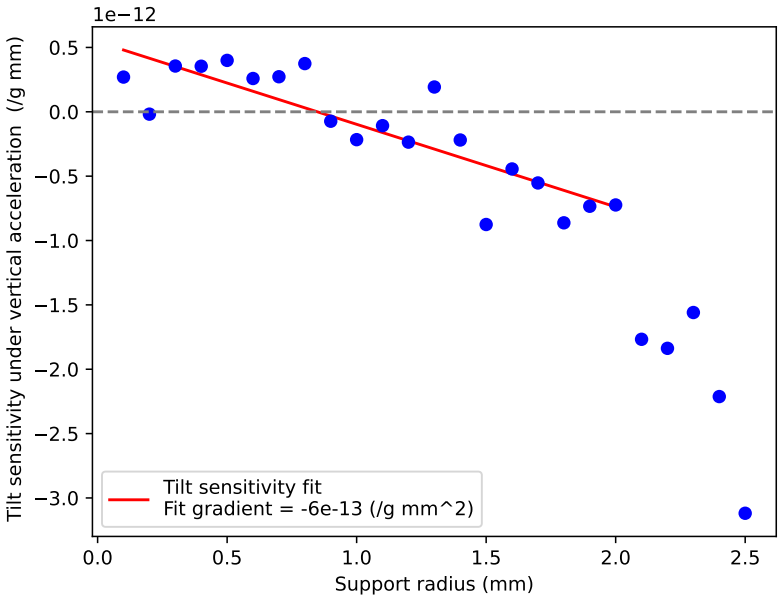


Figure 32: Vertical tilt sensitivity dependence on support radius. The vertical tilt sensitivity gradient is determined by a linear fit at $\frac{\partial \kappa_z}{\partial R_{sup}} \approx -6 \cdot 10^{-13} g^{-1} \mathrm{mm}^{-2}$

3.4.5 Transverse support offset

We have shown that the length change induced by mirror tilt and the Poisson effect can be compensated by the supporting position parameters dx and dz respectively. Yet, we have not considered the influence of transverse (y-) offset of the support points. To make sure that a slight transverse deviation does not affect the sensitivity considerably, a transverse offset of dy was introduced in the simulation. The relative length change under vertical acceleration as a function of transverse offset of the support position dy is shown in figure 33. The linear fit has a gradient of $\frac{\partial k_z}{\partial dy} = -1.8 \cdot 10^{-11} g^{-1} \mathrm{mm}^{-1}$. The tilt sensitivity gradient is determined at $\frac{\partial \kappa_z}{\partial dy} = 5.5 \cdot 10^{-12} g^{-1} \mathrm{mm}^{-2}$, as shown in figure 34.

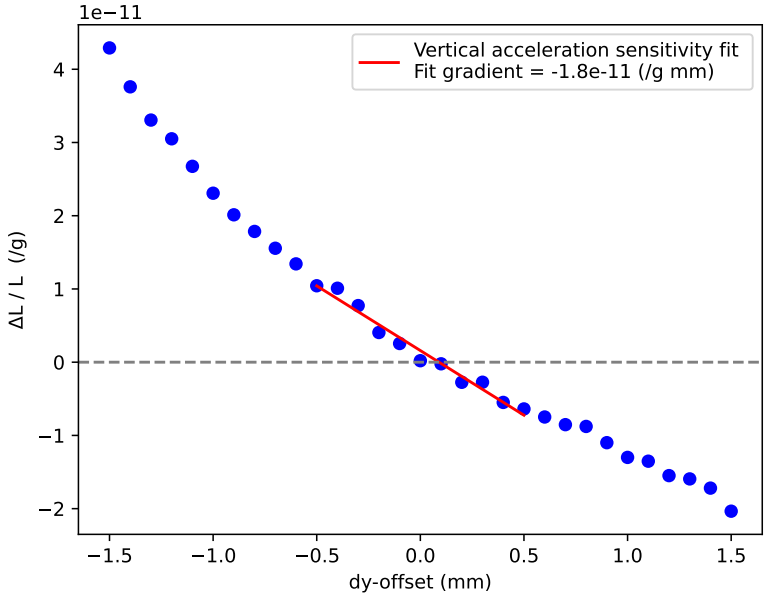


Figure 33: Fractional longitudinal length change under vertical acceleration of 1 g versus offset of the transverse support position dy. The vertical acceleration sensitivity gradient is determined by a linear fit at $\frac{\partial k_z}{\partial dy} = -1.8 \cdot 10^{-11} g^{-1} \mathrm{mm}^{-1}$.

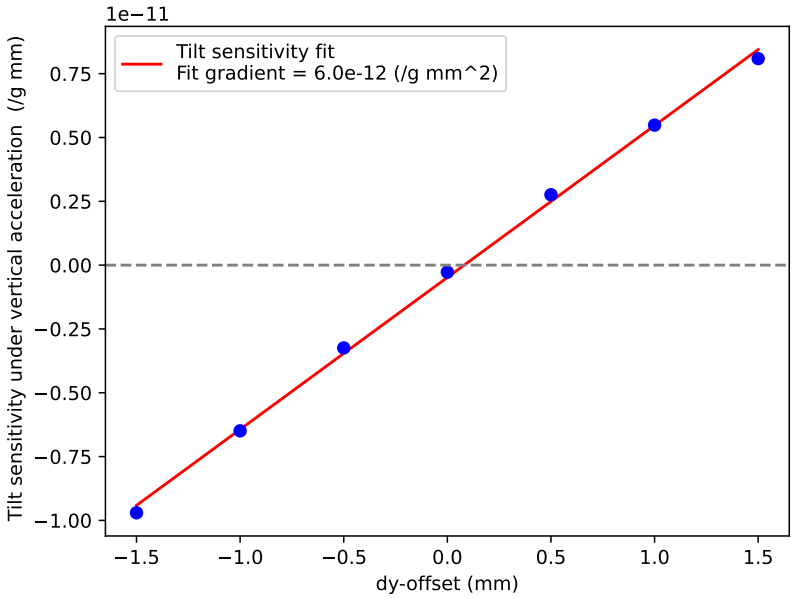


Figure 34: Vertical mirror tilt sensitivity under vertical acceleration of 1 g versus offset of the transverse support position dy. The vertical tilt sensitivity gradient is determined by a linear fit at $\frac{\partial \kappa_z}{\partial dy} = 6.0 \cdot 10^{-12} g^{-1} \mathrm{mm}^{-2}$.

3.4.6 Finalized configuration

The finalized configuration of the support points and cavity geometry consists of a cylindrical cavity spacer with a length of 30 cm, a diameter of 8 cm, with 4 cutouts having dimensions of 5 mm x 20 mm. The relevant geometrical parameters, as well as acceleration and tilt sensitivities and their gradients are listed in table 5. A technical schematic of the cavity is provided in appendix B.

Table 5: Summary of all the relevant parameters and the resulting acceleration and tilt sensitivities and their gradients at the final support positions.

Geometrical parameters	[mm]
L	300
R_{sp}	40
R_{bore}	4
dl	5
dh	20
Optimal support positions	[mm]
dx	61.35
dz	3.75
Residual tilt sensitivities	[g^{-1}]
$\kappa_y \cdot \pm 0.1$ mm	$2.1 \cdot 10^{-11}$
$\kappa_x \cdot \pm 0.1$ mm	$-2.4 \cdot 10^{-11}$
Acceleration sensitivity gradients	[g^{-1} mm^{-1}]
$\frac{\partial k_z}{\partial dz}$	$7.3 \cdot 10^{-11}$
$\frac{\partial k_z}{\partial dy}$	$-1.8 \cdot 10^{-11}$
Tilt sensitivity gradients	[g^{-1} mm^{-2}]
$\frac{\partial \kappa_z}{\partial dx}$	$7.0 \cdot 10^{-11}$
$\frac{\partial \kappa_y}{\partial dx}$	$7.4 \cdot 10^{-11}$
$\frac{\partial \kappa_x}{\partial dz}$	$-8.1 \cdot 10^{-11}$

3.4.7 Limitation of the FEM simulations

The finite element analysis done in COMSOL calculates the displacement for a large number of points in the cavity geometry. The number of points that it considers is determined by the *mesh* size and distribution that is used. COMSOL gives the option to choose a predefined mesh element size, from extremely coarse to extremely fine. For our simulations we increase the

number of elements in critical areas, such as the mirror cutlines and the supporting points, which is shown in figure 35. We can estimate the meshing error of our simulations by systematically increasing the fineness of the mesh from normal to extremely fine, considerably increasing the computation time for each simulation in the process. Using this procedure, the meshing error was estimated to be $\sim 10^{-12}$ g^{-1} which is lower than our tolerance limit [15].

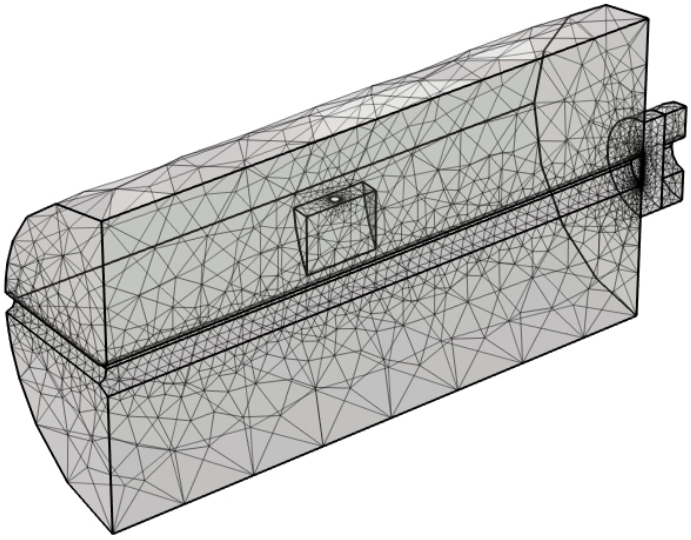


Figure 35: 3D rendering of a quarter cavity geometry with mesh distribution. The depicted mesh has a predefined *Fine* element size with additional *Free Tetrahedral* mesh *distribution* nodes with 25 elements along the mirror cutline and 5 elements along the support points.

3.5 Cavity Mounting

To ensure that the cavity can realize thermal-noise-limited performance its vibration sensitivity needs to be sufficiently small. The mounting of the cavity is crucial to reach the simulated acceleration sensitivities of the cavity. An imbalance in the loading force on the four supporting points spoils the simulated optimized vibration sensitivity. Unfortunately, using four support points makes the supporting plane over-constrained, which actually induces unequal loading of the four support legs [56; 13]. This is especially concerning since in practise slight height imperfections of the supporting legs or machining imperfections of the spacer will cause unbalanced loading.

To combat the loading imbalance an effective three-point mounting strategy can be implemented as shown by Häfner *et al.* [62]. The over-constrained mounting with four support points

[15] The work of Amairi presents a similar estimation of the meshing error [56].

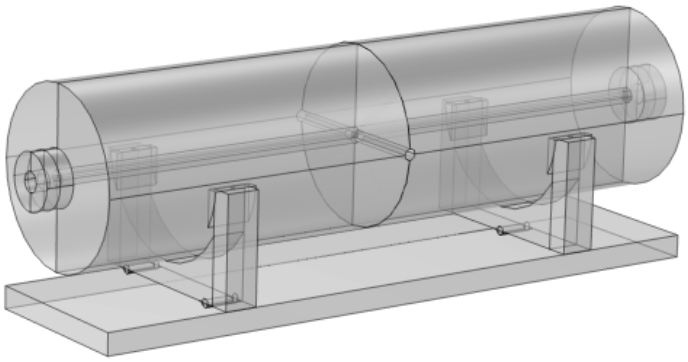


Figure 36: 3D rendering of the effective three-point mounting structure. The ULE spacer rests on four Viton balls resting on two U-shaped ULE supports. The first U-shaped support has two cylinders that contact the ULE baseplate, while the second U-shaped support only has one. This allows the cavity to rotate along the optical axis to automatically balance the load on the support points. This mounting strategy was adopted from the work of Amairi [56].

can be turned into a self-balancing mounting structure, balanced on three points as shown in figure 36. The presented mounting method was adopted from the work of Amairi, where it was implemented for a rectangular ULE cavity [56].

In the three-point mount the ULE cavity spacer rests on four Viton balls which are placed on two U-shaped ULE supports. The first U-shaped support has two cylinders that contact the ULE baseplate, while the second U-shaped support only has one. Because the contact is made by cylinders they allow a degree of freedom for rotation along their long axis. This allows half of the cavity to rotate along the optical axis which automatically balances the load on the support points.

By opting for contact cylinders instead of spheres, we have only allowed for self-balancing along the longitudinal axis. To achieve a fully self-balanced structure, the ULE baseplate contacts the first inner heat shield with three spheres placed such that the center of gravity of the mounted cavity overlaps with the center of mass of the triangle the spheres form. The technical drawings of the cavity mounting structure are given in appendix B.

3.6 Thermal sensitivity

In addition to vibrations, other external environmental perturbations, like temperature and pressure fluctuations can alter the cavity length. The variations in temperature are coupled to the length of the cavity by thermal expansion or contraction of the cavity spacer, mirror substrates and annuli. The property that describes the thermal expansion of a material with a change in temperature T is the coefficient of thermal expansion (CTE) $\alpha(T)$. A certain change in temperature $\Delta T = T_f - T_i$ then produces a fractional length change of

$$\frac{\Delta L}{L} = \int_{T_i}^{T_f} \alpha(T) dT, \tag{73}$$

for a small temperature change, this reduces to

$$\frac{\Delta L}{L} = \alpha(T)\Delta T. \tag{74}$$

The resulting length fluctuations due to temperature fluctuations can thus be reduced by choosing materials with a small CTE. For the cavity spacer, the typical choice is ultra-low-expansion (ULE[16]) glass, since it has a small CTE with a zero-crossing around room temperature, which eliminates the need of a cryogenic system. The CTE of ULE is approximated to second order by

$$\alpha_{ULE}(T) = a(T - T_0) + b(T - T_0)^2, \tag{75}$$

where a and b are the linear and quadratic temperature coefficients which are approximately $2 \cdot 10^{-9}$ K^{-2} and $-1 \cdot 10^{-11}$ K^{-3} respectively for ULE. The zero-crossing temperature is denoted by T_0, this is the temperature at which the CTE crosses zero, where there is no expansion or contraction ideally. The zero-crossing temperature for ULE is specified to be around 20°C [53]. The mirror substrates are made from fused silica (FS), in order to reduce the thermal noise floor of the cavity, as is discussed in section 3.1. Fused silica does have a significantly higher CTE compared to ULE, namely $\alpha_{FS}(T) = 500 \cdot 10^{-9} + 2.2 \cdot 10^{-9}(T - T_0)$ K^{-1}. This causes the effective CTE α_{eff} of the cavity to differ from that of ULE α_{ULE}. Since the CTE of FS is much larger than that of ULE, the mirrors will experience much more thermal expansion compared to the spacer they are optically contacted to. This will result in stress building up in the mirror substrate for a change in temperature. This stress will be partially relieved by deformation of the back side of the mirror, resulting in outward bulging of the mirror since the back is not directly attached to the spacer. For the combined ULE spacer and FS mirrors the effective CTE is given by

$$\alpha_{eff}(T) = \alpha_{ULE}(T) + \delta \frac{d_{sb}}{L} [\alpha_{FS}(T) - \alpha_{ULE}(T)], \tag{76}$$

[16] ULE ® is a registered brand of ultra-low-expansion glass made with TiO_2 doped silica from Corning Inc.

where d_{sb} is the diameter of the mirror substrate, L the spacer length and δ is the coupling coefficient, which assumes a linear stress-strain relation between spacer and mirror and only depends on the geometry and material properties of the cavity [53]. The effective CTE will be larger compared to that of ULE alone since the CTE mismatch ($\alpha_{FS} - \alpha_{ULE}$) is positive and the slope of the CTE is positive as well. This means that the zero-crossing temperature T_0 for the effective system, consisting of the ULE spacer + FS mirrors, will be lowered compared to a cavity made completely of ULE. The thermal expansion can be simulated with COMSOL, the shift in zero-crossing temperature going from ULE to FS mirrors is shown in figure 37.

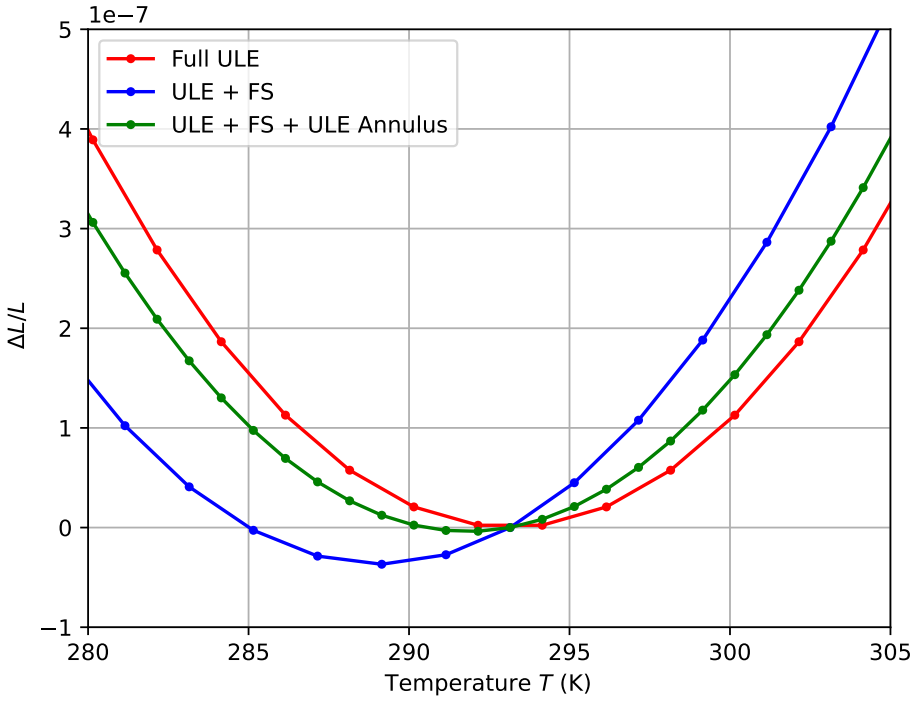
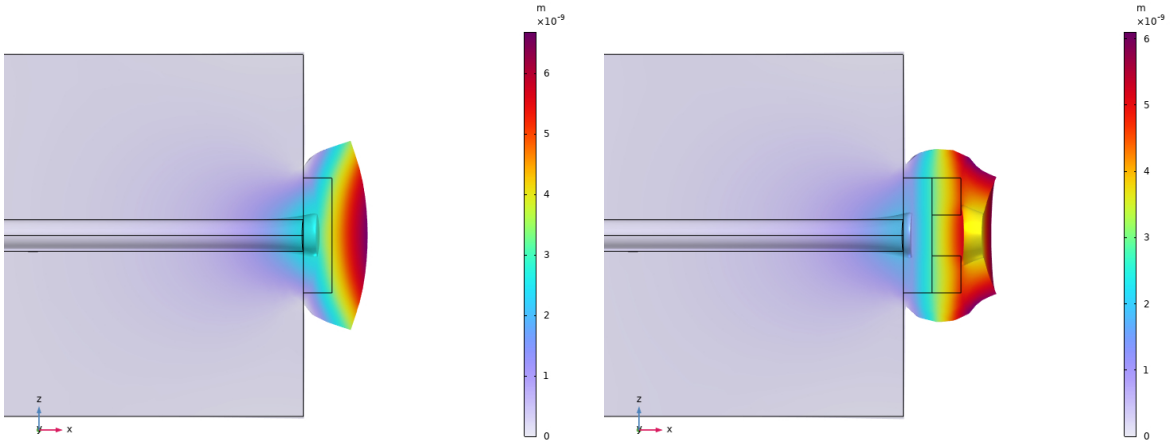


Figure 37: FEM Simulation of the cavity length change $\frac{\Delta L}{L}$ due to thermal expansion for a cavity with an ULE spacer and ULE mirrors (in red), an ULE spacer and FS mirrors (in blue) or an ULE spacer with FS mirrors combined with ULE annuli optically contacted to the back of the mirrors.

By opting for FS over ULE mirror substrates, we lower the thermal noise floor since FS has a lower mechanical loss factor, as discussed in section 3.2.1. From the simulation we can verify that this has the unwanted consequence of shifting the zero-crossing temperature T_0 further from room temperature. To reduce the influence on the effective coefficient of thermal expansion, we can attach ULE *rings* to the back of the FS mirrors.

3.6.1 ULE annulus

To combat the zero-crossing temperature shift Legero *et al.* proposed to attach ULE rings, also referred to as annuli, to the back of the FS mirror substrates [53]. The ULE annuli reduce the effective CTE back to that of the ULE spacer. The deformation of the mirror substrate is largely suppressed by the ULE annulus as depicted in figure 38. The resulting suppression of the zero-crossing temperature shift in comparison to a cavity without ULE annuli is shown in figure 37.



(a) FS mirror substrate

(b) FS mirror substrate + ULE annulus

Figure 38: Thermal expansion due to $\Delta T = 1$ K, either without (a) or with (b) ULE annulus with an inner diameter of $d_{ring} = 9$ mm, attached to the backside of the fused silica mirror substrate.

3.6.2 Heat transfer modelling

Besides choosing materials with low CTE, we can also aim to reduce the thermal fluctuations that the cavity experiences. This is achieved by implementing a cavity housing which is thermally isolated against external temperature changes. Heat transfer under vacuum conditions will predominantly have conductive and radiative contributions. The conductive heat flow $\dot{q}_{con}$ from a system at fixed temperature T_1 towards a system at $T_2(t)$, through a material with thermal conductivity λ, cross-sectional area A and length l, is given by[17]

$$\dot{q}_{con} = \lambda \frac{A}{l}[T_1 - T_2(t)], \tag{77}$$

To reduce the effect of conductive heat transfer we can choose materials with low thermal

[17] Valid for conductive heat transfer through a prismatic or cylindrical object.

conductivity and minimize the contacting surface between connected materials in the cavity housing. The heat transfer due to radiation $\dot{q}_{rad}$ from a surface with area A_1 to a different surface A_2 which have a temperature of T_1 and T_2 respectively, is determined by the law of Stefan-Boltzmann, given by

$$\dot{q}_{rad} = \sigma_{SB}\left(\frac{1}{A_1\epsilon_1} + \frac{1}{A_2\epsilon_2} - \frac{1}{A_1}\right)^{-1} \cdot \left[T_1^4 - T_2(t)^4\right], \tag{78}$$

where $\sigma_{SB} = 5.6703 \cdot 10^{-8}\ \mathrm{Wm^{-2}K^{-4}}$ is the Stefan-Boltzmann constant and $\epsilon_{1/2}$ is the *emissivity* of surface $A_{1/2}$. The emissivity of a surface defines the ratio of the energy radiated from a material's surface compared to that radiated from a black body. A perfect reflector will have $\epsilon = 0$, while a perfect emitter or black-body, has $\epsilon = 1$. So the heat transfer through radiation can be reduced by decreasing the emissivity ϵ of the surfaces of the cavity housing. This can be achieved by polishing the surfaces and using highly reflective surface coatings. For small temperature fluctuations $\Delta T = T_1 - T_2(t) \ll T_1$, the radiative heat transfer can be approximated to first order as

$$\dot{q}_{rad} = 4\sigma_{SB}T_1^3\left(\frac{1}{A_1\epsilon_1} + \frac{1}{A_2\epsilon_2} - \frac{1}{A_1}\right)^{-1} \cdot \Delta T(t). \tag{79}$$

Combining the expressions for the conductive and radiative heat transfer of system (1) at fixed temperature T_1 acting on system (2), the variations of T_2 in time will be given by

$$C_2\frac{\partial T_2(t)}{\partial t} = \dot{q}_{con} + \dot{q}_{rad} \tag{80}$$

$$= \left(\lambda\frac{A}{l} + 4\sigma_{SB}T_1^3\left(\frac{1}{A_1\epsilon_1} + \frac{1}{A_2\epsilon_2} - \frac{1}{A_1}\right)^{-1}\right) \cdot \Delta T(t) \tag{81}$$

$$= \kappa_{12} \cdot \Delta T(t), \tag{82}$$

where $C_2 = M_2 \cdot c_p$ is the thermal capacity of system (2) with M_2 and c_p its mass and specific heat, and κ_{12} gives the total heat flow from system (1) to (2). This differential equation is solved by an exponential with characteristic time constant $\tau_{12} = C_2/\kappa_{12}$. This system will effectively function as a low-pass filter for temperature fluctuations between the two systems. When temperature fluctuations happen on a faster time scale than τ_{12}, the fluctuations are damped with an effective cut-off frequency of $1/\tau_1$. Typically ultrastable cavities make use of several heat shields, such that multiple first-order low-pass filters, with differing time constants are combined in series to strongly attenuate any temperature fluctuations [17; 56; 14].

A cavity that has two inner passive heat shields and an additional outer actively stabilized heat shield is shown in figure 39. The heat shields act as heat capacitance which behaves effectively as a low-pass filter for short-term temperature fluctuations. The time-dependent thermal behaviour of the heat shields and cavity can be determined by a set of coupled differential equations that take the conductive and radiative heat transfer mechanisms into account.

For the active heat shield at a fixed temperature T_3, the passive heat shields at temperature T_2 and T_1 respectively and the cavity at T_c, the system of coupled differential equations are given by

$$C_c \frac{\partial T_c(t)}{\partial t} = \kappa_{1c}[T_1(t) - T_c(t)], \tag{83}$$

$$C_1 \frac{\partial T_1(t)}{\partial t} = \kappa_{21}[T_2(t) - T_1(t)] - \kappa_{1c}[T_1(t) - T_c(t)], \tag{84}$$

$$C_2 \frac{\partial T_2(t)}{\partial t} = \kappa_{32}[T_3 \quad - T_2(t)] - \kappa_{21}[T_2(t) - T_1(t)]. \tag{85}$$

The general solution for the temperature of the cavity $T_c(t)$ is given by

$$T_c(t) = A \cdot e^{-t/\tau_a} + B \cdot e^{-t/\tau_b} + C \cdot e^{-t/\tau_c}. \tag{86}$$

The time-evolution of the temperature for a small change in the temperature of the active heat shield ΔT and an initial cavity temperature offset $T_c(0)$ can given by

$$T_c(t) = T_c(0) + \Delta T \left(1 - \frac{\tau_a^2}{(\tau_a - \tau_b)(\tau_a - \tau_c)} \cdot e^{-t/\tau_a} + \frac{\tau_b^2}{(\tau_a - \tau_b)(\tau_b - \tau_c)} \cdot e^{-t/\tau_b} - \frac{\tau_c^2}{(\tau_a - \tau_c)(\tau_b - \tau_c)} \cdot e^{-t/\tau_c} \right). \tag{87}$$

This gives the temperature response normalized to the absolute temperature change ΔT.

Now with the understanding of the heat transfer process, we can design a cavity enclosure and simulate its behaviour to temperature changes.

3.6.3 Heat shields design

To minimize the radiative heat transfer between consecutive heat shields, the surface emissivity should be as low as possible. Further, to ensure that the temperature distribution along the cavity is as homogeneous as possible, the heat shields themselves are made from highly conductive materials such as aluminium $\lambda_{Alu} = 235$ W m^{-1} K^{-1}. The aluminium plates that make up the heat shields are polished to reduce their surface emissivity, typically to $\epsilon \approx 0.03$. The masses of the three heat shields made from 10 mm thick aluminium plates are $M_3 \approx 14$ kg, $M_2 \approx 10$ kg and $M_1 \approx 7$ kg from outer to innermost heat shield. The specific heat capacity of Aluminium is $c_{Alu} = 0.897$ kJ kg^{-1} K^{-1} such that the thermal capacity of the three shields is given by $C_3 \approx 12.4$ kJ K^{-1}, $C_2 \approx 9.11$ kJ K^{-1} and $C_1 \approx 6.27$ kJ K^{-1} respectively. The cavity itself has a mass of approximately $M_c \approx 3.3$ kg and the specific heat capacity of ULE is $c_{ULE} = 0.767$ kJ kg^{-1} K^{-1}. Hence, the cavity will have a thermal heat capacity of $C \approx 2.53$ kJ K^{-1}. A summary of the relevant properties of all the materials used are given in table 6.

To combat the conductive heat transfer between the heat shields and the cavity base plate, they are separated by Teflon spheres. Teflon acts as an insulator with a relatively poor thermal conductivity of $\lambda = 0.25$ W m^{-1} K^{-1}. The spheres are positioned in a balanced three-point

Table 6: Relevant properties of the materials used for the construction of the heat shield design.

Material	**Density** ρ $\mathrm{g\ cm^{-3}}$	**Thermal conductivity** λ $\mathrm{W\ m^{-1}\ K^{-1}}$	**Emissivity** ϵ	**Heat capacity** c $\mathrm{J\ g^{-1}\ K^{-1}}$
Aluminium	2.71	235	0.03	0.897
ULE	2.21	1.31	0.92	0.767
Viton	1.85	0.235	-	1.65
Teflon	2.29	0.25	-	1.01

configuration such that the center-of-gravity of the cavity mounted on the base plate, overlaps with the center-of-mass of the triangle the spheres form. An overview of the mounted cavity inside the three heat shields is shown in figure 39.

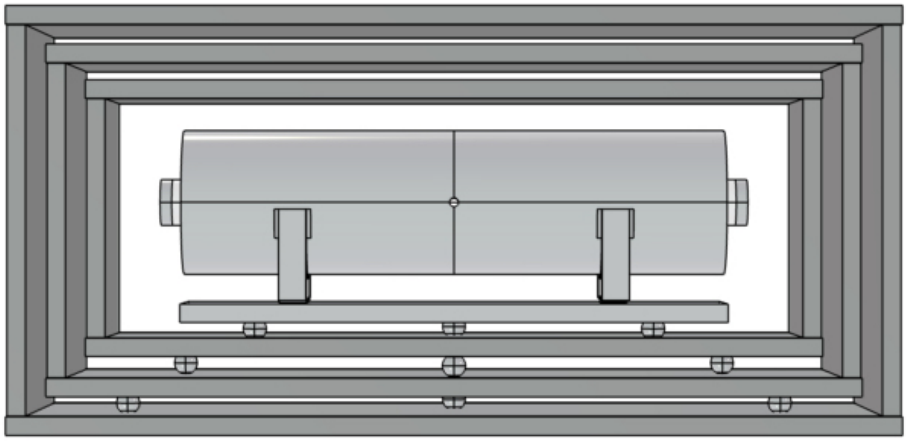


Figure 39: 3D rendering of the ULE cavity and mounting system placed inside three heat shields; an active temperature stabilized outer shield and two passive inner heat shields. The cavity base plate and heat shields are separated by spheres placed in a balanced three-point mount configuration.

To estimate the temperature response of the cavity to a change in temperature of the outermost active heat shield, we do a FEM simulation in COMSOL. We simplify the simulation by only considering the dominant radiative heat transfer mechanism, which is a good approximation since the amount of contact area between the insulating spheres is minimal. Furthermore, in the simulation, we disregard the influence of windows or vent holes in the heat shields. We apply a temperature of $T = 303.15$ K to the outer boundary surface of the active heat shield while the inner heat shields and cavity start at a temperature of 293.15 K imposing a temperature step of $\Delta T = 10$ K. The evolution in time of the temperature of the heat shields and cavity

is depicted in figure 40, where we normalized the temperature step with $[T(t) - T(0)]/\Delta T$. A fit to the curve of the cavity temperature is made following equation 87. The resulting time constants are found to be $t_a = 1.32$ d, $t_b = 0.85$ d and $t_c = 6.43$ d. We can see that only considering radiative heat transfer it takes up to 15 days for the temperature of the cavity to equilibrate to the applied temperature step at the active heat shield.

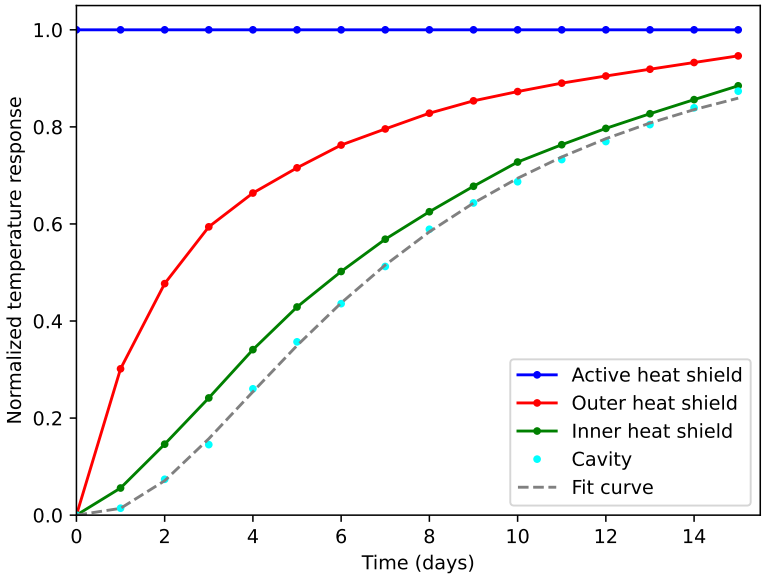


Figure 40: FEM simulation of the normalized temperature response of the heat shields and cavity due to radiative heat transfer only. The cavity temperature is fitted with equation 87, the best fit time constants are $t_a = 1.32$ d, $t_b = 0.85$ d and $t_c = 6.43$ d.

4 Optical layout for the stabilization of the clock laser

In figure 41 the provisional optical layout of the optical reference cavity is depicted. The different feedback mechanisms are color coded for clarity. The laser light passes an optical isolator and an AOM that stabilizes the frequency to the cavity resonance using the PDH technique, depicted in blue. Afterwards a portion of the total optical power is sent towards the cavity by a polarizing beam splitter (PBS) cube and is fiber coupled. The fiber contains an additional AOM that corrects for accumulated (fiber) phase noise, depicted in yellow, and also stabilizes the light intensity, depicted in purple. The fiber runs from the laser board to the active vibration isolation platform where the ultrastable cavity is placed. The light coming out of the other end of the optical fiber is phase modulated by an EOM, creating the sidebands required for the PDH lock. The RAM that the EOM causes is detected by splitting of part of the light using a PBS and measuring the light intensity with a photodiode (PD). From the PD output, a feedback signal is continuously given to the EOM to actively suppress the RAM as described in section 2.5.2. Next, the light passes through a coupling lens (CL) that ensures a good coupling into the cavity. From there the light goes trough an optical isolator that is used to split off the back reflection from the cavity to create the PDH error signal, depicted in blue, as highlighted in section 2.5.1. The light that is transmitted through the cavity is split into two paths by a beam splitter. One path goes to a CCD camera and the other path goes towards two separate PD's. The light transmitted by the second beam splitter is detected by a photodiode that measures the optical power and provides a signal for the power stabilization to feedback to the fiber coupled AOM. The residual reflected light passes a PBS where it is overlapped with light from the second branch that is effectively free from fiber noise by active cancellation, as introduced in section 2.5.3. The phase noise of the cavity branch is suppressed by locking the phase of the cavity branch to the fiber noise cancelled branch with a phase-locked-loop (PLL).

The resulting frequency stabilized light is sent through an optical fiber with FNC to the frequency comb for distribution and comparison and to the atoms in the 1D optical lattice to create a clock signal.

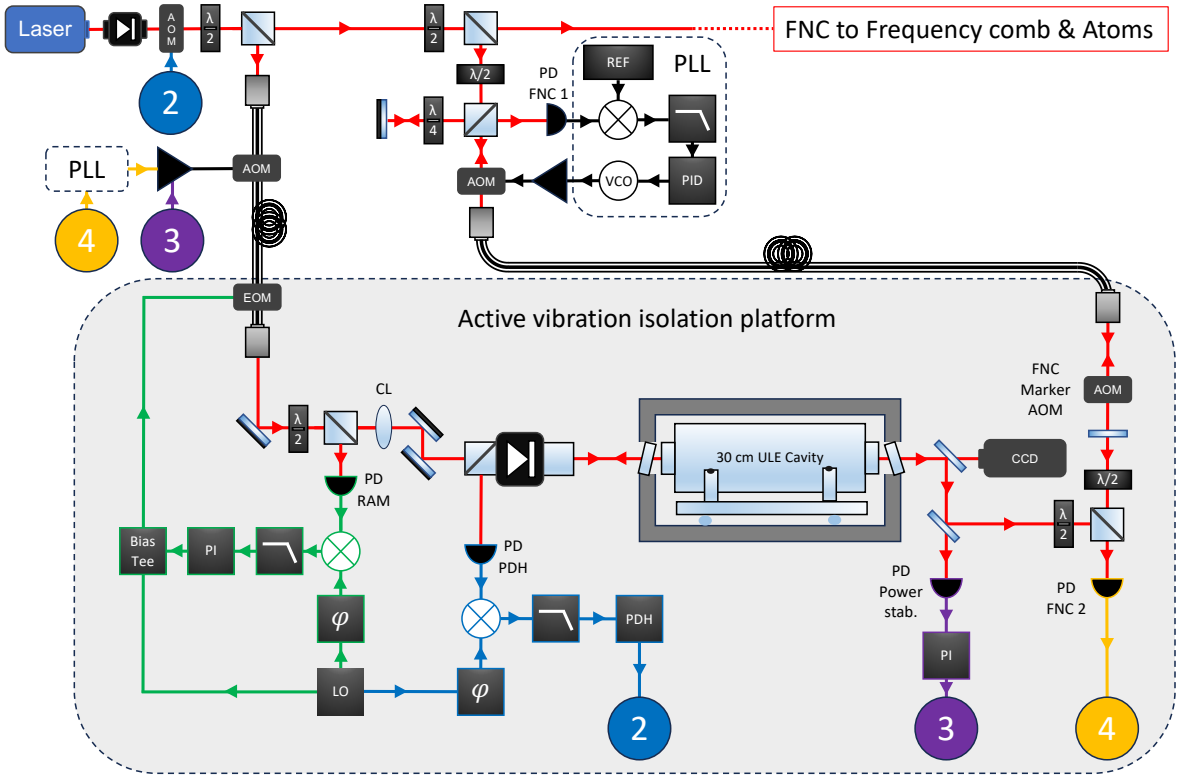


Figure 41: Preliminary schematic of the optical setup of the 30 cm ULE cavity. The setup consists of a cavity branch, split off by the first PBS after the laser, and a fiber noise cancelled branch, split of by the second PBS on the top. Depicted in blue: PDH stabilization, green: active RAM suppression, purple: power stabilization, yellow: cavity branch fiber noise cancellation.

5 Summary & Outlook

The goal of this project is to design and build a new ultrastable optical cavity to provide a short term frequency reference for a strontium clock laser at 698 nm. The aim for this cavity is to be able to provide thermal-noise-limited frequency instability of $\sigma_y < 3 \cdot 10^{-16}$ at 1 second of averaging time. In the future, this oscillator could be used as a new frequency standard for the Netherlands, distributed over fiber-links. A frequency comb will be used to transfer the stability of the clock light at 698 nm to the telecommunication C-band range around 1550 nm.

In this work, we have provided the theoretical background necessary to understand the working principles of an optical cavity and how to stabilize a laser to a cavity using the PDH technique. Further, we have seen different noise sources that require active suppression and how to implement active compensation schemes. We have seen how to transfer the stability of one laser to another which are separated far in frequency using a frequency comb and how to compare the instabilities of multiple oscillators.

Next, we went through the design process of the ultrastable cavity. We have shown the current limitations of modern cavities, hindering the further reduction of the thermal noise floor, namely, Brownian noise and looked into the influence of different materials and mirror configurations on the noise floor. Here we arrived at a cylindrical cavity geometry with a length of 30 cm, to be able to reach the projected frequency instability.

To ensure that the cavity reaches its projected thermal-noise-floor it needs to be made insensitive to external perturbations, in particular, vibrations. To achieve this, the mechanical instability was investigated using finite-element method analysis in COMSOL. A theoretical model for the response of the cavity length to accelerations was made based on the Poisson effect and mirror tilt. The cavity geometry was varied and an optimal spacer diameter of 8 cm was found. Furthermore, the optimal supporting points were determined at $dx = 61.35$ mm and $dz = 3.75$ mm. This resulted in the following acceleration and tilt sensitivities gradients $\frac{\delta k_z}{\delta dz} = 7.3 \cdot 10^{-11}$ g^{-1} mm^{-1}, $\frac{\delta \kappa_z}{\delta dx} = 7.0 \cdot 10^{-11}$, $\frac{\delta \kappa_y}{\delta dx} = 7.3 \cdot 10^{-11}$ and $\frac{\delta \kappa_x}{\delta dz} = -8.1 \cdot 10^{-11}$ g^{-1} mm^{-2}. In addition, a self balancing mounting structure design for the cavity was made.

The thermal sensitivity of the cavity was investigated by creating a model that formulates an effective coefficient of thermal expansion. The relative cavity length change $\frac{\Delta L}{L}$ was simulated using COMSOL at differing temperatures. The ability of ULE annuli attached to the backside of the fused silica mirror substrates, to compensate the zero-crossing temperature shift was investigated.

Furthermore, the effectiveness of a three-layer aluminium heat shield design was simulated. First, a theoretical model that describes the radiative and conductive heat transfer was formulated and a time dependent temperature expression for the three heat shields and cav-

ity was found. A geometrical model of the heat shields surrounding the cavity was made in COMSOL and the time dependent radiative heat transfer response was found by applying a temperature step to the outermost boundary of the active heat shield. Lastly, we propose the preliminary design of the complete optical setup surrounding the cavity, including the PDH laser stabilization, fiber noise cancellation, active RAM suppression and power stabilization.

Currently, the ULE material has been ordered from Corning, after which it will be send to Optrovision, who will machine the spacer and mounting structure from the block of ULE. Next, the cavity mirrors need to be optically contacted to the polished spacer ends. Possibly, to expedite this process, the optical contacting can be done by an external company. Concurrent to this the heat shields with active heating elements and vacuum chamber designs need to be finalized and machined.

In the future, when the optical cavity is operational, it needs to characterized and its sensitivity to external perturbations needs to be investigated. This is typically accomplished by exacerbating the perturbation and measuring the resulting frequency instability compared to a second reference oscillator.

Acknowledgements

First and foremost, I would like to thank everyone in the entire strontium group, all of you create a fantastic atmosphere in the lab and I am incredibly grateful to be part of and work together with this group of people. The fact that everyone was so willing to offer their support and experience, for over a year, is truly amazing and I can confidently say that this thesis wouldn't have been possible without the help of my great team members.

- I am especially grateful to Florian for providing me with this opportunity and supporting me throughout the project. The enthusiasm and motivation you bring while speaking about physics is unmatched to me.
- I am forever thankful to Sumit for the amazing support and guidance that he has offered me. Your continuous encouragement, mentorship and patience have allowed me to keep going, I couldn't have done this without you.
- My other direct lab colleagues, Ananya, Andras and Stefano make it a pleasure to come to the lab each day. I enjoy working with you very much and I hope to continue doing so.
- The person that is always able to turn my frown upside down has to be Sheng. The joy that you bring besides your incredible technical knowledge and experience, is wonderful.
- I want to thank Simon, Noé, Digvijay, Noah and Yu-Chih for sharing a fantastic and memorable week in Hannover with me. The fun times we had, be it in the gym or in the lab, I will never forget.
- Additionally, I would like to thank Francesca, Camila, Stefan, Benedikt, Prem, Ivo, Alex, Shayne and Junyu for their support and help during my project.
- I would like to thank Klaas-Jan for being the second examiner of my project and for the good spirit you bring to the group.
- I would also like to express my gratefulness to Mateusz Narożnik for the feedback you provided and the exchanges we had about my design.
- Furthermore, I would like to thank the members of Rene's group for their support and kindness.
- Special thanks to Nella, Bas and Evelien for their support throughout my master's project. Thanks for all the lovely coffee breaks and mental support.
- Finally, I would like to express my endless love and gratefulness to my parents who never stop to support me.

A Power spectral density & Allan deviation

The power spectral density (PSD) can be calculated using the autocorrelation function $R_y(\tau)$ of the frequency fluctuations, it is defined as

$$R_y(\tau) \equiv \overline{\Delta\nu(t+\tau)\cdot\Delta\nu(t)} = \lim_{T\to+\infty}\frac{1}{2T}\int_{-\infty}^{\infty}\Delta\nu(t+\tau)\cdot\Delta\nu(t)\,dt \tag{88}$$

The Wiener-Khinchin theorem states that the two-sided PSD $S_y^{2-sided}(f)$ can be calculated by taking the Fourier transform of the autocorrelation function $R_y(\tau)$ [63]. This Fourier transform pair is given by

$$S_y^{\text{2-sided}}(f) = \int_{-\infty}^{\infty} R_y(\tau)e^{-i2\pi f\tau}\,d\tau, \tag{89}$$

$$R_y(\tau) = \int_{-\infty}^{\infty} S_y^{\text{2-sided}}(f)e^{i2\pi f\tau}\,df. \tag{90}$$

In an experiment only the positive frequencies are of interest, so the two-sided PSD is related to the one-sided PSD simply as

$$S_y(f) \equiv 2\cdot S_y^{\text{2-sided}}(f). \tag{91}$$

To characterize the stability of an oscillator one can measure the fractional frequency fluctuations $y(t)$ by taking N samples that each have been averaged over a time interval τ, with a time T between each measurement [50]. The N-sample variance is given by

$$\sigma_y^2(N,T,\tau) \equiv \frac{1}{N-1}\left(\sum_{i=0}^{N-1}\left[\frac{y(iT+\tau)-y(iT)}{\tau}\right] - \frac{1}{N}\left[\sum_{i=0}^{N-1}\frac{y(iT+\tau)-y(iT)}{\tau}\right]^2\right), \tag{92}$$

$$= \frac{1}{N-1}\left(\sum_{i=1}^{N}\overline{y}_i^2 - \frac{1}{N}\left[\sum_{j=1}^{N}\overline{y}_j\right]^2\right). \tag{93}$$

The Allan deviation is simply the two-sample $N=2$ variance with zero dead time $T=\tau$, given by

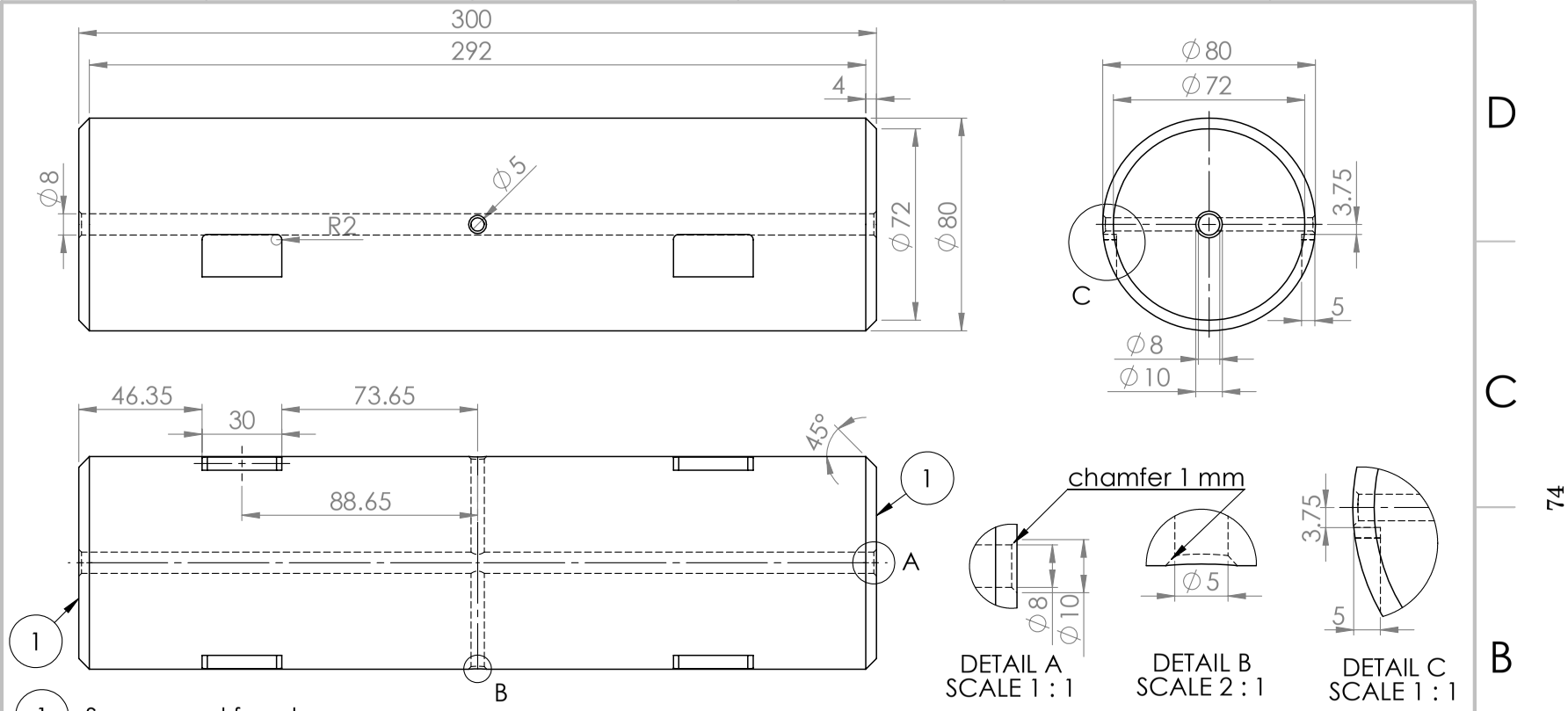
$$\sigma_y^2(\tau) \equiv \left\langle\sigma_y^2(2,\tau,\tau)\right\rangle = \frac{1}{2(N-1)}\sum_{i=1}^{N-1}(\overline{y}_{i+1}-\overline{y}_i)^2, \tag{94}$$

where $\langle ...\rangle$ denotes the expectation operator. By looking at the behaviour of the Allan deviation $\sigma_y(\tau)$ as a function of τ it is possible to identify dominant noise processes. However, the Allan deviation is unable to separate flicker phase noise and white phase noise since they present the same τ scaling at high Fourier frequencies. To be able to distinguish these two, the modified Allan variance Mod $\sigma_y^2(\tau)$ is used, given by

$$\text{Mod }\sigma_y^2(\tau) = 2\int_0^{\infty} S_y(f)\frac{\sin^6(\pi f\tau)}{(\pi f\tau)^4}df, \tag{95}$$

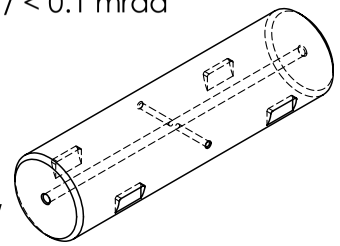
which was introduced by Allan and Barnes [64].

B Technical drawings cavity & mounting structure



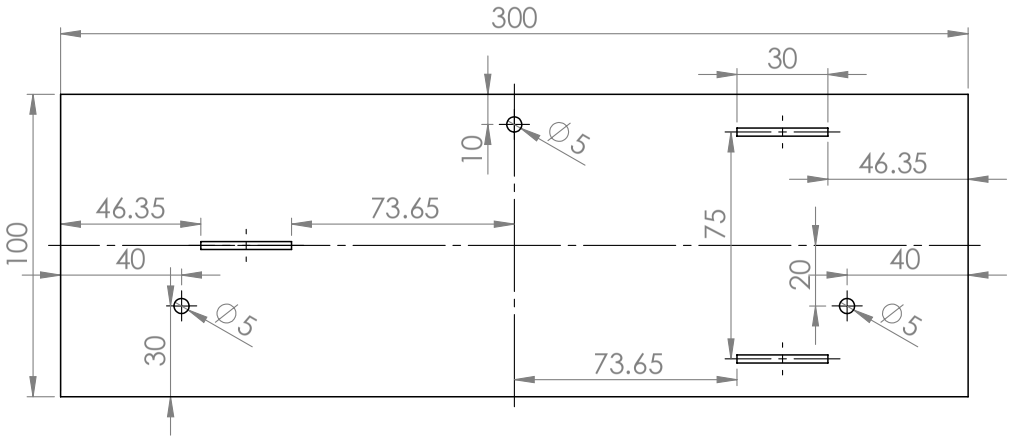
(1) Spacer end facets:

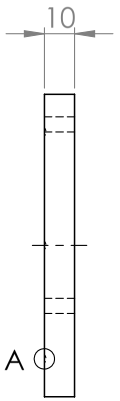
- Surface flatness polished to < λ / 10
- Parallelism // < 0.1 mrad

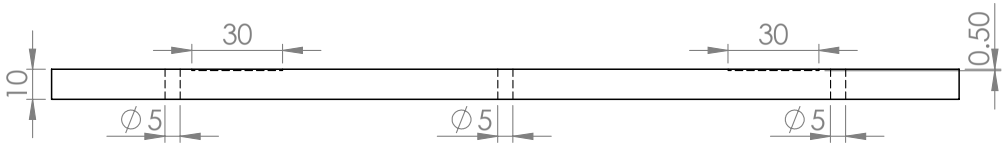


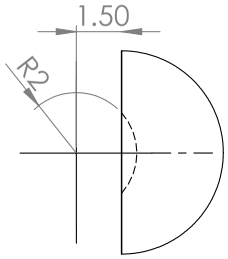
ISOMETRIC VIEW
SCALE 1 : 5

UNLESS OTHERWISE SPECIFIED: DIMENSIONS ARE IN MILLIMETERS SURFACE FINISH: TOLERANCES: LINEAR: 0.1 ANGULAR:			FINISH:			DEBURR AND BREAK SHARP EDGES	DO NOT SCALE DRAWING / REVISION
	NAME	SIGNATURE	DATE				TITLE: ULE Cavity Spacer
DRAWN	UvA						
CHK'D							
APPV'D							
MFG							
Q.A				MATERIAL: Corning ULE 7972 Premium Grade			DWG NO. / A4
				WEIGHT:			SCALE:1:2 / SHEET 1 OF 1

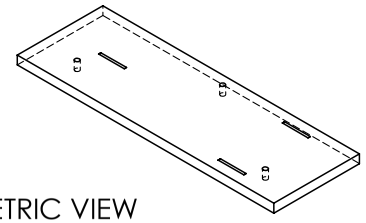








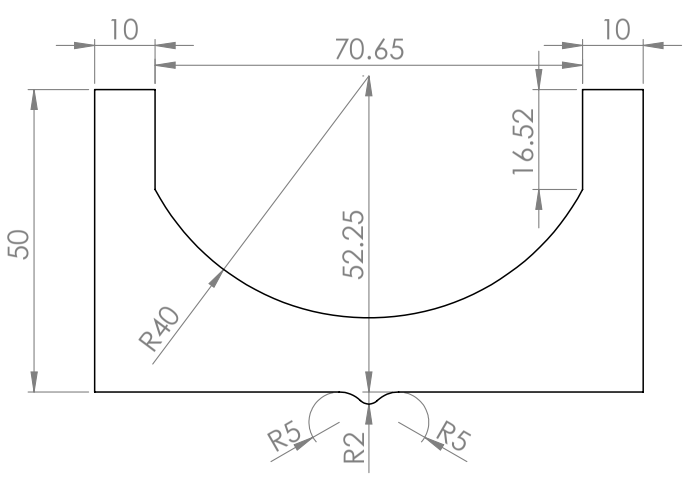
DETAIL A
SCALE 5 : 1

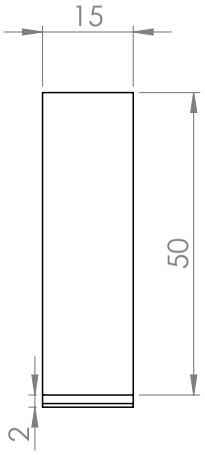


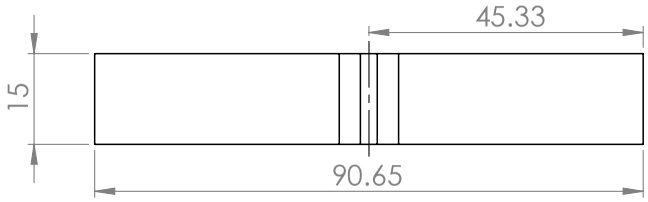
ISOMETRIC VIEW
SCALE 1 : 5

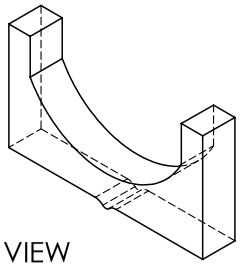
UNLESS OTHERWISE SPECIFIED: DIMENSIONS ARE IN MILLIMETERS SURFACE FINISH: TOLERANCES: 0.1 LINEAR: ANGULAR:		FINISH:		DEBURR AND BREAK SHARP EDGES		DO NOT SCALE DRAWING	REVISION
	NAME	SIGNATURE	DATE			TITLE:	
DRAWN	UvA					ULE Base Plate	
CHK'D							
APPV'D							
MFG							
Q.A				MATERIAL: Corning ULE 7972 Premium Grade		DWG NO.	A4
				WEIGHT:		SCALE:1:2	SHEET 1 OF 1

75



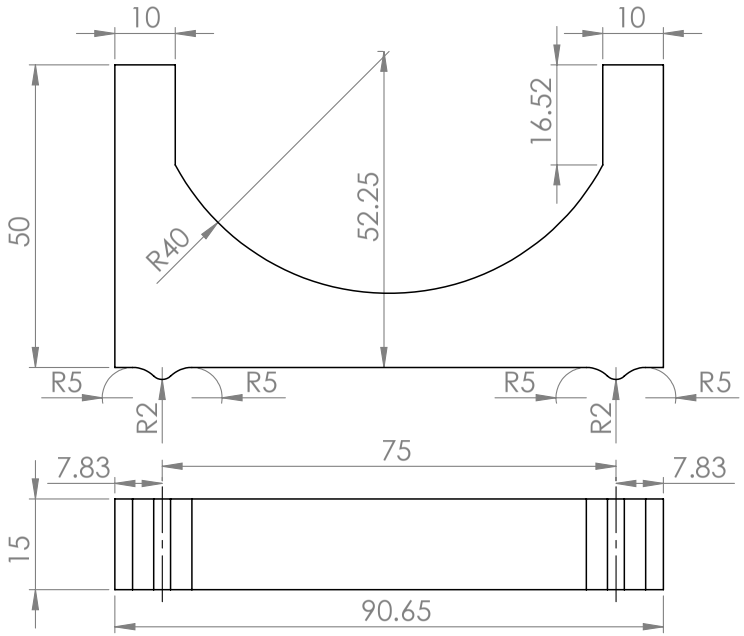


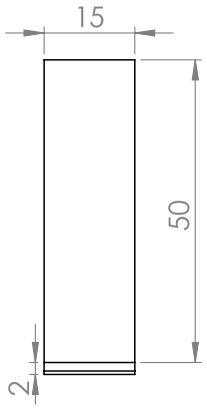


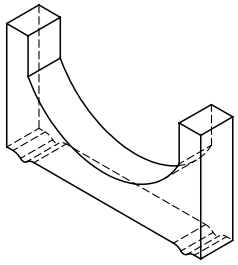


ISOMETRIC VIEW
SCALE 1 : 2

UNLESS OTHERWISE SPECIFIED: DIMENSIONS ARE IN MILLIMETERS SURFACE FINISH: TOLERANCES: 0.1 LINEAR: ANGULAR:		FINISH:		DEBURR AND BREAK SHARP EDGES		DO NOT SCALE DRAWING	REVISION
	NAME	SIGNATURE	DATE			TITLE: ULE U-Shaped Mount 1	
DRAWN	UvA						
CHK'D							
APPV'D							
MFG							
Q.A				MATERIAL: Corning ULE 7972 Premium Grade		DWG NO.	A4
				WEIGHT:		SCALE:1:1	SHEET 1 OF 1







ISOMETRIC VIEW
SCALE 1 : 2

UNLESS OTHERWISE SPECIFIED: DIMENSIONS ARE IN MILLIMETERS SURFACE FINISH: TOLERANCES: LINEAR: 0.1 ANGULAR:		FINISH:		DEBURR AND BREAK SHARP EDGES		DO NOT SCALE DRAWING	REVISION
	NAME	SIGNATURE	DATE			TITLE: ULE U-Shaped Mount 2	
DRAWN	UvA						
CHK'D							
APPV'D							
MFG							
Q.A				MATERIAL: Corning ULE 7972 Premium Grade		DWG NO.	A4
				WEIGHT:		SCALE:1:1	SHEET 1 OF 1

References

[1] D. D. McCarthy, Evolution of timescales from astronomy to physical metrology, *Metrologia* **48**, S132 (2011).

[2] Lord kelvin on atoms as fundamental natural standards (for base units), *IEEE Transactions on Instrumentation and Measurement* **22**, 99 (1973).

[3] T. W. Hänsch A. L. Schawlow, Cooling of gases by laser radiation, *Optics Communications* **13**, 68 (1975).

[4] D. J. Wineland, R. E. Drullinger F. L. Walls, Radiation-pressure cooling of bound resonant absorbers, *Physical Review Letters* **40**, 1639 (1978).

[5] W. D. Phillips, J. V. Prodan H. J. Metcalf, Laser cooling and electromagnetic trapping of neutral atoms, *JOSA B* **2**, 1751 (1985).

[6] S. Chu, L. Hollberg, J. E. Bjorkholm, A. Cable A. Ashkin, Three-dimensional viscous confinement and cooling of atoms by resonance radiation pressure, *Physical review letters* **55**, 48 (1985).

[7] P. Gill, When should we change the definition of the second?, *Philosophical Transactions of the Royal Society A: Mathematical, Physical and Engineering Sciences* **369**, 4109 (2011).

[8] T. E. Mehlstäubler, G. Grosche, C. Lisdat, P. O. Schmidt H. Denker, Atomic clocks for geodesy, *Reports on Progress in Physics* **81**, 064401 (2018).

[9] C.-W. Chou, D. B. Hume, T. Rosenband D. J. Wineland, Optical clocks and relativity, *Science* **329**, 1630 (2010).

[10] V. Dzuba V. Flambaum, Atomic optical clocks and search for variation of the fine-structure constant, *Physical Review A* **61**, 034502 (2000).

[11] N. Huntemann *et al.*, Improved limit on a temporal variation of m p/m e from comparisons of yb+ and cs atomic clocks, *Physical review letters* **113**, 210802 (2014).

[12] K. Numata, A. Kemery J. Camp, Thermal-noise limit in the frequency stabilization of lasers with rigid cavities, *Phys. Rev. Lett.* **93**, 250602 (2004).

[13] M. D. Álvarez, *Optical cavities for optical atomic clocks, atom interferometry and gravitational-wave detection* (Springer, 2019).

[14] S. Häfner, Ultra-stabile lasersysteme für weltraum-und bodenanwendungen, Ph.D. thesis, Hannover: Gottfried Wilhelm Leibniz Universität Hannover (2015).

[15] G. D. Cole, W. Zhang, M. J. Martin, J. Ye M. Aspelmeyer, Tenfold reduction of brownian noise in high-reflectivity optical coatings, *Nature Photonics* **7**, 644 (2013).

[16] D. G. Matei *et al.*, 1.5 μm lasers with sub-10 mhz linewidth, *Phys. Rev. Lett.* **118**, 263202 (2017).

[17] C. Hagemann, Ultra-stable laser based on a cryogenic single-crystal silicon cavity, Ph.D. thesis, Hannover: Gottfried Wilhelm Leibniz Universität Hannover (2013).

[18] S. T. Dawkins, J. J. McFerran A. N. Luiten, Considerations on the measurement of the stability of oscillators with frequency counters, *IEEE Transactions on Ultrasonics, Ferroelectrics, and Frequency Control* **54**, 918 (2007).

[19] W. M. Itano *et al.*, Quantum projection noise: Population fluctuations in two-level systems, *Physical Review A* **47**, 3554 (1993).

[20] E. Hecht, *Optics* (Pearson Education, 2017), fifth edn.

[21] H. Kogelnik T. Li, Laser beams and resonators, *Applied optics* **5**, 1550 (1966).

[22] S. Feng H. G. Winful, Physical origin of the gouy phase shift, *Optics letters* **26**, 485 (2001).

[23] R. W. Drever *et al.*, Laser phase and frequency stabilization using an optical resonator, *Applied Physics B* **31**, 97 (1983).

[24] R. W. Fox, C. W. Oates L. W. Hollberg, *Experimental methods in the physical sciences* (Elsevier, 2003), vol. 40, pp. 1–46.

[25] T. Hansch B. Couillaud, Laser frequency stabilization by polarization spectroscopy of a reflecting reference cavity, *Optics communications* **35**, 441 (1980).

[26] E. D. Black, An introduction to pound–drever–hall laser frequency stabilization, *American journal of physics* **69**, 79 (2001).

[27] H. Shen, L. Li, J. Bi, J. Wang L. Chen, Systematic and quantitative analysis of residual amplitude modulation in pound-drever-hall frequency stabilization, *Phys. Rev. A* **92**, 063809 (2015).

[28] E. A. Whittaker, M. Gehrtz G. C. Bjorklund, Residual amplitude modulation in laser electro-optic phase modulation, *JOSA B* **2**, 1320 (1985).

[29] N. Wong J. L. Hall, Servo control of amplitude modulation in frequency-modulation spectroscopy: demonstration of shot-noise-limited detection, *JOSA B* **2**, 1527 (1985).

[30] Z. Tai *et al.*, Electro-optic modulator with ultra-low residual amplitude modulation for frequency modulation and laser stabilization, *Optics letters* **41**, 5584 (2016).

[31] W. Zhang *et al.*, Reduction of residual amplitude modulation to 1× 10-6 for frequency modulation and laser stabilization, *Optics letters* **39**, 1980 (2014).

[32] L. Li, F. Liu, C. Wang L. Chen, Measurement and control of residual amplitude modulation in optical phase modulation, *Review of Scientific Instruments* **83**, 043111 (2012).

[33] M. Schioppo *et al.*, Comparing ultrastable lasers at 7× 10- 17 fractional frequency instability through a 2220 km optical fibre network, *Nature communications* **13**, 212 (2022).

[34] G. Grosche *et al.*, Optical frequency transfer via 146 km fiber link with 10- 19 relative accuracy, *Optics letters* **34**, 2270 (2009).

[35] L.-S. Ma, P. Jungner, J. Ye J. L. Hall, Delivering the same optical frequency at two places: accurate cancellation of phase noise introduced by an optical fiber or other time-varying path, *Optics letters* **19**, 1777 (1994).

[36] L. Cohen J. Fleming, Effect of temperature on transmission in lightguides, *The Bell System Technical Journal* **58**, 945 (1979).

[37] J. Ye *et al.*, Delivery of high-stability optical and microwave frequency standards over an optical fiber network, *JOSA B* **20**, 1459 (2003).

[38] H. R. Telle, B. Lipphardt J. Stenger, Kerr-lens, mode-locked lasers as transfer oscillators for optical frequency measurements, *Applied Physics B* **74**, 1 (2002).

[39] J. Stenger, H. Schnatz, C. Tamm H. R. Telle, Ultraprecise measurement of optical frequency ratios, *Phys. Rev. Lett.* **88**, 073601 (2002).

[40] H. R. Telle *et al.*, Carrier-envelope offset phase control: A novel concept for absolute optical frequency measurement and ultrashort pulse generation, *Applied Physics B* **69**, 327 (1999).

[41] J. E. Gray D. W. Allan, *28th annual symposium on frequency control* (IEEE, 1974), pp. 243–246.

[42] P. Tavella A. Premoli, Estimating the instabilities of n clocks by measuring differences of their readings, *Metrologia* **30**, 479 (1994).

[43] Y. Levin, Internal thermal noise in the ligo test masses: A direct approach, *Phys. Rev. D* **57**, 659 (1998).

[44] Y. T. Liu K. S. Thorne, Thermoelastic noise and homogeneous thermal noise in finite sized gravitational-wave test masses, *Phys. Rev. D* **62**, 122002 (2000).

[45] H. B. Callen T. A. Welton, Irreversibility and generalized noise, *Phys. Rev.* **83**, 34 (1951).

[46] T. Kessler, T. Legero U. Sterr, Thermal noise in optical cavities revisited, *J. Opt. Soc. Am. B* **29**, 178 (2012).

[47] F. Bondu, P. Hello J.-Y. Vinet, Thermal noise in mirrors of interferometric gravitational wave antennas, *Physics Letters A* **246**, 227 (1998).

[48] N. Nakagawa, A. M. Gretarsson, E. K. Gustafson M. M. Fejer, Thermal noise in half-infinite mirrors with nonuniform loss: A slab of excess loss in a half-infinite mirror, *Phys. Rev. D* **65**, 102001 (2002).

[49] G. M. Harry *et al.*, Thermal noise in interferometric gravitational wave detectors due to dielectric optical coatings, *Classical and Quantum Gravity* **19**, 897 (2002).

[50] D. Allan, Statistics of atomic frequency standards, *Proceedings of the IEEE* **54**, 221 (1966).

[51] T. Kessler *et al.*, A sub-40-mhz-linewidth laser based on a silicon single-crystal optical cavity, *Nature Photonics* **6**, 687 (2012).

[52] ULE® corning code 7972 ultra low expansion glass, Available at `https://www.corning.com/worldwide/en/products/advanced-optics/product-materials/semiconductor-laser-optic-components/ultra-low-expansion-glass.html` (2016).

[53] T. Legero, T. Kessler U. Sterr, Tuning the thermal expansion properties of optical reference cavities with fused silica mirrors, *J. Opt. Soc. Am. B* **27**, 914 (2010).

[54] S. A. Webster, M. Oxborrow P. Gill, Vibration insensitive optical cavity, *Phys. Rev. A* **75**, 011801 (2007).

[55] D. R. Leibrandt *et al.*, Spherical reference cavities for frequency stabilization of lasers in non-laboratory environments, *Opt. Express* **19**, 3471 (2011).

[56] S. Amairi ep Pyka, A long optical cavity for sub-hertz laser spectroscopy, Ph.D. thesis, Hannover: Gottfried Wilhelm Leibniz Universität Hannover (2014).

[57] J. Keller, Spectroscopic characterization of ion motion for an optical clock based on coulomb crystals, Ph.D. thesis, Hannover: Gottfried Wilhelm Leibniz Universität Hannover (2015).

[58] T. Nazarova, F. Riehle U. Sterr, Vibration-insensitive reference cavity for an ultra-narrow-linewidth laser, *Applied Physics B* **83**, 531 (2006).

[59] D. Newell *et al.*, An ultra-low-noise, low-frequency, six degrees of freedom active vibration isolator, *Review of scientific instruments* **68**, 3211 (1997).

[60] R. Hauck, H. Kortz H. Weber, Misalignment sensitivity of optical resonators, *Applied Optics* **19**, 598 (1980).

[61] A. E. Siegman, *Lasers* (University science books, 1986).

[62] S. Häfner *et al.*, 8× 10- 17 fractional laser frequency instability with a long room-temperature cavity, *Optics letters* **40**, 2112 (2015).

[63] L. Cohen, *Proceedings of the 1998 IEEE International Conference on Acoustics, Speech and Signal Processing, ICASSP'98 (Cat. No. 98CH36181)* (IEEE, 1998), vol. 3, pp. 1577–1580.

[64] D. W. Allan J. A. Barnes, *Proceedings of the 35th Annual Frequency Control Symposium* (1981), vol. 5, pp. 470–475.